Universidade de Aveiro
2019

Departamento de Física

Alexandre Manuel Pedroso Botas

Fotoluminescência de Sistemas de Nanopartículas Cristalinas de Silício

Photoluminescence of Crystalline Silicon Nanoparticle Systems

Universidade de Aveiro
2019

Departamento de Física

Alexandre Manuel Pedroso Botas

Fotoluminescência de Sistemas de Nanopartículas Cristalinas de Silício

Photoluminescence of Crystalline Silicon Nanoparticle Systems

Tese apresentada à Universidade de Aveiro para cumprimento dos requisitos necessários à obtenção do grau de Doutor em Física, realizada sob a orientação científica do Doutor Rui Nuno Marques Pereira, Equiparado a Investigador Principal do Departamento de Física da Universidade de Aveiro e da Doutora Maria Rute de Amorim e Sá Ferreira André, Professora Associada com Agregação do Departamento de Física da Universidade de Aveiro.

Este trabalho foi desenvolvido no âmbito dos projetos I3N, UID/CTM/50025/2013, e CICECO−Instituto de Materiais de Aveiro, UID/CTM/50011/2013, financiados por fundos nacionais através do FCT/MEC e cofinanciado pelo FEDER sob o acordo PT2020. O autor agradece o apoio financeiro dado pela FCT através da bolsa de doutoramento SFRH/BD/104789/2014.

o júri

presidente

Prof. Doutor Fernando Joaquim Fernandes Tavares Rocha
professor catedrático da Universidade de Aveiro

Prof. Doutor José António de Carvalho Paixão
professor catedrático da Universidade de Coimbra - Faculdade de Ciências e Tecnologias

Prof. Doutor Luís António Ferreira Martins Dias Carlos
professor catedrático da Universidade de Aveiro

Doutora Maria de Fátima Guimarães Cerqueira
professora auxiliar da Universidade do Minho

Doutor João Oliveira Ventura
investigador principal da Universidade do Porto

Doutor Rui Nuno Marques Pereira
equiparado a investigador principal da Universidade de Aveiro

agradecimentos

O trabalho realizado só foi possível graças à colaboração de algumas pessoas e instituições a quem agradeço.

Aos meus orientadores o Doutor Rui Nuno Marques Pereira e a Professora Doutora Maria Rute de Amorim e Sá Ferreira André pela oportunidade de realizar este trabalho e pelo apoio dado.

Aos membros dos grupos do Professor Doutor Uwe Kortshagem e do Professor Doutor Hartmut Wiggers responsáveis pela síntese e funcionalização das nanopartículas.

Aos membros do grupo do Professor Doutor Martin Stutzmann por me receberem no Walter Schottky Institut da Technical University of Munich, onde parte do trabalho apresentado no capítulo 5 foi realizado. Ao Mestre Markus Wiesinger e ao Mestre Felix Eckmann pela ajuda no trabalho realizado.

Ao Professor Doutor Luís Carlos e ao Doutor Carlos Brites pelas discussões relativas às medidas de termometria.

Ao Doutor Nuno João Silva pela ajuda dada na utilização do método Rietveld.

Ao Professor Doutor Joaquim Leitão pela ajuda com as medidas de fotoluminescência apresentadas no capítulo 5 e ao Mestre Bruno Falcão pela ajuda com as medidas de espectroscopia de Raman.

Aos colegas do grupo Phantom-G, em especial à Doutora Vânia Freitas, pela ajuda e bom ambiente de trabalho.

Ao Departamento de Física e aos Laboratórios Associados CICECO−Instituto de Materiais de Aveiro e I3N pelas condições de trabalho proporcionadas.

À Fundação para a Ciência e Tecnologia pelo apoio financeiro.

À minha família e a todos os que fizeram parte deste percurso.

palavras-chave

Nanopartículas cristalinas de silício, terminação de hidrogénio, superfície oxidada, funcionalização orgânica, espectroscopia de fotoluminescência, termómetro luminescente primário, filmes infiltrados com Al_2O_3.

resumo

O entendimento das propriedades de luminescência do silício à escala nanométrica é uma questão relevante para o desenvolvimento de novos dispositivos emissores de luz.

Neste âmbito, esta tese foca o estudo das propriedades de emissão de nanopartículas cristalinas de silício, com diferentes terminações da superfície (hidrogénio, óxido de silício ou moléculas orgânicas), utilizando espectroscopia de fotoluminescência em modo estacionário e resolvido no tempo e medidas de rendimento quântico de emissão. À temperatura ambiente, os espectros de emissão das nanopartículas terminadas com hidrogénio e funcionalizadas com moléculas orgânicas, com tamanhos médios de ≈3.4 e ≈2.4 nm, apresentam uma componente centrada, respetivamente em ≈800 e ≈750 nm. Esta componente é atribuída à recombinação de excitões fotogerados no núcleo de silício da nanopartícula. Uma componente adicional, a maiores energias, está presente no espectro de nanopartículas com óxido de silício à superfície, sendo atribuída à recombinação de pares dados-aceitador de estados associados ao óxido. Os valores medidos para os tempos de vida de emissão e para o rendimento quântico de emissão dependem da terminação da superfície e são discutidos, através da transferência de excitões intra- e inter-nanopartículas. O valor mais alto de rendimento quântico de emissão à temperatura ambiente para amostras em filme foi medido para nanopartículas com funcionalização orgânica (0.23±0.02). Uma outra vertente do trabalho, envolveu filmes de nanopartículas de silício infiltrados com Al_2O_3, utilizando deposição em camadas atómica. A camada depositada permite proteger os filmes contra a oxidação e observa-se uma alteração do espectro de emissão das nanopartículas, relativamente a nanopartículas análogas sem infiltração. Este trabalho abre novas questões sobre o papel da terminação e separação entre nanopartículas no que respeita às propriedades de emissão.

Tirando partido da dependência da emissão com a temperatura foi desenvolvido um termómetro primário inovador. Em particular, é mostrado que termómetros luminescentes baseados em nanopartículas de silício processadas em filme e em solução podem operar em diversos ambientes com um parâmetro termométrico (energia do pico de emissão) descrito por uma equação de estado bem estabelecida. O termómetro apresenta uma reversibilidade e repetibilidade superior a 99.98%, e um valor máximo para a sensibilidade térmica relativa de 0.04 $\%.K^{-1}$.

keywords

Crystalline silicon nanoparticles, hydrogen-termination, oxidized surface, organic functionalization, photoluminescence spectroscopy, primary luminescent thermometer, infilled films with Al_2O_3.

abstract

The understanding of the luminescence properties of silicon at nanoscale is a relevant subject for the development of new light emitting devices.
In this work, the emission features of crystalline silicon nanoparticles is studied. To reveal the role of the surface termination on the photoluminescence properties of silicon nanoparticles with several terminations (hydrogen, silicon oxide or organic molecules) photoluminescence in steady-state and time-resolved modes and measurements of the emission quantum yield were performed. At room temperature, the emission spectra of silicon nanoparticles terminated with hydrogen and functionalized with organic molecules, with average mean diameter of ≈3.4 and ≈2.4 nm present an emission component peaking at ≈800 and ≈750 nm, respectively. This emission component is ascribed to recombination of photogenerated excitons in the silicon core of the nanoparticles. An additional emission component peaking at higher energy, ascribed to the donor-acceptor recombination within states associated with the oxide shell is also present in the spectra of the nanoparticles with an oxide shell. The emission lifetime and quantum yield values depend on the surface termination and are discussed the role of the surface termination int the inter- and intra-nanoparticle exciton transfer. The higher room temperature emission quantum yield was measured for silicon nanoparticles with organic functionalization processed as films (0.23±0.02).
Another aspect studied was the homogeneous infilling of films of silicon nanoparticles with Al_2O_3 using atomic layer deposition. The infilling allows to protect the films against oxidation and also impacts on the photoluminescence emission spectrum of the nanoparticles. This work opens new questions about the role of the surface termination and separation between nanoparticles on the emission properties.
Taking advantage from the dependence of the nanoparticles emission on temperature, an innovative primary thermometer was developed. It is shown that luminescent thermometers based on silicon nanoparticles films and solutions can operate in distinct environments with the thermometric parameter (emission peak position) described by a well-established equation. The thermometer has a reversibility and repeatability higher than 99.98% and the maximum relative thermal sensitivity is 0.04 %.K^{-1}.

Index

List of acronyms and abbreviations

ALD – Atomic layer deposition

d – Average nanoparticle core diameter

E_g – Energy band gap

FTIR – Fourier transform infrared

fwhm – Full-width-at-half-maximum

NIR – Near infrared

NP – Nanoparticle

QD – Quantum dot

R_{exp} – Expected *R*-factor

R_p – Profile value

R_{wp} – Weighted profile *R*-factor

r^2 – Coefficient of determination

SAM – Spectral angle mapper

SEM – Scanning electron microscopy

SD – Starting delay

SIMS – Secondary ion mass spectrometry

TEM – Transmission electron microscopy

UV – Ultraviolet

XPS – X-ray photoelectron spectroscopy

XRD – X-ray diffraction

η – Absolute emission quantum yield

χ^2 – Chi-square

Chapter 1. General introduction

1.1 Motivation and context

Bulk Si has been the base of the semiconductor industry and despite the research efforts on new materials, there is no obvious successor for the today's Si-based technology.[1] The technology devices that are commercially available (such as transistors and diodes) include integrated circuits that are built with bulk crystalline Si.[2] Despite the technological and commercial success of the devices based on bulk Si, the commercially available light emitting devices are not based on bulk Si, because it does not present efficient light emission due to its indirect energy band gap of 1.1 eV at 300 K.[3]

In 1990, Canham showed that quantum confinement effect yields photoluminescence from Si nanostructures at room temperature in the visible (red) spectral range.[4] This observation created the perspective of the development of light emitting devices based on Si nanostructures. Those nanostructures based on Si would present several advantages. The fact that they are made of the same element that dominates the integrated circuits market would facilitate the compatibility and integration with the current technology. Besides that, Si is one of the most abundant elements on the Earth's crust[5] and reveals good properties in terms of biocompatibility,[6] unlike elements such as cadmium and selenium that have been used for the development of nanocrystal-based light emitting devices, such as light-emitting diodes,[7] but are well known for their toxicity.[7, 8] Despite all these advantageous properties, devices based on the light emission by Si nanostructures do not have until now the same success in light emission devices when compared with the success of the bulk Si in the semiconductor industry. To improve the possibility of success of the Si nanostructures it is fundamental to understand the light emission mechanisms, such as the photoluminescence, and study how the structure of the nanostructures impact on the light emission properties.

Nanostructures based on Silicon

Nanostructures based on Si, with different sizes and shapes, have properties distinct from the ones that characterize bulk Si.[9] Si nanoparticles (NPs) are structures with size in the nanometer scale (<100 nm)[10] formed by Si atoms that may or may not have an ordered conformation. In the first case, the NPs are crystalline and in the second one they are typically amorphous.[11] These NPs can be produced with different shapes such as spherical, octahedral, cubic or even as nanowires, as shown in the scanning electron microscopy (SEM) and transmission electron microcopy (TEM) images of Figure 1.1.[12-15] Each one of these shapes has advantageous properties for specific applications, for example, in terms of the formation of structures, the shape of the NPs assumes an important role on the packing of the NPs,[14] and on the design of new devices as thin film transistors.[14, 16]

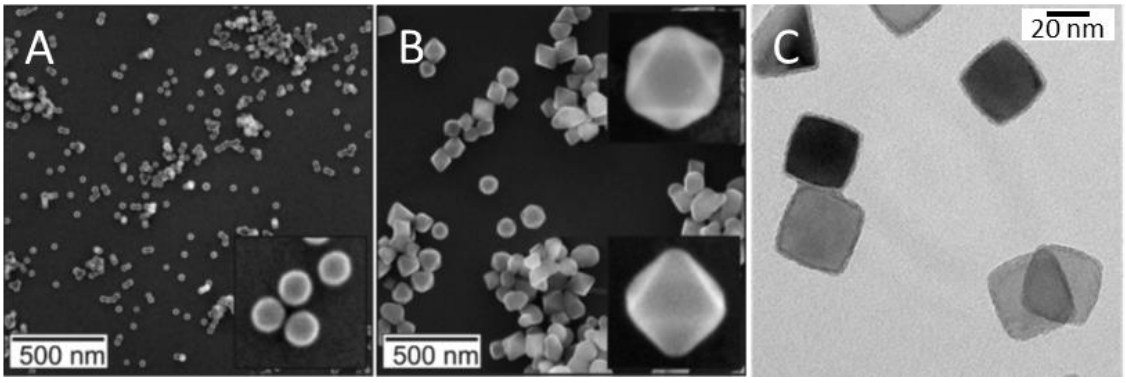

Figure 1.1 SEM images[14] of (A) spherical and (B) octahedral Si NPs and TEM image[12] of (C) cubic Si NPs.

Other examples of Si nanostructures are porous Si and Si NPs embedded in a matrix, *e.g.* silicon oxide,[17-20] ammonium silicon hexafluoride[21] or silicon nitride[22] (Figure 1.2). These structures do not contain freestanding nanocrystals but present also properties that are different from bulk Si.[23-25] Porous Si is formed by a nanocrystalline[26] or an amorphous[27] Si skeleton immersed in a disordered web of pores. The optoelectronic properties of porous Si are mainly determined by the skeleton size.[28]

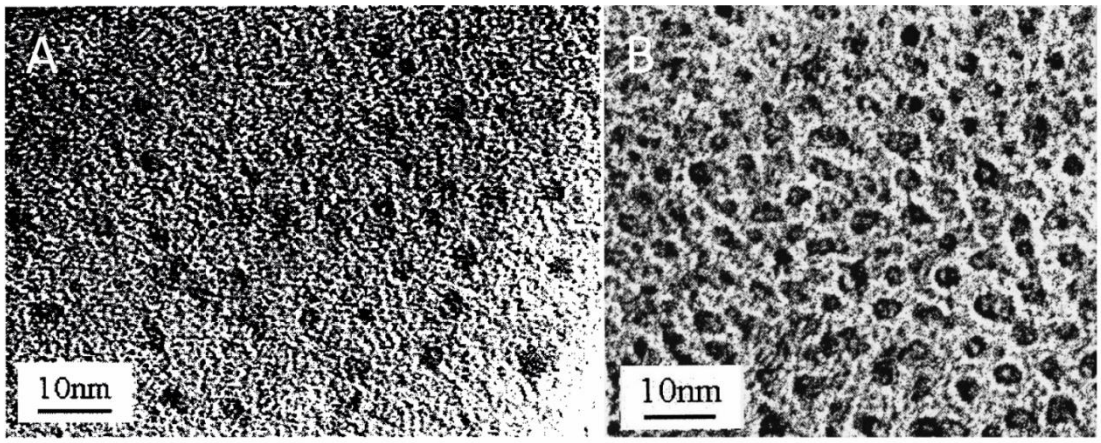

Figure 1.2 TEM images of Si NPs (dark spots) embedded in (A) silicon oxide[29] and in (B) silicon nitride.[22]

Freestanding nanocrystals are suitable systems for the study of photoluminescence properties, since there is no influence of the matrix and of the porosity on their properties, as happens in Si NPs embedded in a matrix and in porous Si.[28] For some applications the porous Si and Si NPs embedded in a matrix are systems with advantageous properties, for example porous Si is an attractive material for drug delivery.[30] Despite that, the Si NPs embedded in a matrix present some important limitations in terms of charge transport between Si NPs, because of the dielectric properties of the materials that usually constitute the matrix, such as silicon oxide.[31] Besides that, in nanostructures of Si NPs embedded in a matrix the control of the concentration of embedded NPs is not accurate.[31] The less complexity of the Si NPs also allows to predict an easier understanding of the effect of a surface modification on the photoluminescence properties.

Light emission properties of silicon nanoparticles

Bulk Si is a semiconductor characterized by a weak emission in the near infrared (NIR).[32, 33] These properties are explained by its indirect energy gap (1.1 eV) that results in long radiative decay times of free excitons, allowing nonradiative decay channels, which decrease the luminescence efficiency.[34] Differently from what happens in bulk Si, Si NPs with different surface terminations (*e.g.* hydrogen, oxide or organic molecules), or embedded in oxides, amorphous silicon oxide (SiO_x) NPs, and porous Si present emission in the visible spectral range.[35-37] The photoemission is characterized

by a broad/unstructured band with a spectral distribution that shifts from the NIR to the visible spectral regions as the size of the nanostructures is decreased. [38-40]

One of the phenomena that is indicated as being responsible for the emission in the visible range by Si nanostructures is quantum confinement.[38, 41, 42] As the nanostructures become smaller, the electrons become more confined and their position is more precisely defined, so their momenta is less precisely defined due to the Heisenberg uncertainty relations.[43] This allows radiative transitions even without the assistance of phonons, without violating the momentum conservation law, as happens in materials with direct band gap.[44, 45] This phenomenon can explain the emission in the visible range observed for Si NPs with a diameter lower than 5 nm.[38, 46] The emission spectra are characterized by a broad band that shifts to lower wavelengths (higher energies) with the decrease of the Si NPs diameter (as shown in Figure 1.3A). This behavior is attributed to an increase of the quantum confinement of the excitons, which is a consequence of the decrease of the Si NPs diameter that also results in an increase of the band gap of the Si NPs (Figure 1.3B).[38, 41]

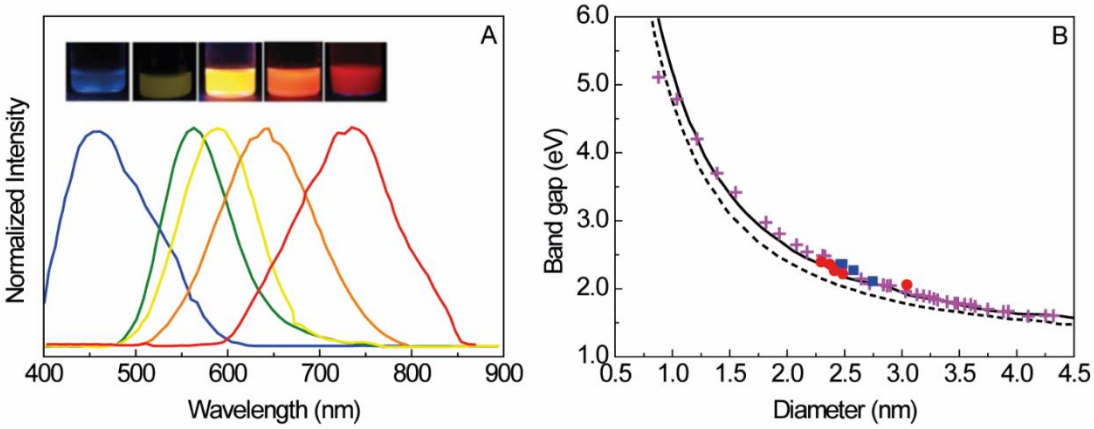

Figure 1.3 A) Emission spectra of crystalline Si NPs with different diameter values (increasing from the left to the right) in solution for an excitation wavelength of 350 nm. The photographs of each solution exposed to ultraviolet (UV) radiation (of 355 nm) are also shown.[38] **B)** Calculated (lines) and experimental results (solid symbols) for the optical band gap energies of Si NPs with different diameter.[32]

Considering that the Bohr radius of free excitons in Si is 4.9 nm,[4, 47, 48] in small hydrogen-terminated Si NPs, the phenomenon of quantum confinement can explain the blue shift of the emission spectra with the decreasing of the diameter of the Si NPs.[34, 49, 50] In larger crystalline NPs and also in other kinds of nanocrystalline Si (with different

surface termination), other phenomena, such as surface states (*e.g.* localized defect states or dangling bonds), must be considered in order to explain the emission properties.[35, 50-53]

The emission of the hydrogen-terminated Si NPs is modified by the exposure of the NPs to ambient conditions, because a native oxide shell is formed at the surface of the NPs.[54-57] This oxide shell determines important properties from the fundamental and technological point of view, like water solubility.[37, 58, 59] The oxide shell takes an important role on the luminescence properties of the Si NPs.[55, 60-62] In fact, beside quantum confinement, the alternative phenomena proposed to explain the emission properties of Si NPs are related to the oxide shell. The most studied dependence of the light emission properties of Si NPs on surface modification is the one related with the formation of an oxide shell. The formation of the oxide shell is a self-limited process[55] that can readily take place in air at room temperature.[54-57] The oxidation phenomenon can be described using the Cabrera-Mott mechanism (Figure 1.4) that includes de following steps: (i) water molecules adsorb at the surface silanol groups and aid in the cleavage of Si–Si backbonds of Si–OH; (ii) an electron is transferred from the broken bond to an adsorbed O_2 molecule; (iii) the resulting electrostatic potential forces the O_2^- drift toward the cleaved Si–Si bond; (iv) the process leads to the oxidation of this bond and of the neighboring Si–Si bond through a mechanism that involves initially formation of a disilperoxo bridge Si–O–O–Si, which is transformed into two Si–O–Si groups.[59]

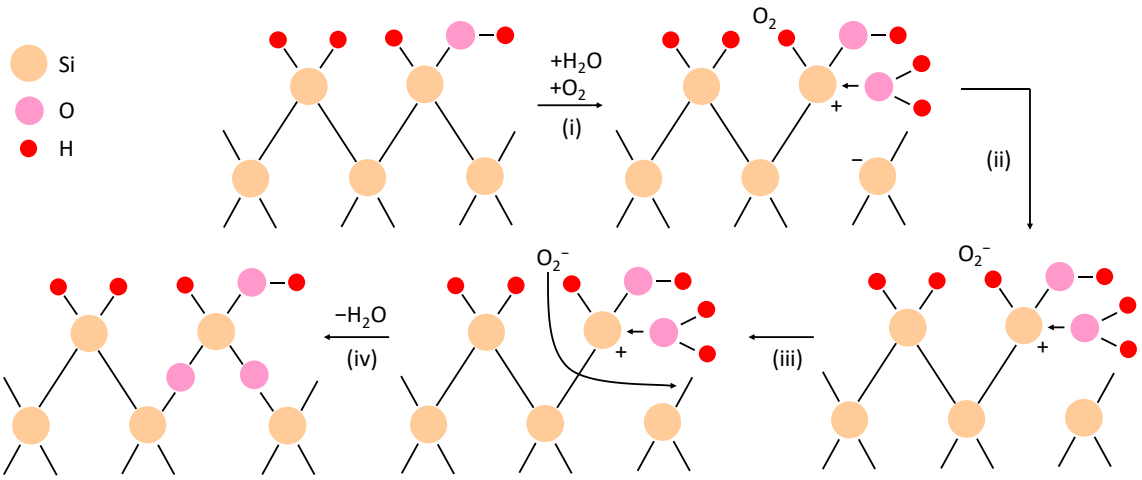

Figure 1.4 Scheme illustrating the steps of the oxidation phenomenon in the presence of water and oxygen molecules (adapted).[59]

The emission spectra of the oxidized surface Si NPs are characterized by a shift in the position of the emission band when compared with the spectra of hydrogen-terminated NPs. The majority of the studies report a blue shift after oxidation (Figure 1.5A).[31, 40, 55, 56, 60-64] This effect is attributed to the decrease of the crystalline core size after oxidation, which results in an increase of the band gap[40, 61-64] or to the appearance of defects related to the oxide formation.[55, 60-62] Other studies report a red shift[58] (Figure 1.5B) that is attributed to the introduction of trapped excitons at silanone (Si=O) bonds,[65, 66] Si–O–Si bridge bonds[58] or oxygen incorporation via passivation with group OH or oxidation.[67]

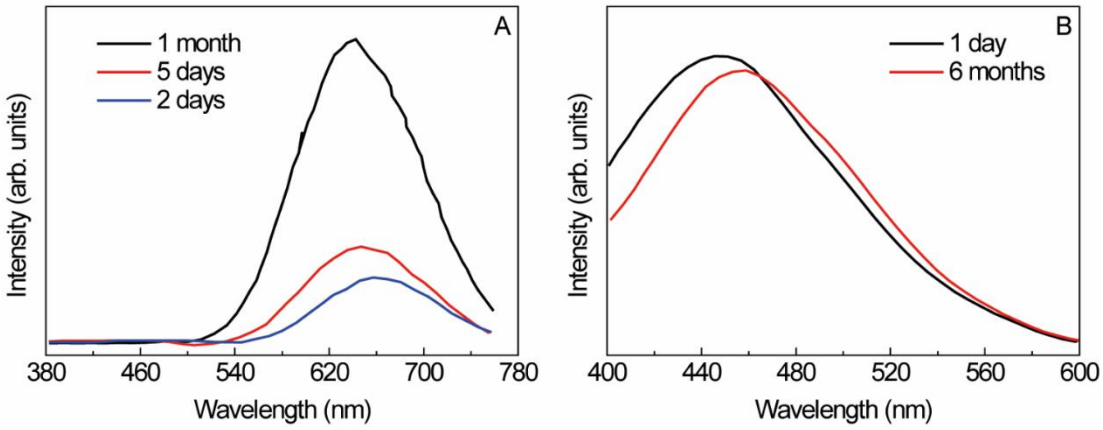

Figure 1.5 A) Emission spectra of Si NPs presenting a blue shift in the peak position with the increasing of the exposure time to air, excited at 355 nm (adapted).[63] **B)** Emission spectra of Si NPs presenting a red shift in the peak position with the increasing of the time in water, for different time intervals and excitation wavelength of 350 nm (adapted).[58]

Time-resolved photoluminescence spectroscopy also indicates that oxidation of hydrogen-terminated NPs induces the appearance of a new emission component.[68] Interesting too is the fact that some studies report a decrease of the photoluminescence intensity after air exposure,[55] but other studies report that samples only show photoluminescence, observed with naked eye, after a few hours or few days of exposure to air.[40] This effect is attributed to the progressive oxidation of the surface.[40] These experimental studies that show distinct results indicate that the origin of the photoluminescence in oxidized surface NPs is not clear yet and that it is strongly dependent on the Si NPs size and surface termination.

Organic functionalization of hydrogen-terminated NPs allows some protection against surface oxidation.[69] Despite that, the literature reports the oxidation of alkly-passivated NPs and that this effect induces changes in the emission properties of the NPs.[69] The most notorious emission property of the organic-functionalized NPs is the higher value of the emission quantum yield.[70-73] The efficiency of the emission of the Si NPs can be quantified through the emission quantum yield. The majority of the measurements reported so far were performed for NPs in solution, with an oxide shell or functionalized with organic molecules. The higher values (0.60-0.70) were reported for Si NPs suspended in mesitylene with particles size distribution centered around 2.5-4.0 nm and synthesized by nonthermal plasma and functionalized with 1-dodecene,[70] as shown in Table 1.1. The comparison between the different quantum yield values must take into attention factors such as the polarity of the solvent[33] and the excitation wavelength[74] that may influence the measured values.

It was also suggested that the functionalization eliminates nonradiative surface defects, which results in the enhancement of the emission intensity.[75] In some reports, the high absolute emission quantum yield values observed for organic-functionalized Si NPs is attributed to surface passivation and a strict avoidance of oxidation.[70-72] The studies also suggest that an efficient protection of the Si NPs from the environment using alkyl chains favors luminescence over nonradiative recombination.[76] For Si NPs functionalized with alkyl and aryl amines, surface state emission was shown to be characterized by fast recombination rates and high emission quantum yields compared to Si NPs of equivalent size with hydrogen termination.[77]

Table 1.1 Emission quantum yield values (η) of oxidized surface and organic-functionalized Si NPs in film or suspended in different solvents. The average nanoparticle core diameter (d, nm), excitation wavelength (λ_{exc}, nm), and synthesis method are also indicated.

Sample		d	Synthesis method	Surface	λ_{exc}	η
Film		3.5	Laser pyrolysis of SiH_4	Silicon oxide	–	0.30[39]
		3.4	Plasma decomposition of SiH_4		270	0.115±0.011[This work]
			Laser pyrolysis of SiH_4		–	0.09[78]
		1-2	Pyrolyze of Si_2H_6		–	0.05[23]
		2.4	Plasma decomposition of SiH_4	1-dodecene	325	0.23±0.02[This work]
		1.7		1-dodecene and silicon oxide		0.21±0.02[This work]
Suspended in	Ethanol	3.4		Silicon oxide	365	0.43±0.04[This work]
		2-3	Plasma-assisted decomposition of $SiBr_4$		360	0.24[79]
		<3	Polyoxometalate-assisted electrochemical decomposition of bulk Si			0.08-0.10[37]
	Water	4.1	Solution-phase synthesis using Mg_2Si		–	0.12[58]
	–	5	Laser pyrolysis of SiH_4		355	0.005-0.01[64]
	Toluene	–	Plasma decomposition of SiH_4		–	≈0.50[80]
	Mesitylene/ 1-dodecene	–		1-dodecene	–	0.52[72]
	Mesitylene	4			380-400	0.70[70]
	Mesitylene/ octadecene	3.9		Octadecene	360	0.62[71]
	Ethanol or hexane	1.5	Thermally degrading diphenysilane	Octanol	–	0.23[36]
	Hexane	1-3	Gas-phase based on high-pressure microdischarges		–	0.30[81]
	Water	1-2	Solution-phase reduction of $SiCl_4$	Allylamine	–	0.10[82]
	Toluene	–	Laser pyrolysis of SiH_4	Styrene	404	0.07[83]

Other effect that demonstrates the importance of the surrounding environment for the emission properties of the Si NPs is the quenching of photoluminescence that is induced by the transfer of excitons confined in Si NPs to molecular oxygen.[84-86] This phenomenon is characteristic of hydrogen-terminated NPs, being reduced by orders of magnitude if a thin oxide barrier is present.[85] Cryogenic temperatures (5-120 K) are ideal to observe this effect, as shown in Figure 1.6. With the increase of the temperature the conditions for an interaction between excitons and the molecular oxygen are reduced.[85, 86] This happens because with the increasing of the temperature a small separation distance is realized only during the short time of collisions between oxygen molecules and the Si NPs surface.[85, 86] With the increase of the temperature, the excitons' lifetime and the occupation number of the spin-triplet states of the excitons also decreases. This effect reduces the energy transfer rate to triplet ground-state oxygen molecules and the quenching of the photoluminescence.[85, 86]

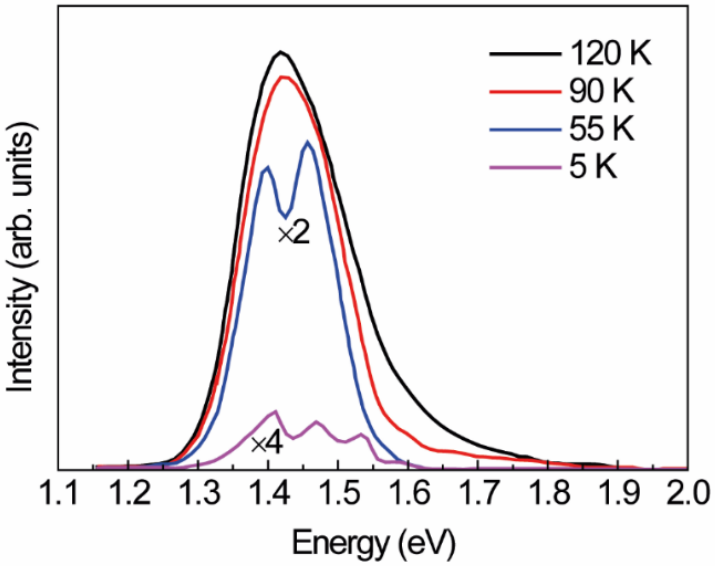

Figure 1.6 Temperature dependence of emission spectra intensity of microporous Si in oxygen ambient. Spectra at 55 and 5 K have been scaled by the indicated multiplication factor for better comparison (adapted).[85]

Despite all the research performed on Si NPs, several topics about the optoelectronic properties and specifically about the photoluminescence of the Si NPs are still open. Questions regarding the origin of the photoluminescence such as if the emission arises from defect states or from quantum confinement effects are still under debate.[50, 52, 87-89] Understanding these phenomena and how they affect the

photoluminescence properties of the NPs is a crucial step for developing new applications and also for improving the performance of the already demonstrated devices that are based on Si NPs.

Applications based on light emission by silicon nanoparticles

Taking advantage of the light emission properties of Si NPs, the development of light-emitting devices based on Si NPs, as light-emitting diodes is already a reality,[90-94] as shown in Figure 1.7. They present promising values in terms of external quantum efficiency, a parameter defined by the ratio between the number of photons emitted from the device and the number of electrons passing through the device.[95] Values up to 8.6% have been achieved.[91] This is a high value considering that other devices based on other semiconductor NPs, such as CdSe/ZnS core-shell nanocrystals and ZnSe/ZnS core-shell quantum dots (QDs) which present values of 2.7[96] and 7.83%,[97] respectively. Despite that the value is still far from the value of external quantum efficiency reported for light-emitting diodes based on CdSe/CdS core-shell quantum dots that have a value of 20.5%.[98] The light emitting devices based on Si NPs also present high brightness and long-term stable electroluminescence.[91] The emission wavelength can be tuned from the NIR to the yellow by changing the size of the Si NPs.[93]

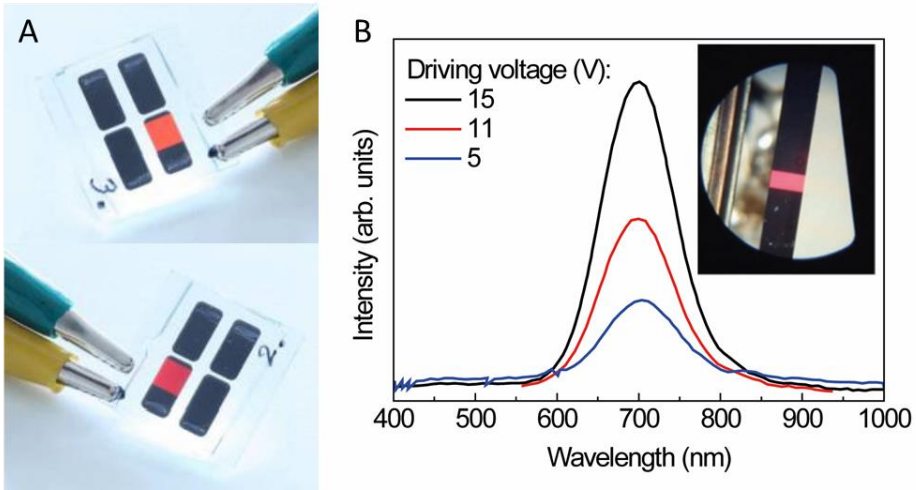

Figure 1.7 A) Photographs of Si light-emitting diodes featuring intense electroluminescence in the visible spectral region.[93] **B)** Electroluminescence spectra of hybrid nanocrystal organic light-emitting diode for different driving voltages. The inset shows a photograph of the device in ambient lighting conditions.[69]

The dependence of the photoluminescence on temperature (*e.g.* emission peak position and emission lifetime) is also one of the features that can be potentially used to the development of thermometers with size in the nanoscale as proposed by Ryabchikov *et al*, Figure 1.8.[99, 100] The light emission properties make Si NPs suitable for diagnostic imaging[101, 102] or biological labeling.[8, 103, 104]

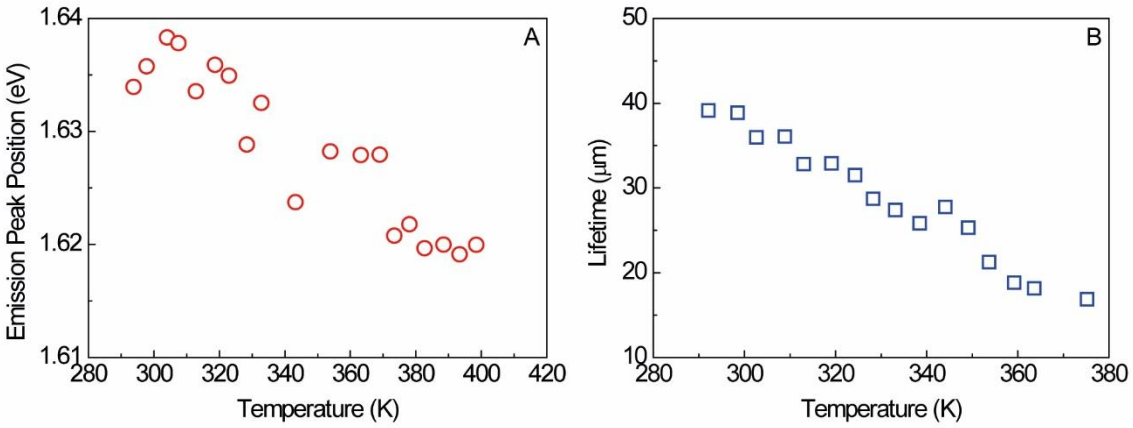

Figure 1.8 Dependence on the temperature of the (A) emission peak position and (B) emission lifetime of colloidal solutions of Si NPs functionalized with alkyl groups.[99]

1.2 Objectives of the thesis

The major objective of this thesis is the study of the photoluminescence properties of Si NPs. In order to infer how surface oxidation affects the photoluminescent properties, Si NPs with and without oxide shell, with the same average core diameter will be studied. The effect of the functionalization of the surface with organic molecules on the photoluminescent properties will also be studied and compared with the photoluminescence properties of hydrogen-terminated Si NPs.

Aiming at taking advantage of the dependence of the photoluminescence properties on the temperature, the operation of Si NPs as luminescent thermometers will also be explored.

Moreover, films of Si NPs will be infilled with Al_2O_3. This will allow to study if the Al_2O_3 deposition can provide protection against oxidation in ambient conditions and how the photoluminescence properties are affected by the Al_2O_3 deposition.

1.3 Organization of the thesis

This thesis is composed of six chapters. In chapter 1, the motivation of the work and context in which it was developed are presented.

Chapter 2 describes the experimental techniques that were more relevant to the development of the work, namely a revision about the different methods for synthesis of Si NPs, with focus on the synthesis method used to produce the Si NPs studied in this thesis and on the systems developed by the two groups that synthesized the Si NPs (the Kortshagen group from the University of Minnesota, USA, and the Wiggers group from the Universität Duisburg-Essen, Germany). The techniques used to study the photoluminescent properties are also presented, together with a brief description of the other techniques used to characterize the Si NP systems.

In chapter 3, the effect of the surface modification on the photoluminescence properties is studied for oxidized surface, hydrogen-terminated and organic-functionalized Si NPs.

Chapter 4 presents the application of the luminescent properties of Si NPs to the measurement of the temperature by presenting the Si NPs operating as primary luminescent thermometers.

In the chapter 5, the deposition of Al_2O_3 by atomic layer deposition (ALD) on films of Si NPs is presented. The films were characterized in order to study if there was a homogeneous infilling of the films with Al_2O_3 and if it is able to provide protection against oxidation in ambient conditions. The results of a study about how the Al_2O_3 affects the photoluminescence of the films are also presented.

In the last chapter, chapter 6, the general conclusions of the work and the perspectives for future work are presented.

1.4 Original contribution

The study presented in chapter 3 gives experimental evidences for the simultaneous presence of two emission components in Si NPs with a native oxide shell at the surface. One emission is due to the recombination of photogenerated electrons and holes in the crystalline core of the Si NPs and another is due to donor-acceptor recombination within states associated with the native oxide shell. The study performed

on organic-functionalized Si NPs, with and without oxidized surface, also enabled the comparison of the role of the surface terminal groups on the photoluminescent properties of the Si NPs. Two publications resulted from the work presented in chapter 3:

- "High Quantum Yield Dual Emission from Gas-Phase Grown Crystalline Si Nanoparticles" **A. M. P. Botas**, R. A. S. Ferreira, R. N. Pereira, R. J. Anthony, T. Moura, D. J. Rowe and U. Kortshagen, *J. Phys. Chem. C*, **2014**, *118*, 10375;
- "Influence of the Surface Termination on the Light Emission of Crystalline Silicon Nanoparticles" **A. M. P. Botas**, R. J. Anthony, J. Wu, D. J. Rowe, N. J. O. Silva, U. Kortshagen, R. N. Pereira and R. A. S. Ferreira, *Nanotechnology*, **2016**, *27*, 325703.

The study presented in chapter 4, about the operation of the Si NPs as luminescent thermometer, showed experimentally, for the first time, that Si NPs in film and in solution may operate in different media as primary thermometers. The work resulted in the following publication:

- "A New Generation of Primary Luminescent Thermometers Based on Silicon Nanoparticles and Operating in Different Media" **A. M. P. Botas**, C. D. S. Brites, J. Wu, U. Kortshagen, R. N. Pereira, L. D. Carlos and R. A. S. Ferreira, *Part. Part. Syst. Charact.*, **2016**, *33*, 740, **Cover Highlighted**.

The work presented in chapter 5, describes the impact on the photoluminescence properties of the infilling of Si NP films with Al_2O_3 and the protection provided against oxidation:

- "Preparation and Photoluminescence Study of Silicon Nanoparticles Films Infilled with Al_2O_3 Using Atomic Layer Deposition" **A. M. P. Botas,** J. P. Leitão, B. P. Falcão, M. Wiesinger, F. Eckmann, J. P. Teixeira, H. Wiggers, M. Stutzmann, R. A. S. Ferreira, R. N. Pereira, **to be submitted**.

Chapter 2. Experimental techniques

2.1 Methods of silicon nanoparticle synthesis

The Si NPs can be synthesized by several methods. The major goals of these methods are to get a high production rate, to produce amounts of material scalable for industrial use, and provide high quality of Si NPs.[64] This involves control in terms of the size distribution, amount of impurities, surface termination, and crystallinity of the NPs. In the following paragraphs, it is presented how the different techniques perform these tasks. The approaches of the techniques used to produce Si NPs can be classified as top-down and bottom-up (Table 2.1).[105]

In the top-down approaches, the NPs are synthesized by decomposing bulk materials (for example a crystalline Si wafer),[106, 107] with a laser[54, 56, 63, 106, 107] or using electrochemical techniques.[103, 108] Generally, these top-down techniques present limitations like a very broad particle size distribution and a specific lower limit concerning the particles size.[105] Other top-down approach consists in isolating nanocrystals that were embedded in a matrix using a chemical etching.[46, 69]

The bottom-up approaches use liquid or gaseous precursor materials in a process of nucleation, coagulation, and growth of the NPs.[105] Several techniques use this approach to synthesize NPs, such as, for instance, laser pyrolysis of silane.[40, 64, 109] Unfortunately, the distribution of particle sizes of this high-temperature process is rather wide[14, 23] and a size selection must be performed to have a smaller size distribution.[39, 81] Solution-phase synthesis techniques as thermal degradation of Si precursors[36, 110] and synthesis in inverse micelles[33, 82] are also used to synthesize Si NPs. Despite the fact that some of these techniques allow the synthesis of NPs with a narrow size distribution, the separation of the surfactant from the reaction mixture is not easy and some purification steps are necessary.[102]

The techniques that use plasmas to synthesize NPs are an attractive and versatile alternative to the above mentioned ones.[70, 111] They use plasmas to decompose the precursors (such as silane,[81, 112] silicon tetrachloride[61] or silicon tetrabromide)[79] and generate a supersaturated vapour, with subsequent particle formation.[105] The process starts with a nucleation step and the particles core grow due to the interaction anion-

molecule.[102] Thermal plasmas created by direct current arc discharges or nonthermal plasmas created by radio-frequency or microwaves can be used and the size of the NPs can be controlled by changing parameters such as the precursor concentration, the mass flow, and pressure.[105] One of the main disadvantages of the techniques that use plasma when compared with techniques such as solution-phase synthesis or electrochemical techniques is the need of specialized equipment.[102]

In the next paragraphs, the nonthermal plasma synthesis will be focused as this was the methodology chosen to prepare the NPs for the photoluminescence studies. The nonthermal plasma synthesis presents an excellent combination in terms of the amount of Si NPs that they can produce and the control over particle size, crystallinity, and morphology.[113] Several groups developed their own experimental setups to produce Si NPs using nonthermal plasma synthesis.[61, 105, 113] In the next paragraphs, the systems developed by two different groups are presented. The first system was been developed by Kortshagen group from the University of Minnesota, USA. This system has as main advantages the synthesis of Si NPs with a smaller size than that reported by other groups[114] and with low concentration of defects.[115] The second system, developed by Wiggers group from the Universität Duisburg-Essen, Germany, presents one of the highest production rates of Si NPs reported for a nonthermal plasma reactor.[105, 113]

Table 2.1 Advantages and drawbacks of several methods for synthesis of Si NPs.

	Method	Advantages	Drawbacks
Top-down approaches	Laser ablation of bulk Si	Mean size controllable in the range 2-100 nm[106]	Rather wide size distribution[106]
	Etching of bulk Si	Simplicity of the equipments[102, 103] Shape and mean size controllable in the range 1-8 nm[102, 103, 116]	Difficulty in the large scale production[102] Rather wide size distribution[100, 117] High safety risk of some of the required products (HF)[102, 103]
	Breaking down Si rich oxides	Mean size controllable in the range 2-16 nm[102, 118] Narrow size distribution[118]	Difficulty in the large scale production[102] High safety risk of some of the required products (HF)[102]
Bottom-up approaches	Reduction of silane precursors in solution	Several precursors are available[82, 102, 110]	Poor control of size[58, 102] Difficulty in tunable light emission in the entire visible spectrum[102]
	Laser pyrolyse of a gaseous precursor	Si NPs with tunable light emission in the entire visible spectrum[64, 102] Hight production rates (200 mg.hour^{-1})[102, 119]	Use of more specialized equipment[102] Rather wide size distribution[14, 23]
	Plasma synthesis using thermal plasma	Allows the production of few grams of Si NPs per hour[105]	Contamination of the Si NPs due to the degradation of the electrode material when DC arc discharges are used[105, 120]
	Plasma synthesis using nonthermal plasma	Size controllable from 2 to tens of nm[102, 112] Reports of η up to 0.72 after surface modification[70] Low agglomeration of the Si NPs without adding surfactants[113] Hight production rates (10 g.hour^{-1})[105]	Use of more specialized equipment[102, 105, 113]

The Kortshagen group developed a reactor (Figure 2.1A and 2.1B) that uses radio-frequency and produce NPs (Figure 2.1C) with a core size smaller than 3 nm to a few tens of nanometers.[105, 112] The size distribution of the Si NPs is well described by a

log-normal distribution (Figure 2.1D and 2.1E).[70] This type of distribution typically indicates that coagulation and sintering of particles are important factors in this synthesis method.[113] The production rate of the NPs depends on their size. A production rate of 14.4 mg.hour^{-1} for Si NPs with a size of 2-4 nm is reported (52 mg.hour^{-1} for larger ones).[112] In terms of process yield an almost complete conversion of the silane into Si NPs is reported.[112] With this system, it is possible to control the conditions that allow the production of NPs with surface close to 100 % termination with Si–H bonds. This is an important fact considering that hydrogen in an excellent passivating agent for surface states and also that the hydrogen termination is required for the surface modification with organic molecules known as hydrosilylation.[72, 102]

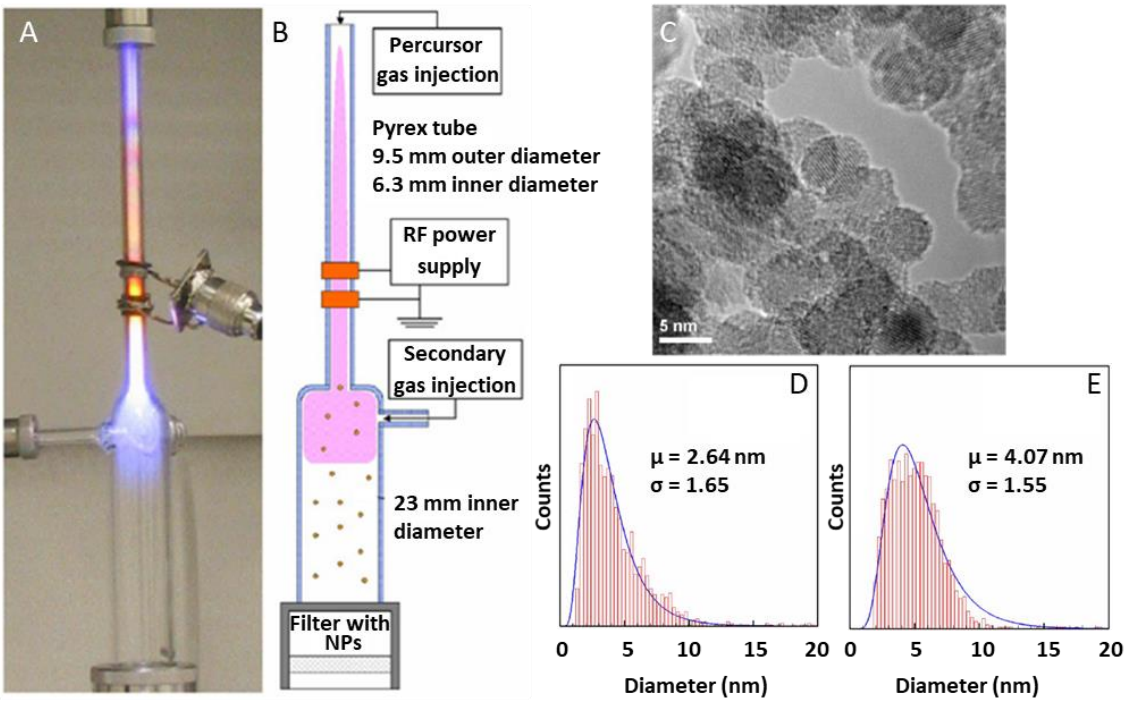

Figure 2.1 Photograph (A) and sketch (B) of a nonthermal plasma reactor developed by Kortshagen group (adapted).[70] The sketch indicates the region of injection of the precursor gases and the region of injection of the secondary gas. TEM image (C) of the Si NPs synthesized in the nonthermal plasma reactor[113] and particle size distribution (D and E) of two different samples of Si NPs with a log-normal distribution [the mean (μ) and the standard derivation (σ) values of the distribution are also indicated].[70]

Through a hydrosilylation reaction, it is possible to attach organic molecules to the surface of the NPs, which can improve properties as the emission quantum yield to values as high as 0.60-0.70.[70] The control of the synthesis conditions also enables the

synthesis of Si NPs with extremely low defect content (0.002-0.005 defects per NP for Si NPs of 4 nm in size).[115]

The Wiggers group developed a reactor based on a microwave-induced plasma that allows the production of highly pure material with a high production rate (from 0.7 to 10 g.hour^{-1}) in the form of powder, as shown in Figure 2.2A. The technique produces mostly single crystalline particles with soft-agglomeration. A TEM images of soft-agglomerated Si NPs in shown in Figure 2.2B. Differently from hard-agglomerated Si NPs (Figure 2.2C), the points of contact between the NPs of the soft-agglomerates are very small.[105] The mean size of the Si NPs can be tuned between 4 and 50 nm by changing the experimental conditions.[105] Both experimental setups developed by Kortshagen and Wiggers groups allow the n- or p-type doping by adding into the reactor phosphine (PH_3) or diborane (B_2H_6), respectively.[31, 105, 121-124]

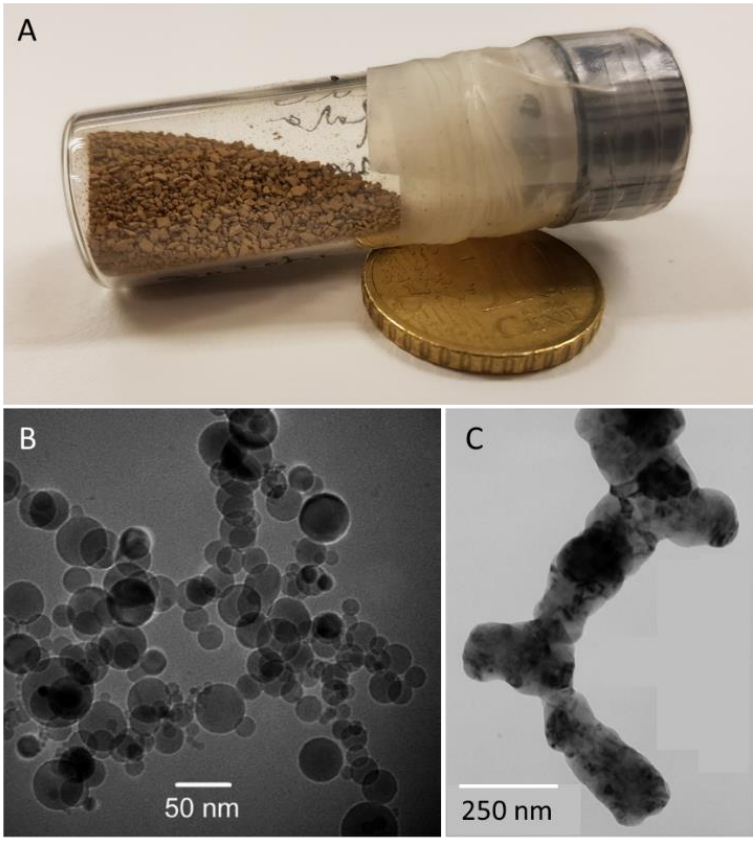

Figure 2.2 A) Photograph of Si NP powder (≈20 mg) synthesized in a nonthermal plasma reactor developed by Wiggers group. TEM images of (B) soft- and (C) hard-agglomerated Si NPs.[105]

Preparation of the samples studied in the thesis

Hydrogen-terminated Si NPs (identified as **as-prepared H-terminated Si NPs**) were synthesized, by Kortshagen group at the University of Minnesota, USA, in a nonthermal radiofrequency (13.56 MHz) flow-through plasma reactor, as the one presented in Figure 2.1, through the dissociation of injected silane.[72] The system consisted of a borosilicate glass tube equipped with two copper ring electrodes used to apply the RF power. A mixture of 5 % of silane (SiH_4) in He was used as precursor gas at a flux of 13 sccm and the carrier gas was Ar at a flux of 35 sccm. The pressure in the reactor was kept constant at 1.4 Torr by using an electronically controlled throttle valve. Hydrogen gas was injected into the plasma afterglow at a flow of 100 sccm to reduce surface dangling bond defects.[115] Hydrogen-terminated Si NPs were collected from the plasma as a powder using a mesh. To avoid surface oxidation, the as-grown Si NPs were transferred under nitrogen from the synthesis reactor to a nitrogen-purged glovebox (oxygen and moisture level below 30 ppm). The Si NPs were afterwards removed from the glovebox and kept under ambient conditions for about one month. As know from previous investigations,[59, 115] during this time a natural oxide shell of 0.3±0.1 nm thickness is formed on the Si NPs surface.[59] The resulting Si NPs are identified as **oxidized surface Si NPs.** The native oxide shell is replaced with hydrogen termination,[125] by etching the NPs in an aqueous HF solution (10 % in volume) for three minutes followed by rinsing with ethanol. The resulting hydrogen-terminated Si NPs (identified as **H-terminated Si NPs**) were afterwards dispersed in toluene and the solution was spin-coated onto a glass substrate, forming a film of randomly distributed Si NPs, with which photoluminescence measurements were carried out. These procedures were done inside a nitrogen-purged glove box (oxygen below 300 ppm).

Hydrogen-terminated Si NPs (identified as **Si NPs-H**) were synthesized using the same procedure described above, but using an Ar flow of 80 sccm. Part of the **Si NPs-H** were functionalized with 1-dodecene under air-free conditions in a hydrosilylation reaction, as described by Anthony *et al.*[72] For this, the Si NPs-H were mixed with a 5:1 (in volume) solution of mesitylene and 1-dodecene, following ≈2 hours of heating at 488 K under nitrogen-purged refluxing conditions. After this the Si NPs formed a clear colloidal solution. Following functionalization with 1-dodecene the Si NPs (hereafter

termed as **Si NPs-C12**) were dried, redispersed in chloroform, filtered through a 200 nm PTFE filter, and dried again. After preparation the **Si NPs-H** and **Si NPs-C12** were kept in vials that were sealed under nitrogen atmosphere inside a glove box (oxygen below 1 ppm) to avoid surface oxidation. Part of the **Si NPs-C12** were afterward removed from the glovebox and kept under ambient conditions for about one month, yielding to the formation of a natural oxide shell on the Si NPs surface. The Si NPs-C12 with natural oxide shell are identified hereafter as **Si NPs-C12-O**. Films of Si NPs were prepared by drop casting on ISO 8255-1 glass substrates from Normax. For this, solutions of **Si NPs-H** and **Si NPs-C12** were prepared in toluene (Sigma-Aldrich, 99.9 %) and films were cast inside a nitrogen purged glovebox (oxygen below 300 ppm) where then were kept until the measurements.

Hydrogen-terminated Si NPs were synthesized through the same procedure used for **Si NPs-H** but using an Ar flow of 100 sccm. After growth, the hydrogen-terminated Si NPs were functionalized with 1-dodecene in a thermal hydrosilylation reaction for ≈4 hours using the same procedure described above for **Si NPs-C12**. The resulting Si NPs are called **as-prepared Si NPs-C12**. After functionalization, the **as-prepared Si NPs-C12** were suspended in toluene (Sigma-Aldrich, anhydrous, 99.8%) with a concentration of 4.0 M and kept in a vial that was sealed and maintained in a nitrogen-purged glove box (oxygen below 1 ppm). Films of **as-prepared Si NPs-C12** were prepared by drop casting onto Si wafers (Sieger Wafer) under nitrogen atmosphere (with oxygen level below 0.1 ppm and moisture below 0.1 ppm). Si NPs with silicon oxide on the surface were obtained by air exposure for ≈7 months of two solutions of **as-prepared Si NPs-C12** with concentrations ≈0.1 M and ≈1.0 M. In average, the interaction of the Si NPs with oxygen and water molecules is stronger for the low concentrated solution, because the amount of these molecules per Si NP is higher. This yields Si NPs with a larger oxide shell (smaller crystalline core) in the lower concentration solution when compared with the more concentrated solution. The Si NPs with silicon oxide on the surface resulting from the solutions with 1.0 M and 0.1 M are termed as **Si NPs-C12-1** and **Si NPs-C12-2**, respectively. For the photoluminescence measurements, the **Si NPs-C12-2** were suspended in toluene in a dilute concentration of 0.49 M.

Free-standing Si NPs in the powder form and with a surface terminated with Si-H bonds were synthesized from gas phase in a silane plasma by Wiggers group at the

Universität Duisburg-Essen, Germany.[126] The mean diameter (*d*) is 4.9±0.9 nm, 5.5±1.1 nm and 18±3 nm, determined using the Brunauer-Emmett-Teller (BET) method.[127] Considering that the as-grown Si NPs suffered some exposure to ambient conditions that leads to the formation of amorphous silicon oxide on the surface of the Si NPs to recover a hydrogen-termination of the Si NPs, it was performed an HF wet etching. The NP powder is moistened with ethanol and mixed in excess with an aqueous HF solution (10 % in volume) for 10 min. After the suspension is mixed with chlorobenzene (Sigma-Aldrich, anhydrous, 99.8 %), as the Si NPs become hydrophobic (hydrogen-terminated) they are transferred into the chlorobenzene, which is separated from the HF solution due to its different density. In a subsequent step, the HF aqueous solution is removed from the chlorobenzene suspension by centrifuging (2 min at 5000 rpm). The precipitate is then mixed with a fixed volume of chlorobenzene to achieve a cloudy suspension containing 1 % in weight of hydrogen-terminated Si NPs.

Thin films of Si NPs were deposited on Si substrates (CrysTec, 1 cm × 1 cm), previously coated with an Au layer with a thickness of 130 nm, using the spray coating technique (homemade system) with a distance between the spray needle and the substrate (heated at 323 K) in the range 12-14 cm. Films of hydrogen-terminated Si NPs were deposited, using the solutions described in the previous paragraph inside a N_2-purged glovebox (oxygen concentration below 0.2 ppm) to avoid reoxidation of the Si NPs. Samples labeled in this work as **Si NPs (*d* nm)** correspond to films of hydrogen-terminated Si NPs with the mean diameter *d*. Films of oxide-terminated Si NPs (air exposed, unetched) were also deposited for comparison purposes using the same spray system, but using solutions of Si NPs, in which HF wet etching was not performed, in ethanol solvent. Immediately before spray deposition, all solutions were ultrasonicated in a water bath with a temperature between 278 and 293 K. The spray coating deposition yields films with a controlled thickness by applying different numbers of spray cycles (each cycle with a spray time of 0.5 s with a time between sprays of 20 s).

Al_2O_3 was deposited in a homemade ALD system. Depositions were performed at 448 K using alternating pulses of trimethylaluminum (0.2 s) and water (0.5 s), a purge time of 45 s, and at a base pressure of 1 mbar. The performance of the system was tested for these experimental conditions by measuring the growth rate of the Al_2O_3 deposited on a H-terminated Si wafer. For that a growth rate of 1.0 Å per cycle has been

obtained, which is in agreement with an ALD process with the growth of one mono layer per cycle.[128-130] Samples hereafter labeled as **Si NPs (*d* nm) + Al_2O_3** correspond to films of hydrogen-terminated Si NPs with mean diameter *d* on which Al_2O_3 has been deposited.

Table 2.2 presents a list of the samples studied in the thesis.

Table 2.2 Si NP samples studied in the thesis. *d* is the average diameter of the Si core.

	Sample	Surface termination	*d* (nm)	Processed as
Chapter 3	**as-prepared H-terminated Si NPs**	Hydrogen	4.0±0.1	Film
	oxidized surface Si NPs	Silicon oxide	3.4±0.1	Suspended in ethanol
	H-terminated Si NPs	Hydrogen		Film
	Si NPs-H		2.4±0.1	
	Si NPs-C12	1-dodecene		
	Si NPs-C12-O	1-dodecene and silicon oxide	1.7±0.1	
Chapter 4	**as-prepared Si NPs-C12**	1-dodecene	2.0±0.2	
	Si NPs-C12-1	1-dodecene and silicon oxide		
	Si NPs-C12-2			Suspended in toluene
Chapter 5	**Si NPs (18 nm)**	Hydrogen	18±3	Film
	Si NPs (18 nm) + Al_2O_3	Aluminium oxide		
	Si NPs (5.5 nm)	Hydrogen	5.5±1.1	
	Si NPs (5.5 nm) + Al_2O_3	Aluminium oxide		
	Si NPs (4.9 nm)	Hydrogen	4.9±0.9	
	Si NPs (18 nm) + Al_2O_3	Aluminium oxide		

2.2 Photoluminescence spectroscopy

Photoluminescence is defined as the spontaneous emission of photons (in an energy range between the NIR and the UV) from the excited electronic states, after being excited by absorption of photons (in an energy range between the NIR and the UV).[45, 131] The emission of photons is the result of the radiative recombinations that occur after the excitation. In the next paragraphs, the main radiative transitions in semiconductors are briefly described.

When radiation reaches a semiconductor material part of the photons with an energy E can be absorbed leading to the excitation of electrons from the valence band to the conduction band if E is larger or equal to the energy band gap E_g (represented as i in Figure 2.3). If the energy is larger than the E_g the electrons are excited to levels at energy higher than the bottom of the conduction band. The radiative recombination of the electrons from the high energy levels of the conduction band to the valence band (ii in Figure 2.3) is not likely to happen, with exception of high pure single crystals. Usually, there are other competing processes that lead to the transition from levels of the condition band at higher energies to the bottom of the conduction band, as the thermalization achieved by phonon emission (iii in Figure 2.3) or less frequently by phonon-assisted radiative transitions.[45] After thermalization the electrons at the bottom of the conduction band can recombine radiatively to the valence band (iv in Figure 2.3).

The excitation of an electron to the conduction band creates a hole in the valence band. The electron and the charge can move independently but due to the Coulomb attraction between these two opposite charges, an interacting electron-hole pair can be created.[131] This pair is called exciton and can move without contributing to the electrical conductivity because of its neutral charge. Using a simple model, the excitons can be modeled by a hydrogen atom-like structure. In this model, two types of excitons can occur in crystalline materials: the weakly bound excitons (also known as Mott-Wannier excitons or simply Wannier excitons)[132] and the tightly bound excitons (also known as Frenkel excitons).[131] The Frenkel excitons are localized in the vicinity of an atomic site and have much smaller radius than the Mott-Wannier excitons.[131] They occur in molecular crystals.[48] Wannier excitons have a large radius in comparison to the interatomic distances.[131] The Wannier excitons are also called free excitons, as their wavefunction is strongly delocalized and they can move freely inside the crystal.[48] The Wannier excitons occur mainly in semiconductors.[48] The excitons can recombine (C in Figure 2.3), leading to an emission with an energy

$$E = E_g - E_b \tag{2.1}$$

where E_b is the binding energy between electron and hole.[131]

The existence of defects or impurity atoms, either intentionally (doping) or as residual impurities will lead to an attraction of the excitons due to van der Waals interactions.[48, 132] The exciton will be then bound to these neutral donor (D^0) or acceptor (A^0).[132] The donor-bound exciton (D in Figure 2.3) an acceptor-bound exciton (E in Figure 2.3) can recombine, leading to an emission with an energy

$$E = E_g - E_b - E_{bx} \tag{2.2}$$

where E_{bx} is the binding energy between D^0 and exciton or A^0 and exciton.[45]

Other recombinations are the ones between an electron bound to a donor and a hole bound to an acceptor (F in Figure 2.3), the recombination between a free electron and a neutral acceptor (G in Figure 2.3) and the recombination between a donor and a free hole (H in Figure 2.3).[45] The energy of the photon that results from these radiative transition is

$$E = E_g - E_D - E_A + \frac{e^2}{\varepsilon r} \tag{2.3}$$

where E_D and E_A are the energy levels of the donor and acceptor, respectively, ε is the dielectric constant, e is the electronic charge, and r is the average distance between donor and acceptor. [45, 133]

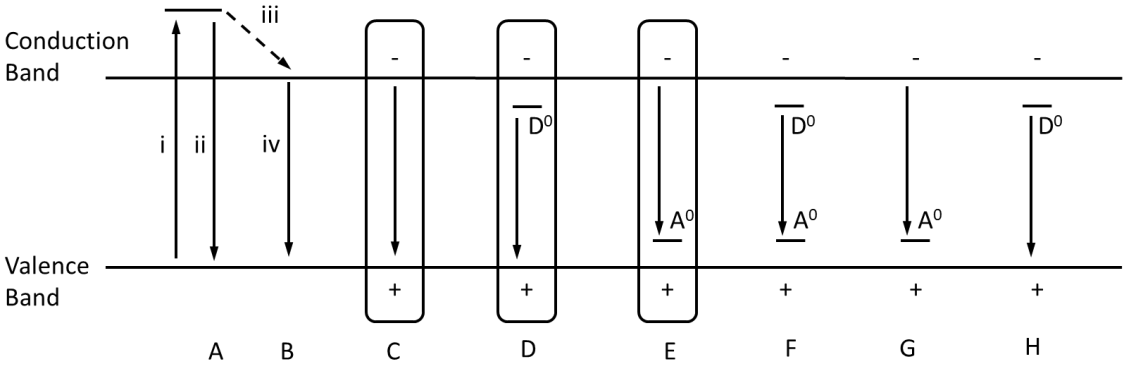

Figure 2.3 Scheme illustrating radiative transitions in semiconductors (adapted).[45, 134]

The intensity of the emission that results from the radiative transitions is dependent on the excitation power (P_{exc}) and, with exception of experiments where P_{exc} is varied more than two orders of magnitude and in experiments where the

excitation energy is resonant with E_g,[134] follows a power law $I_{em} \sim {P_{exc}}^{k}$, with $1 < k < 2$ for exciton type emissions and $k < 1$ for donor-acceptor type emission.[134-136]

Photoluminescence spectroscopy is a technique used to study the emission and excitation spectra of a given sample.[45] A typical experimental layout diagram is shown in Figure 2.4. The main elements are the excitation source, that can be a monochromatic excitation source as a laser beam or other excitation source with a broad emission range, typically a Xe arc lamp, in which the excitation wavelength in selected by using a monochromator (the excitation monochromator). The excitation radiation reaches the sample and the emitted radiation is collected by a focusing lens and using a second monochromator (the emission monochromator) the photons with a selected wavelength can be collected to the detector.[131]

The result of the measurement is a spectrum. If the excitation wavelength was fixed and the emitted light intensity is measured at different wavelengths by scanning the emission monochromator the result is an emission spectrum. If the emission monochromator is fixed to a certain emission wavelength and the emitted light intensity is measured while the excitation wavelength is scanned for several excitation wavelengths, the result is an excitation spectra.[131]

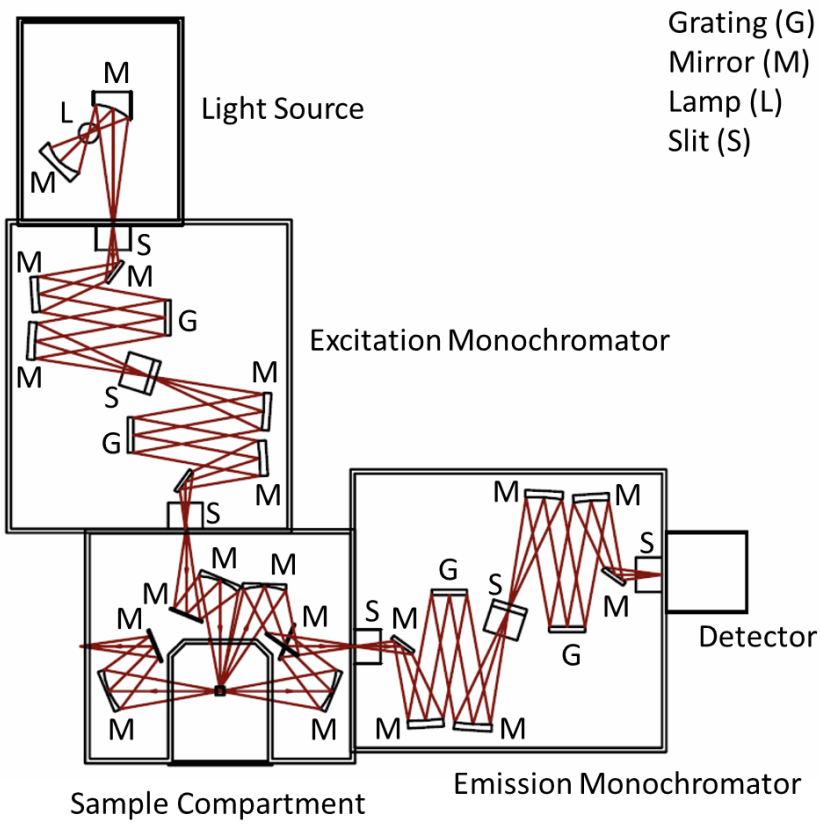

Figure 2.4 Schematic diagram of a spectrofluorometer used in the present studies (adapted).[137]

The photoluminescence measurements can be performed in two distinct modes: steady-state mode (also known as stationary optical excitation) and time-resolved mode. In the stationary mode the excitation and the measurement of the spectrum are performed at the same time, as there is a continuous excitation. In the time-resolved mode the measurements are performed using a pulsed excitation source, which allow a time delay, called starting delay (SD), between the end of the excitation and the beginning of the emission measurement.[131] Time-resolved mode allows the study of the decay kinetics responsible for the emission and the determination of the experimental lifetime of the excited emitting state, as the emission decay curve can be measured.

The photoluminescence measurements reported in chapter 3 were carried out at 12 K and at room temperature using a Fluorolog-3 modular double grating excitation spectrofluorometer with a TRIAX 320 emission monochromator from Horiba Scientific, coupled to a R928 photomultiplier from Hamamatsu, using a 450 W Xe arc lamp as excitation source (Figure 2.5). Emission spectra (acquired using front-face and right-

angle modes for sample in film and solution, respectively) were corrected for the spectral response of the monochromators and detector using the correction spectrum provided by the manufacturer. The excitation spectra intensity (I_{exc}) was corrected for the spectral distribution of the lamp intensity (R) recorded using a photodiode reference detector, yielding to the corrected spectra intensity (I_{exc}/R). In the case of the **Si NPs-H** the low relative intensity values between 240-280 nm, lead to an artificial increase of the corrected spectra intensity.

The excitation irradiance was quantified using a Field MaxII-TOP power meter from Coherent, coupled to a OP-2 VIS high-sensitivity Si photodiode optical sensor from Coherent (diameter of 7×10^{-3} m), yielding average irradiance values of 0.5 W.m^{-2} in the excitation wavelength range (365-525 nm), ensuring that overexcitation artifacts can be neglected in the low-temperature measurements.[138] The time-resolved emission spectra and emission decay curves were acquired with the same instrumentation using a pulsed Xe–Hg lamp (6 μs pulse at half width and 20–30 μs tail). The films were measured in vacuum (10^{-6} Pa), inside a helium-closed cycle cryostat.

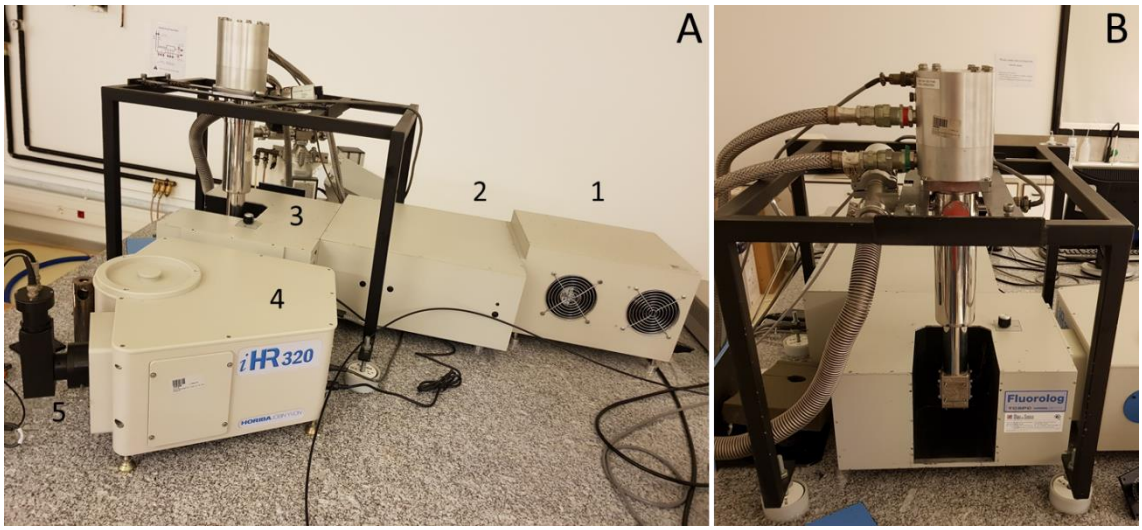

Figure 2.5 Photographs of (A) the Fluorolog-3 spectrofluorometer and of (B) the helium-closed cycle cryostat used to perform the photoluminescence measurements. The number identify the main elements of the spectrofluorometer: (1) excitation source, (2) excitation monochromator; (3) sample compartment; (4) emission monochromator and (5) detector.

The emission spectra reported in chapter 4, of **as-prepared Si NPs-C12**, **Si NPs-C12-1** and **Si NPs-C12-2** in film were recorded under vacuum (13-480 K) and in air with the Fluorolog-3 spectrofluorometer. The nominal spectral dispersion of the

spectrofluorometer is 2.64 nm.mm^{-1}, yielding a spectral resolution of 2×10^{-3} eV (slits width of 0.1 mm) in the visible range. The temperature was varied using a helium-closed cycle cryostat, a vacuum system (4×10^{-4} Pa), and a Lakeshore 330 auto-tuning temperature controller from Lakeshore, with a resistance heater. All the measurements began at least 300 s after temperature indicated in the temperature controller remained constant, thus ensuring the samples thermalization and constant temperature during the measurement.

Emission spectra of the Si NPs (in solution and in film) were measured in air and under nitrogen atmosphere (inside a glove box at 400 Pa with oxygen concentration below 14 ppm and moisture below 27 ppm) using a Maya2000 Pro portable spectrometer from Ocean Optics and a LED light as the excitation source. The temperature was varied using a Kapton thermofoil heater from Minco, mounted in a Cu holder and coupled to a IES-RD31 temperature controller. The temperature was measured using a K-type thermocouple from VWR, with accuracy of 0.1 K, enabling the determination of the real temperature surrounding the Si NPs. In the solutions, the thermocouple was immersed in Quartz Suprasil cuvette from Hellma Analytics, whereas in the film samples was placed in direct contact with the films substrate. All the measurements began at least 300 s after the thermocouple temperature readout remained constant, thus ensuring the samples thermalization and the collection of each spectrum at a constant temperature.

Photoluminescence measurements reported in chapter 5 were performed with a Vertex 80v Fourier transform infrared spectrometer from Bruker, equipped with InGaAs and Si detectors. The emission spectra were corrected for the response of the detectors. During the measurements the samples were kept at 8 K using a helium gas flow cryostat. The 457.9 nm line of an 85-BLS-305 diode-pumped solid-state laser from Melles-Griot was used as the excitation source (laser spot diameter is ≈2 mm), with the power being varied using neutral density filters from Edmund Optics. For each measurement the excitation power was measured at the front of the spectrometer entrance window with a Model 842-PE optical power meter from Newport.

The hyperspectral microscopy images were performed using a BX51 brightfield microscope from Olympus (10× objective), in the reflection mode, equipped with a Retiga 4000R digital CCD camera from QImaging used to capture the microphotographs

(exposure time of 20 ms) of the films under illumination of white light of a DC-950 DC regulated illuminator from Fiber-Lite. The microscope is also equipped with a hyperspectral imaging system from CytoViva that includes a IPX-2M30 digital camera from Imperx coupled to a V10E 2/3" spectrograph from Specin (30 µm slit, nominal spectral range of 400–1000 nm, and nominal spectral resolution of 2.73 nm), used to perform the hyperspectral microscopy in bright field reflection mode under UV illumination from a LLS-365 LED light from Ocean Optics (emission at 365 ± 25 nm). The hyperspectral scanning is vertical and each image results from 696 lines (20 s per line) and each pixel field-of-view on the hyperspectral images corresponds to 1.3 × 1.3 μm^2 on the sample plane. The spectral angle mapper (SAM) classification was performed using the ENVI 4.8 software, after applying the Savitski–Golay curve fit smoothing (width 33 and degree 2) in order to reduce the spectra noise.

2.3 Absolute emission quantum yield

The photoluminescence can be quantified by the emission quantum yield, which is a direct measure of the conversion of absorbed photons into emitted photons,[139] and is defined as

$$\eta = \frac{N_{em}}{N_{abs}} = \frac{\int_{\lambda_1}^{\lambda_2} \frac{\lambda}{hc}\left[I_{em}^{sample}(\lambda) - I_{em}^{reference}(\lambda)\right] d\lambda}{\int_{\lambda_3}^{\lambda_4} \frac{\lambda}{hc}\left[I_{exc}^{sample}(\lambda) - I_{exc}^{reference}(\lambda)\right] d\lambda} \tag{2.4}$$

where N_{abs} and N_{em} are the number of photons absorbed and emitted by a sample, respectively, h is the Planck's constant, c is the speed of the light in vacuum, I_{em}^{sample} and $I_{em}^{reference}$ are the emission intensities of the measured with and without a sample respectively, in the emission spectra wavelength interval [λ_1,λ_2] and I_{exc}^{sample} and $I_{exc}^{reference}$ are the integrated intensities of the excitation radiation measured with and without a sample respectively, in the excitation wavelength interval [λ_3,λ_4].[140] The η measurements can be classified as absolute or relative measurements.[139] The main difference between these two types of measurements is that relative measurements are performed with conventional spectrofluorometer, which can only detect a certain fraction of the emitted light, so relative measurements require a standard with known

η and optical properties, namely energy ranges of absorption and emission, closely matching those of the sample that is being studied, and the measurement is performed by comparing the integral emission spectra of the sample and the standard obtained under identical measurement conditions.[141] The absolute measurements do not need quantum yield standards[139] and are obtained using an integrating sphere, as the one shown in Figure 2.6. This allows to detect all the light emitted from the excited sample, and so the η can be determined by measuring the number of emitted photons and the number of absorbed photons. The number of absorbed photons is determined by the difference between the number of photons, with an energy corresponding to the excitation wavelength, measured with the sample inside the integrating sphere and measured with a blank in the sample position.[139]

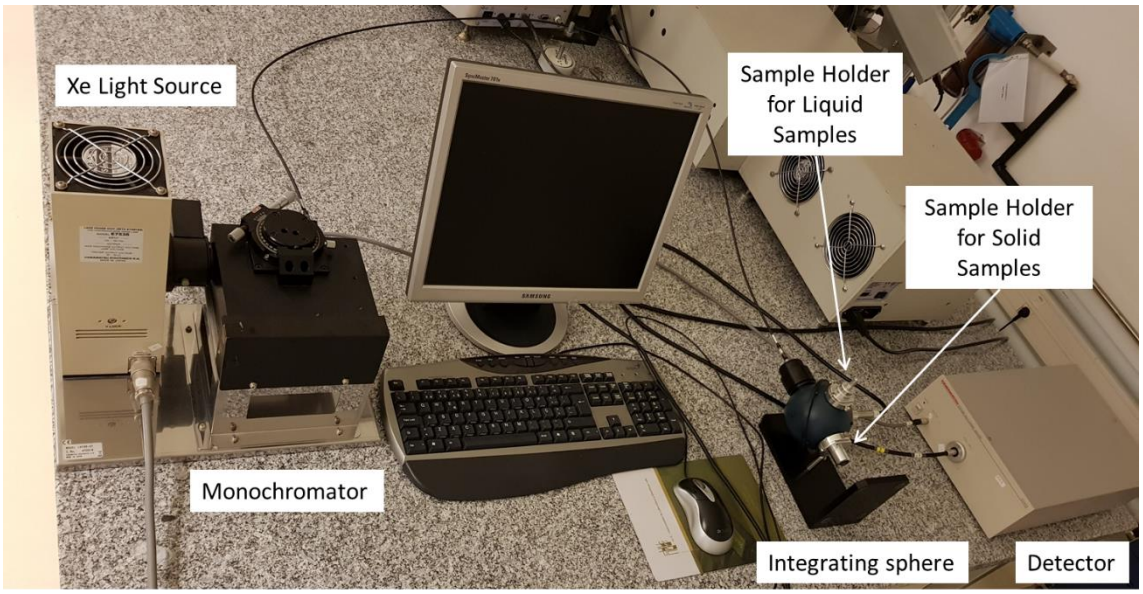

Figure 2.6 Photograph of the integrating sphere and setup used to measure the absolute emission quantum yield.

The absolute emission quantum yield measurements were performed at room temperature using the C9920-02 setup from Hamamatsu with a 150 W Xe lamp coupled to a monochromator for wavelength discrimination, an integration sphere as sample chamber and a multichannel analyzer for signal detection. Three measurements were made for each sample and the average values obtained are reported with accuracy within 10 % according to the manufacturer. The measurements were performed, under ambient conditions, immediately after removing the samples from the cryostat used to perform the photoluminescence measurements.

2.4 Structural characterization techniques

2.4.1 X-ray diffraction

The X-ray diffraction (XRD) is an experimental technique that allows the determination of physical characteristics of the materials, such as the average crystallite size. The technique is based on the interaction between the X-ray beam incident on the sample and the atoms of the sample.[142] When a X-ray beam incides on a crystalline sample it is diffracted by the crystal planes. Depending on the atomic arrangement, there will be a constructive interference between the scattered rays.[142] The conditions for the constructive interference are described by the Bragg law

$$2d_p sin\theta = n\lambda \tag{2.5}$$

where d_p is the spacing between diffracting planes, θ is the incident angle, n is an integer number and λ is the wavelength of the X-ray.[3, 142]

In a diffraction experiment, it is called powder to a sample that consists of a large number of small randomly oriented crystallites.[142] If the number of crystallites is sufficiently large, there will be enough crystallites in any diffracting orientation to give reproducible diffraction patterns.[142] The crystallite size (L) by using the Sherrer equation

$$L = \frac{K\lambda}{\text{fwhm}\ cos\theta} \tag{2.6}$$

where fwhm is the full-width-at-half-maximum of the diffraction peak in radians, and K is a constant in the order of unity,[143] being 0.9 a good approximation.[144]

Figure 2.7 illustrates one of the setups that can be used to perform XRD measurements. The setup is formed by an X-ray source, a sample holder, and a detector. Between the source and the sample there are primary optics as the Soller slits that correct the angular divergence and the divergence slit that controls the beam spread. Between the sample and the detector there is the secondary optics as the anti-scatter slit that changes the geometry of the system, the Soller slit that limits the beam height and the Beta-filter that filters K_β rays and white radiation.[145]

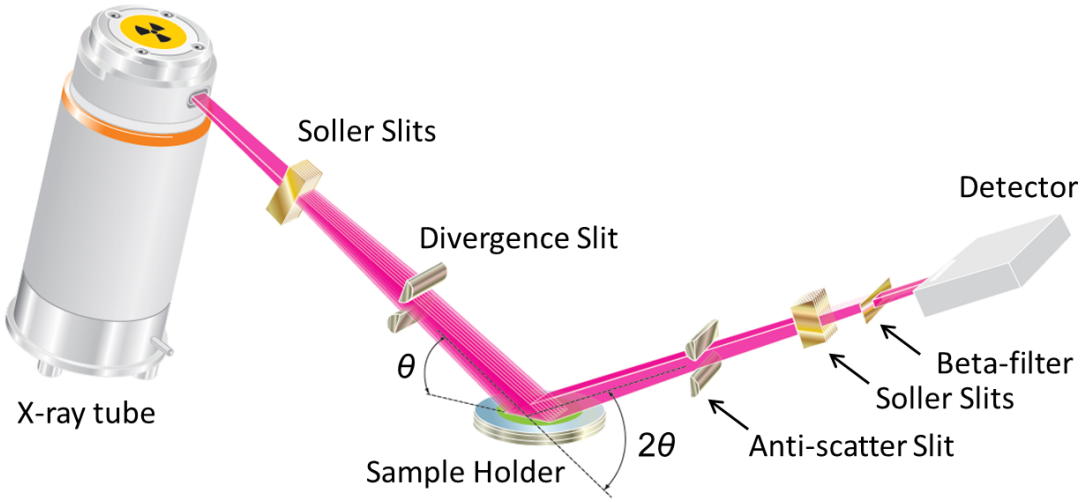

Figure 2.7 Schematic diagram of the setup used to the XRD measurements (adapted).[146]

Rietveld refinement allow to interpret XRD data. The method is based on the calculation of a profile using a model that is fitted until it matches with the measured profile, using a least squares refinement.[142] Among others, the Rietveld method can adjust parameters as the lattice parameters, atomic positions, preferred orientation, background function and overall scale factor. The method requires as input information initial values of the adjusted parameters, step-scan data in equal increments, the starting and ending values of 2θ, and the wavelength of the X-ray.[142] The evaluation of the quality of the fit and the determination of when the refinement can be stopped can be performed by checking the *R*-values, which are useful to communicate and compare results.[142, 147] Despite that, the best way to evaluate the success of the refinement is the comparison between the calculated and the measured diffraction patterns together with the evaluation of the chemical/physical plausibility of the parameters that were determined.[142]

The **H-terminated Si NPs** XRD pattern was recorded using an AXS microdiffractometer from Bruker, with a 2.2 kW sealed Cu X-ray source. The sample consisted of a glass covered with Si NPs and was prepared by firmly pressing the glass substrate onto the Si NP powder. The XRD patterns of **Si NPs-H** and **as-prepared Si NPs-C12** were recorded using a D8 Discover from Bruker, equipped with a CoK_{α} (1.79 Å) radiation source. The XRD patterns of **Si NPs-C12** and **Si NPs-C12-O** were recorded using an AXS microdiffractometer from Bruker and an Empyrean powder X-ray diffractometer from Panalytical, respectively. The samples were exposed to CuK_{α} radiation (1.54 Å) at

room temperature. For the XRD measurements, the Si NP powder was firmly pressed onto a Si sample holder form VDL Enabling Technologies Group, under ambient conditions. The XRD patterns of **Si NPs-H** and **Si NPs-C12** were recorded with integration times of 300 s (to prevent oxidation) and the XRD pattern of **Si NPs-C12-O** was recorded with integration time of 12 hours.

Rietveld refinements used in the analysis of the XRD data were performed using the FullProf package.[148] The size effects were treated with the integral breadth method considering a Thompson-Cox-Hastings pseudo-Voigt convoluted with axial divergence asymmetry function to describe the peak shape. The contribution of the instrument to the peaks broadening was determined by the refinement of the XRD pattern of a LaB_6 standard sample (NIST ref. 660a). The contribution of the finite size of the NP crystallites to the peaks broadening was taken into account by an isotropic model yielding an apparent average size. The background was modelled using polynomials of degree five (for samples **Si NPs-H**, **Si NPs-C12** and **Si NPs-C12-O**) and six (for sample **as-prepared Si NPs-C12**). The quality of the refinement was evaluated by calculating the profile value (R_p), weighted profile *R*-factor (R_{wp}), expected *R*-factor (R_{exp}), and Chi-squared (χ^2).[149]

2.4.2 Fourier transform infrared spectroscopy

The Fourier transform infrared (FTIR) spectroscopy is a characterization technique that can be used to identify functional groups in a molecule based on its vibrational modes at different infrared frequencies.[150] The measurements are performed using a FTIR spectrometer that is based in a Michelson interferometer (Figure 2.8). The interferometer is formed by a fixed mirror, a moving mirror, and a beam splitter. An infrared beam reaches the beam splitter, it is divided into a beam that goes to the fixed mirror and other beam that goes to the moving mirror. The beams are reflected by each of these mirrors and come back to the beam splitter, where they combine into a new beam that passes through the sample and reaches the detector. The combination of the two beams produces a pattern that is called interferogram.

The interferogram is composed by a sum of all the interference patterns created by each wavelength in the beam, as a function of the optical path difference. The intensity as a function of the optical path can be considered as a function in the time

domain, as the optical path depends on the positions of the moving mirror that is time dependent. The Fourier transformation from the time (t) domain to frequency (ν) domain is obtained from

$$F(\nu) = \frac{1}{\sqrt{2\pi}} \int_{-\infty}^{\infty} f(t) e^{-i\nu t} dt \tag{2.7}$$

The Fourier transformation of the interferogram allows to convert the intensity versus optical path difference to intensity versus wavenumber ($\tilde{\nu}$),[131, 151] because $\tilde{\nu}$ is related with the frequency by the equation

$$\tilde{\nu} = \frac{\nu}{c} = \frac{1}{\lambda} = \frac{E}{hc} \tag{2.8}$$

where E is the photon energy.[131]

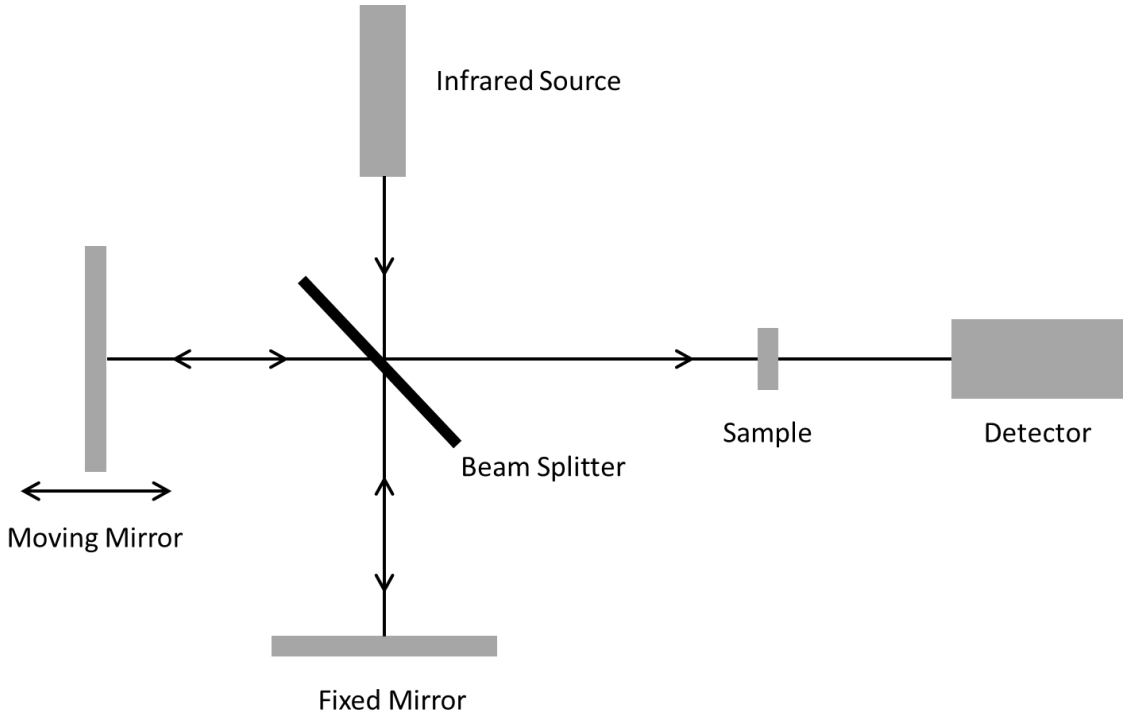

Figure 2.8 Schematic diagram of a setup used to the FTIR measurements that uses a Michelson interferometer.

The vertical axis in the FTIR spectrum is often presented by transmittance ($T_{ransmit}$)

$$T_{ransmit}\,(\tilde{\nu}) = \frac{I(\tilde{\nu})}{I_0(\tilde{\nu})} \tag{2.9}$$

where $I(\tilde{\nu})$ is the intensity transmitted by the sample and I_0 is the intensity incident on the sample.[131, 151] The absorbance (A) can be calculated form the $T_{ransmit}$ using[152]

$$A = -log_{10}(T_{ransmit}) \tag{2.10}$$

The FTIR spectroscopy measurements presented in chapter 3 were performed with a nitrogen-purged Nicolet Series II Magna-IR System 750 equipped with a glowbar light source, a KBr beam splitter, and a mercury-cadmium-telluride detector. All spectra were recorded in diffuse reflection mode at room temperature with a resolution of 2 cm^{-1} and averaged over 1000 scans. The samples consisted of an Au-coated Si wafer, covered with Si NPs. These were prepared inside a glove box by firmly pressing the respective substrates onto the Si NP powder. The samples transfer from the glovebox to the spectrometer was carried out using a gas-tight chamber that was sealed inside the glovebox. Once the chamber was opened, the samples were immediately introduced in the spectrometer and the measurements were started. A bare Au-coated Si wafer was used to measure the background reference.

The FTIR spectroscopy measurements presented in chapter 5 were performed under vacuum (2 Pa) with a Vertex 70v spectrometer from Bruker Optics equipped with a glowbar light source and recorded in reflection mode with a resolution of 1 cm^{-1} and 300 scans. In the used measurement configuration, the incident radiation crosses the sample film and is reflected by the underneath Au layer following a second transmission across film and goes to the detector, which corresponds to a measurement of the intensity (I) after the incident radiation crosses the sample two times. The transmission (T_{rans}) in a given sample was determined from $T_{rans} = \frac{I}{I_0}$, where I_0 is the intensity measured in the same configuration for a reference sample, made of a Si wafer coated with an Au layer with a thickness of 130 nm. The corresponding absorption (A_{bsor}) was determined from $A_{bsor} = -log_{10}(T_{rans})$. The area of the different FTIR bands was estimated by integration after performing a linear baseline correction in the wavelength range of the integration.

2.4.3 Raman spectroscopy

Similarly to FTIR spectroscopy, Raman spectroscopy can provide information on chemical structures and physical forms and identify substances from the characteristic spectral patterns.[153] In this technique, monochromatic radiation (usually from a laser) is used to irradiate a sample. After reaching the sample, part of the radiation is scattered in an elastic process (Rayleigh scattering) that results in radiation with the same wavelength than that of the incident one, and a small percentage of the radiation is scattered in an inelastic process (Raman scattering) that results in radiation with a wavelength different from that of the incident one. In Rayleigh and Raman scattering processes, an electron is excited due to the incident radiation from the ground level to a short-lived state called "virtual state", because the incident radiation does not match the energy difference between the ground state and the excited states, and so only distorts (polarizes) the cloud of electrons. The electron excited from the ground level to the "virtual state" can fall to the original ground level resulting in the scattering of radiation with the same energy (Rayleigh scattering) or to a vibrational level of the ground level, which results in radiation with lower energy (Stokes Raman scattering). Other possibility is the electron being excited from a vibrational level of the ground level to a "virtual state" and then falls to the ground level, which lead to radiation scattered with higher energy (anti-Stokes Raman scattering).[154]

A Raman spectrum consists in scattered intensity plotted vs. wavenumber. In order to get a representation of the Raman spectra independent of the excitation wavelength the scattered intensity is represented as a function of the Raman shift

$$Raman\ shift\ (\lambda_{scattered}) = \frac{1}{\lambda_{incident}} - \frac{1}{\lambda_{scattered}} \qquad (2.11)$$

where $\lambda_{incident}$ and $\lambda_{scattered}$ are the wavelengths of the incident and scattered photons.[154]

Raman scattering measurements were performed in backscattering configuration in a Jobin-Yvon LabRam HR 800 spectrometer equipped with a Peltier-cooled (203 K) CCD detector and using a 50× long focal distance objective (0.5 numerical aperture), which resulted in a probing spot radius of ≈0.7 μm. The measurements were

done with the 532 nm line of a diode-pumped solid-state laser (Laser Quantum) at a lower power density (<10^3 W cm^{-2}).

2.4.4 Brunauer-Emmet-Teller method

The Brunauer-Emmet-Teller (BET) method is a gas adsorption spectroscopy technique that can be used to determine the mean diameter of NPs.[127, 155] The adsorption is described through an isotherm, which is a model that describes the volume of adsorbate gas on the adsorbent surface as a function of the gas pressure at constant temperature. This expression is[127]

$$\frac{P}{V_{ad}(P_0 - P)} = \frac{C-1}{V_{mono}C}\frac{P}{P_0} + \frac{1}{V_{mono}C} \tag{2.12}$$

where P is the equilibrium pressure and P_0 is the saturation pressure. P_0 is defined as the pressure at which no further gas is adsorbed to the surface upon increasing P. The parameter V_{ad} is is the volume of gas adsorbed and V_{mono} is the volume of gas forming a monolayer on the surface. C is the BET constant

$$C = e^{-\frac{E_X - E_L}{R_g T}} \tag{2.13}$$

where, E_X is the adsorption energy for the first monolayer, E_L is the adsorption energy for the other layers, R_g is the gas constant, and T is the temperature. In the application of the BET method, the V_{ad} is measured as a function of P, and V_{mono} and C are obtained by modelling the experimental data with the Equation (2.12), in a pressure range $0.05 < \frac{P}{P_0} < 0.35$, where the plot of $\frac{P}{V_{ad}(P_0-P)}$ as a function of $\frac{P}{P_0}$ is approximately linear.[127] The surface area (S) of the sample is given by

$$S = V_{mono} N_A \Phi \tag{2.14}$$

where N_A is the Avogadro constant and Φ is the adsorption cross section of the gas molecules. For spherical particles the average mean diameter (d) can be calculated from[155]

$$d = \frac{6m}{\rho S} \tag{2.15}$$

where m is the mass of the sample and ρ is the mass density.

Measurements with the BET method were performed by Wiggers group at the Universität Duisburg-Essen, Germany, using nitrogen gas at 77.4 K with an adsorption cross section of the gas molecules of 16.2×10^{-16} cm^2.

2.4.5 Electron microscopy

Electron microscopy uses a beam of electrons to create an image of the sample that is being studied. The main advantage of the electron microscopy when compared with the optical microscopy, which uses photons to create the image, is that electrons have a smaller wavelength than that of the photons used in the optical microscopy (≈300-700 nm), allowing measurements with a much larger spatial resolution.[156] For example, electrons emitted into vacuum from heated filament and accelerated through a potential difference of 50 V, have a velocity of 4.2×10^6 m/s and their wavelength is 0.17 nm.[156] For an optical microscope the best possible spatial resolution is ≈0.3 μm (for a wavelength of 500 nm), but a modern transmission electron microscope has resolution below 0.2 nm and a scanning electron microscope can provide resolution between 1 and 10 nm.[156]

Two types of electron microscopy can be distinguished, the TEM, which uses the electrons that reach the sample (primary beam) and that are transmitted through the sample, and the SEM, which detects electrons that are emitted from the surface (secondary electrons) due to excitation by the primary electron beam.

Both SEM and TEM equipments are formed by an electron gun, which is the source of the primary electrons, condenser lens, which focus the electrons onto the sample using a magnetic field, and an objective system.[156] SEM contains scanning coils to deflect the electron beam allowing to scan the surface of the sample and detector that converts the secondary electrons into light allowing to get an image.[156] TEM contains projector lens that allow to produce a direct image or diffraction pattern on a phosphor screen that emits light under electron bombardment.[156]

SEM images of films were obtained in this thesis using a microscope NVision 40 from Zeiss. TEM images of Si NPs deposited onto ultrathin carbon on Au grids were acquired with a FEI Titan aberration-corrected microscope.

2.4.6 X-ray photoelectron spectroscopy

X-ray photoelectron spectroscopy (XPS) is a technique used to investigate the chemical composition of surfaces. In an XPS measurement, the sample is irradiated by a X-ray beam that interacts with the atoms in the surface region.[157, 158] Due to the photoelectric effect, this leads to the emission of electrons with an kinetic energy (KE)

$$KE = h\nu - BE - W \tag{2.16}$$

where BE is the binding energy of the atomic orbital from which the electron originates, and W is the spectrometer work function.[157-159] The binding energy corresponds to the energy difference between the initial and final sates after the photoelectron has left the atom.[157] Each element has a unique set of binding energies, allowing the XPS to be used to identify and determine the concentration of the elements in the sample surface (typically in a depth between 0 and 10 nm).[158, 159]

An XPS setup is composed by an X-ray source, an energy analyzer, and a detection system. The energy analyzer is a concentric hemispherical analyzer also called hemispherical sector analyzer, whose function is to select the electrons with a specific energy.[159] Considering that the environment in which the measurement is performed needs to assure that the photoelectron emission is not affected by any external electrostatic or magnetic fields, allowing the maximum number of photoelectrons to reach the detector, and to avoid contamination of the surface, the measurements are performed in ultra-high vacuum (pressure below 10^{-9} mbar).[159]

XPS measurements presented in chapter 5 were performed with a FlexMod XPS setup from SPECS equipped with a monochromatized XR50 X-ray source, Al Kα radiation (1486.71 eV), and a Phoibos 150 hemispherical analyzer from SPECS, plus an electron beam heating element. The pressure was maintained at 2×10^{-10} mbar during the measurements.

2.4.7 Secondary ion mass spectrometry

Secondary ion mass spectrometry (SIMS) is a mass spectrometric technique that is based on bombarding the surface of a solid sample with ions (primary ions). SIMS provides information about the composition of the surface by analyzing the emitted secondary ions. This destructive technique can be used to detect all elements and is particularly advantageous due to its sensitivity (for example Si can be detected in a concentration of ≈0.4 ppb) and depth resolution (from 2 to 30 nm).[160, 161] Two different modes can be used in SIMS, the static SIMS, which examines the elemental and molecular distribution present over the outmost monolayer of the material surface, and the dynamic SIMS, which examines the elemental and molecular distribution as a function of the depth by using ions with enough density to remove more than the surface monolayer.[160, 161]

The basic components of a setup for SIMS measurements are an ion gun generating the primary ion beam (such as Cs^+, O_2^+, O^-), a mass filter that separates the ions according their mass to charge ratio, and a detector.[160, 161] In order to allow the ions to move freely in the chamber and to reduce the adsorption of residual gas species on the sample surface, the measurements are performed in ultra-high vacuum.[161]

Secondary ion mass spectrometry presented in chapter 5 was performed by Probion Analysis for the elements C, O, Al, Si and Au, in an analyzed region with a diameter of 60 µm, using Cs^+ primary ions with impact energy of 2.5 keV.

Chapter 3. Surface dependence of the photoluminescence properties[162, 163]

3.1 Introduction

Previous studies,[39, 40] explain the photoluminescence properties of Si NPs based on the quantum confinement model that does not take into account the possibility of co-existence of an excitonic-related emission and of an emission associated with surface/interface states. Moreover, little has been established about the effect of inter-NP interactions (*e.g.* inter-NP energy/charge transfer) on the photoluminescence properties of Si NP ensembles. Because of that, the emission of Si NPs with the same diameter but distinct surface terminations are studied using photoluminescence spectroscopy in steady-state and time-resolved modes. Experimental evidences for the simultaneous contribution of two recombination mechanisms to the photoemission of Si NPs with silicon oxide shell are given. The role of the inter-NP charge transfer on the light emission is also studied. It is found that an increase in the inter-NP separation towards non-interacting Si NPs leads to an enhancement of the emission quantum yield, which is rationalized in terms of competition between radiative recombination and nonradiative inter-NP charge transfer.

The light emission properties of organic-functionalized Si NPs will also be studied to discuss the role of the surface on the photoluminescent properties. Despite the advantageous properties of the organic-functionalized Si NPs, such as the higher emission quantum yield when compared to, for example, hydrogen-terminated and Si NPs with an oxide shell at the surface with the same size (as shown in Table 1.1, section 1.1), the way how the surface termination determines intra- and inter-NP interactions and how the optical properties are affected by these interactions is still not clear. In order to study these interactions, the light emission properties of hydrogen-terminated Si NPs and Si NPs functionalized with organic groups (1-dodecene) with the same size are studied through photoluminescence spectroscopy in time-resolved and steady-state modes as well as by quantum yield measurements. The goal is to elucidate

the role of the surface conditions on the dynamics of photoexcited charges and on the recombination processes concurrent with light emission. Moreover, from the photoluminescence temperature dependence, the role of thermally-activated processes in the effective recombination of photogenerated charges is discussed. It is demonstrated that despite the fact that most of the works consider that functionalization affects the luminescence by changing the passivation properties of individual NPs (*e.g.* functionalization eliminates surface nonradiative defects), it is shown that the surface functionalization changes the photoluminescence properties also by changing the inter-NP exciton transfer.

3.2 Results and discussion

3.2.1 Structural characterization

The XRD pattern of the **as-prepared H-terminated Si NPs** is shown in Figure 3.1A. In the diffractogram, the most intense reflections appear ≈28.5°, 47.7°, and 56.6°, corresponding to (111), (220) and (311) Si crystal planes, respectively.[18, 164] From the first peak the mean diameter of the NPs was estimated to be 4.0±0.1 nm using the Scherrer equation, presented in section 2.4.1, Equation (2.6). The obtained diameter is in good agreement with values estimated by TEM, as shown in the inset of Figure 3.1A.

The FTIR spectra of the **as-prepared H-terminated Si NPs** (Figure 3.1B) show the bands at 866 and 908 cm^{-1} associated with deformation modes of Si-Si-H_3 and scissor and wag modes of Si_2-Si-H_2[165] and the band ≈2100 cm^{-1} attributed to Si-H stretching vibrations of Si_3-Si-H, Si_2-Si-H_2, and Si-Si-H_3 surface hydride groups.[59] The spectra suggest minute contamination with Si-O-Si bonds, as shown from the low intensity of the band between 1050-1150 cm^{-1} ascribed to Si-O-Si bonds,[59, 115] in good agreement with the idea that **as-prepared H-terminated Si NPs** are terminated with Si-H bonds. The FTIR spectra of the **oxidized surface Si NPs**, that kept under ambient conditions for about one month, show a band in the region 1050-1150 cm^{-1} due to Si-O-Si bonds (stretching) and a band at 2255 cm^{-1} due to O_3-Si-H bonds (stretching), both from the surface oxide, and band with a lower relative intensity due to Si_{4-X}-Si-H_X (X =

1, 2, 3) hydrides, as it is typically observed for Si NPs with a fully developed native oxide shell.[59, 115] This is in good agreement with the development of a native oxide shell on the Si NPs surface. Previous investigations performed on Si NPs with 5.5±0.1 nm under ambient conditions for the same period of time, found a native oxide shell thickness of 0.3±0.1 nm.[59] Thus, after air exposure, the Si NPs have a mean diameter of 3.4±0.1 nm and a surface shell of native silicon oxide.

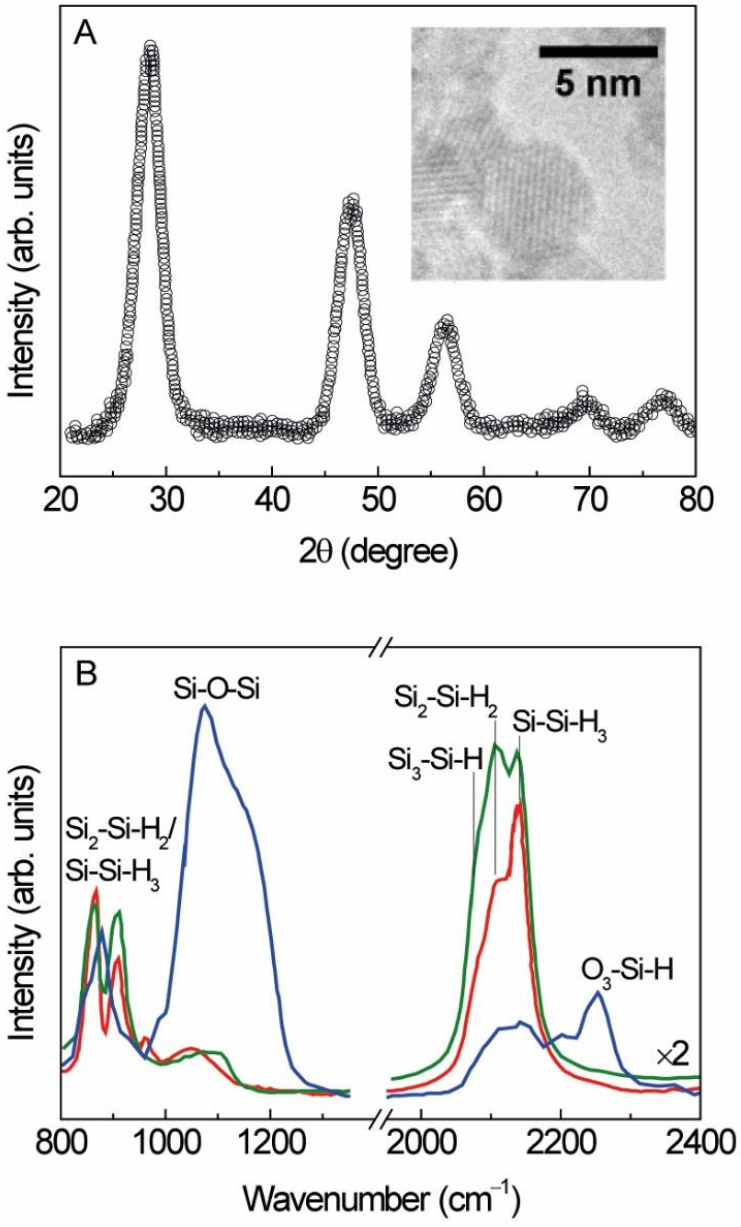

Figure 3.1 A) XRD pattern and TEM image (inset) of **as-prepared H-terminated Si NPs** before exposure to ambient conditions. **B)** FTIR spectra recorded for **as-prepared H-terminated Si NPs** (red line), **oxidized surface Si NPs** (blue line) and **H-terminated Si NPs** (green line).

After etching the **oxidized surface Si NPs** with HF solution (sample identified as **H-terminated Si NPs**), the band attributed to Si-O-Si is not observed in the FTIR spectrum (Figure 3.1B). Instead it is possible to observe the Si_2-Si-H_2/Si-Si-H_3 and Si_{4-X}-Si-H_X (X = 1, 2, 3) signals, which indicates that the HF etching leads to hydrogen-terminated Si NPs.

The XRD diffraction patterns were measured for **Si NPs-H**, **Si NPs-C12** and **Si NPs-C12-O**. These are shown in Figure 3.2A. In the diffractogram of **Si NPs-H** the most intense reflections appear at ≈33.0°, 55.5°, and 66.2°, and in the diffractograms of **Si NPs-C12** and **Si NPs-C12-O** these appear at ≈28.4°, 47.4°, and 56.1°, corresponding to (111), (220) and (311) Si crystal planes, respectively.[18, 164] The difference in the position of the reflections is due to the difference in the wavelength of the used radiation sources. The peaks are clearly broadened with respect to bulk Si, as expected for samples composed of NPs. The average apparent diameter of the Si crystallites is 2.4±0.1 nm (**Si NPs-H** and **Si NPs-C12**) and 1.7±0.1 nm (**Si NPs-C12-O**). The size-reduction upon air exposure points out that a native oxide shell with a thickness of ≈0.4 nm was grown on the **Si NPs-C12-O**.

The FTIR spectra of **Si NPs-H**, **Si NPs-C12**, and **Si NPs-C12-O** were measured in order to evaluate the surface termination of the Si NPs (Figure 3.2B). The spectrum of **Si NPs-H** reveals bands characteristic of hydrogen termination in the 830-950 cm^{-1} region, associated with deformation modes of Si-Si-H_3 and scissor and wag modes of Si_2-Si-H_2,[165] and at 2000-2150 cm^{-1} with three components located at 2095, 2113 and 2135 cm^{-1}, attributed to Si-H stretching vibrations of Si_3-Si-H, Si_2-Si-H_2, and Si-Si-H_3 surface hydride groups, respectively.[59] Relatively weaker bands characteristic of the Si-H stretching vibration modes are also observed in the FTIR spectra of **Si NPs-C12** and **Si NPs-C12-O**, which is dominated by bands due to CH_2/CH_3 stretching and deformation modes in the regions 2800-3000 and 1420-1490 cm^{-1}, respectively.[70] It is noted that in the spectra of **Si NPs-C12** and **Si NPs-C12-O**, the absence of the peaks at ≈3080 cm^{-1} (assigned to =C–H stretching modes), at ≈1640 cm^{-1} (assigned to C=C stretching modes), and at 997 and 912 cm^{-1} (assigned to CH=CH_2 out of plane bending mode), indicating the successfully bonding of the 1-dodecene to the Si NPs surface.[70] The spectrum of **Si NPs-C12-O** also displays a band within 1000-1250 cm^{-1} attributed to Si-O-Si bonds, in good agreement with the formation of a native oxide shell.[59]

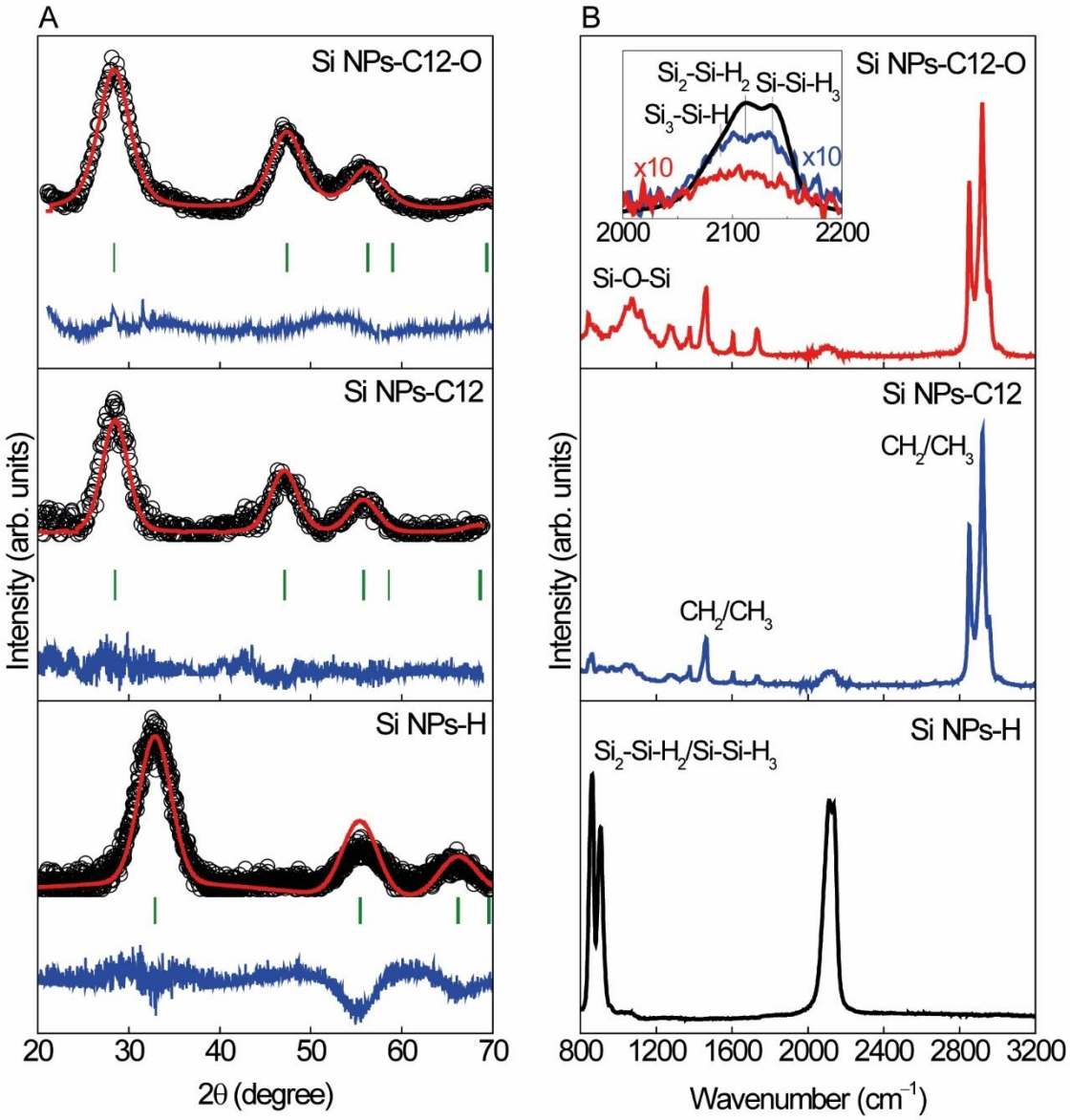

Figure 3.2 A) XRD patterns of **Si NPs-H**, **Si NPs-C12** and **Si NPs-C12-O**. Continuous (red) line corresponds to Rietveld refinement of Si phase (**Si NPs-H**: R_p=33.1 %, R_{wp}=40.6 %, R_{exp}=22.6 % and χ^2=3.22; **Si NPs-C12**: R_p=30.8 %, R_{wp}=37.2 %, R_{exp}=22.5 % and χ^2=2.73; **Si NPs-C12-O**: R_p=15.3 %, R_{wp}=14.1 %, R_{exp}=5.94 % and χ^2=5.67). Vertical (green) lines represent the position of allowed Bragg peaks, while (blue) lines represent the fit residues. **B)** FTIR spectra recorded for **Si NPs-H**, **Si NPs-C12** and **Si NPs-C12-O**. The inset shows a magnification of the region within 2000-2200 cm^{-1}.

3.2.2 Photoluminescence properties

Oxidized surface and hydrogen-terminated silicon nanoparticles

The emission spectra of the **oxidized surface Si NPs** were recorded at different excitation wavelengths at 12 K and at room temperature and are shown in Figure 3.3A

and B, respectively. The room temperature emission spectra, excited between 300 and 410 nm, display a broad emission in the red spectral region, peaking at ≈808 nm (1.54 eV) and with a fwhm of ≈250 meV (Figure 3.3B). Increasing the excitation wavelength to 520 nm, the emission spectrum shifts to the red by ≈8 meV (Figure 3.3B).

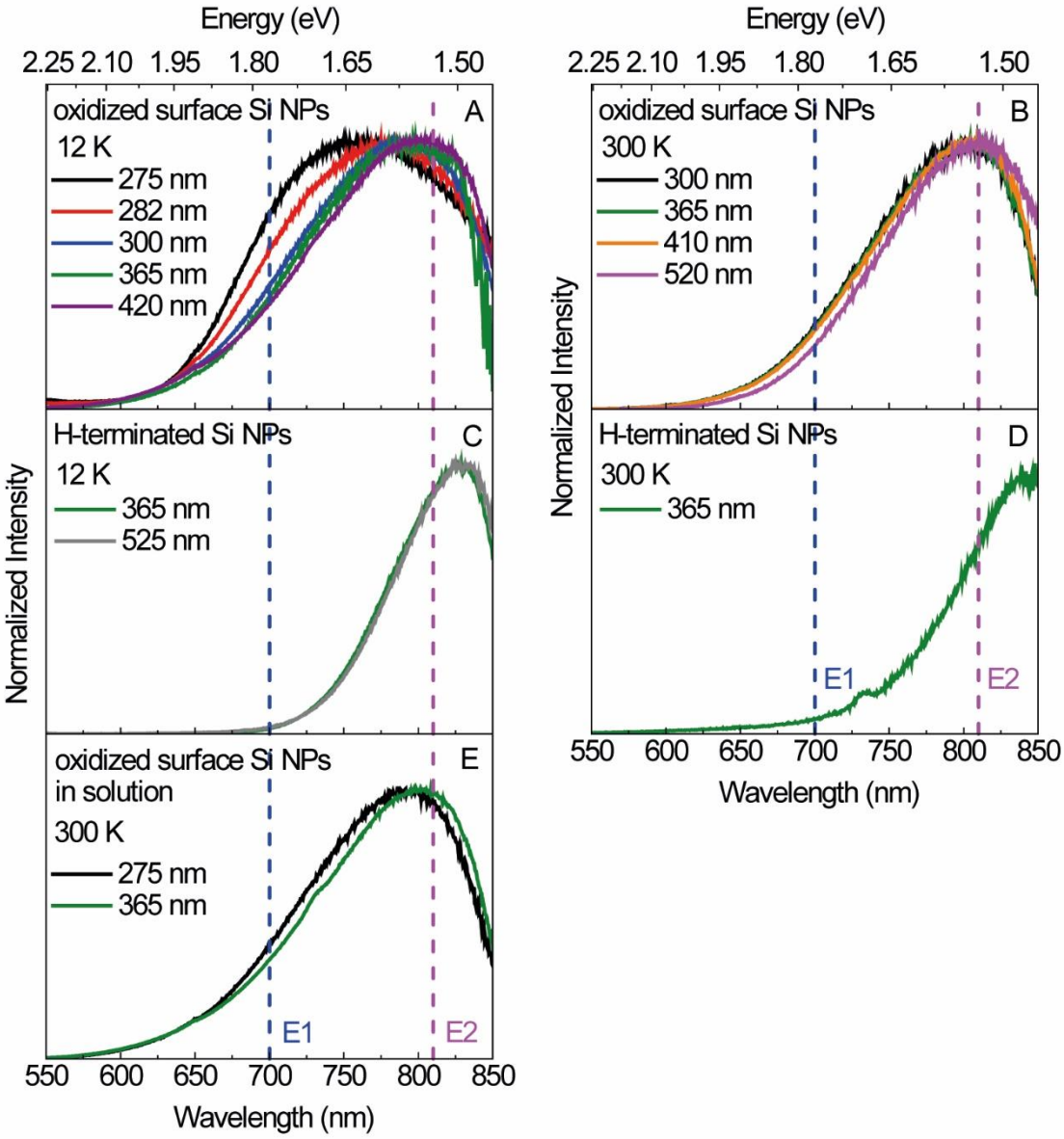

Figure 3.3 Emission spectra of the **oxidized surface Si NPs** excited between 275 and 525 nm and measured at (A) 12 K and (B) 300 K and of the **H-terminated Si NPs** recorded at (C) 12 K and (D) 300 K, as well as of the (E) **oxidized surface Si NPs** in solution measured at 300 K.

The room temperature excitation spectra were monitored in the low- and high-wavelength side of the emission spectrum (700 and 800 nm, respectively) revealing a similar broad band spanning the 260-590 nm spectral region (Figure 3.4B). The low

temperature emission spectra excited within 300-420 nm resemble those acquired at room temperature, whereas for lower excitation wavelengths (250-290 nm) the emission spectra become broader, revealing the raising of the emission on the lower wavelength side of the spectra. At 12 K, the excitation spectra monitored at 700 and at 800 nm (Figure 3.4A) are similar to those acquired at room temperature. Nevertheless, in the case of the spectrum monitored at 700 nm an additional excitation path around 270 nm (4.60 eV) is revealed (Figure 3.4A).

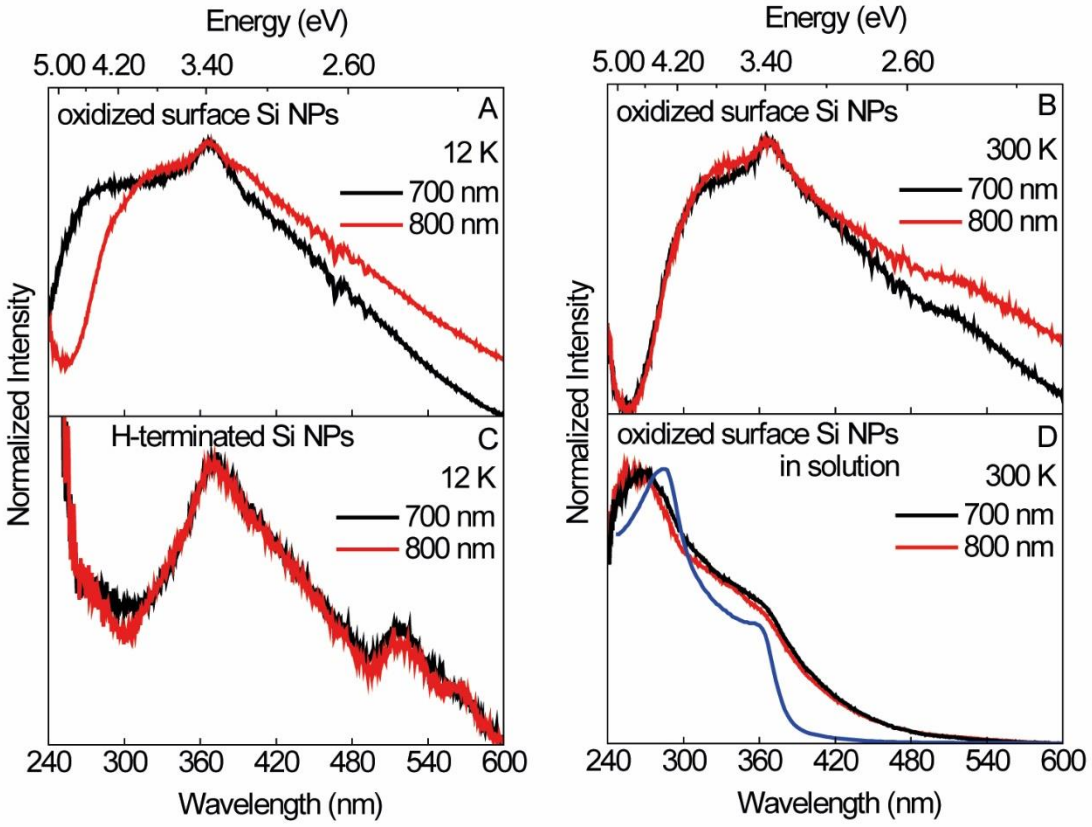

Figure 3.4 Excitation spectra of **oxidized surface Si NPs** at (A) 12 K and (B) 300 K and of the (C) **H-terminated Si NPs** at 12 K, as well as of the (D) **oxidized surface Si NPs** suspended in ethanol recorded at 300 K. The monitoring wavelengths were 700 nm and 800 nm. The blue curve in (D) represents the absorption spectrum of the crystalline bulk Si measured at 10 K.[34]

The emission features of the **oxidized surface Si NPs** were quantified through the measurement of the η as a function of the excitation wavelength (Figure 3.5). The maximum η values (0.095-0.115±0.011) are attained at excitation wavelengths within 270-350 nm. At higher excitation wavelengths (365-420 nm), η decreases from 0.095±0.010 to 0.070±0.007. Despite several reports on the η of oxidized surface Si

NPs in solution, involving distinct solvents,[33, 37, 58, 64, 79] only few reports mention the emission quantum yield for oxidized surface Si NPs deposited as films (Table 1.1, section 1.1).[23, 39, 40, 78] In particular, a similar quantum yield value of 0.09 excited at 266 nm was previously measured for oxidized surface Si NPs also grown by gas-phase[78] and a smaller value of 0.05 excited at 350 nm was reported for oxidized surface Si NPs prepared by pyrolyze of Si_2H_6.[23] Other studies report quantum yield values in the range 0.01-0.30 for films of oxidized surface Si NPs synthesized from laser pyrolysis of silane, depending on the average diameter (2.5-8 nm) and size distribution.[39, 40] In these studies, values above 0.18 were obtained only for molecular beam size-selected Si NPs with average diameters in the range 3-4 nm.[39] For as-grown Si NPs without size selection and with average diameter similar to that of the Si NPs studied here (3.4 nm) these investigations report quantum yield values (0.01-0.10)[40] analogous to those obtained for **oxidized surface Si NPs** also in film.

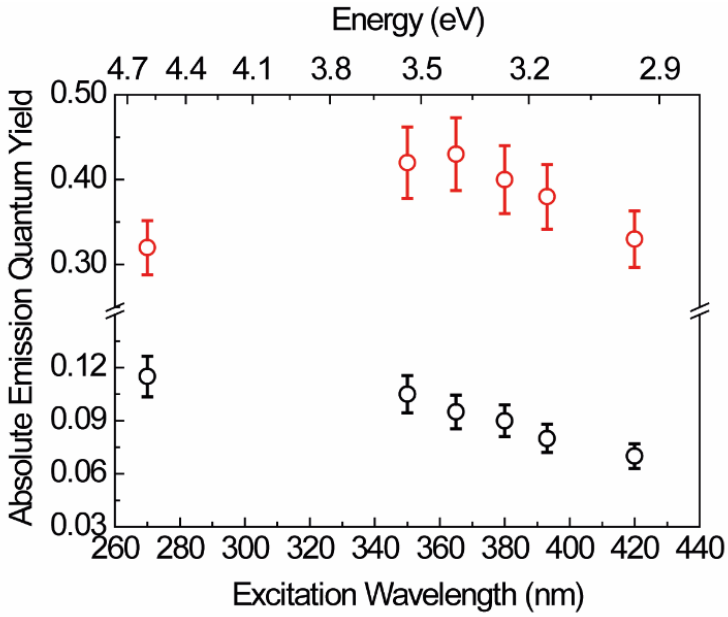

Figure 3.5 Absolute emission quantum yield values obtained as a function of the excitation wavelength for **oxidized surface Si NPs** in film (black circles) and suspended in ethanol (red circles).

Time-resolved emission spectra of the **oxidized surface Si NPs** were acquired at distinct SD values. Both at room temperature and at 12 K (Figures 3.6A and 3.6B, respectively), the emission spectra deviate towards the red and become narrower as SD increases from 0.02 to 0.30 ms, indicating that the time-scale behind the emission at lower wavelengths (700 nm) is faster than that at higher wavelengths (800 nm).

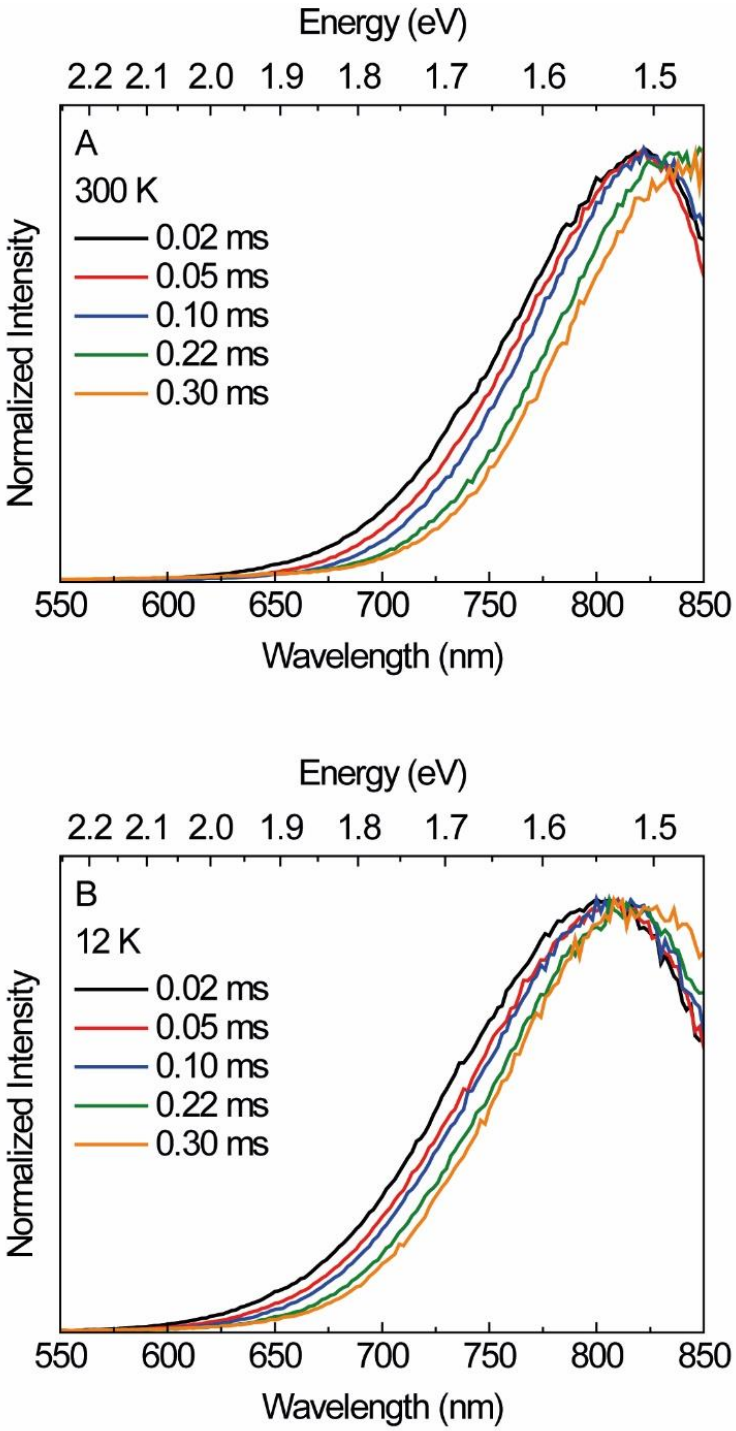

Figure 3.6 Time-resolved emission spectra (excited at 365 nm) of **oxidized surface Si NPs** acquired at 300 K and 12 K for SD between 0.02 ms and 0.30 ms. The integration window was 20 ms.

The emission decay curves of the lower and higher wavelength side of the emission band were selectively monitored at 690 nm and 815 nm, respectively. For both monitoring wavelengths, the emission decay curves display a non-exponential

behavior (Figure 3.7). The non-exponential behavior is observed for both 12 and 300 K.

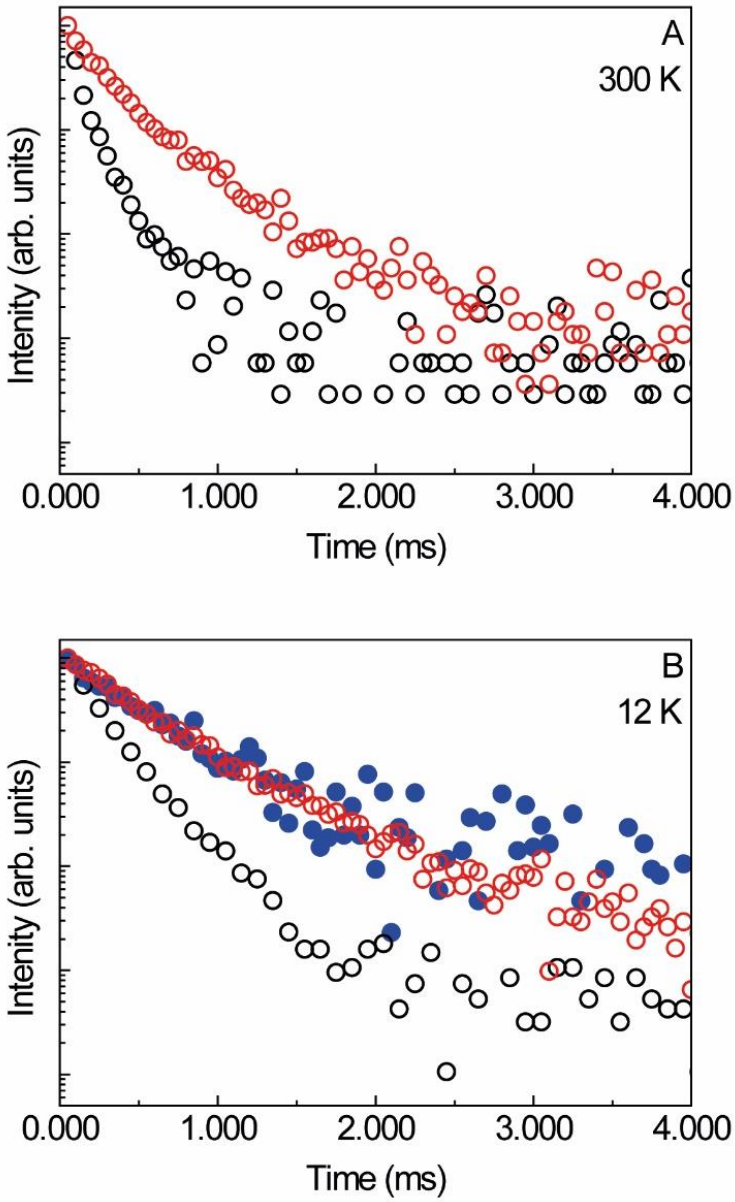

Figure 3.7 Emission decay curves of **oxidized surface Si NPs** acquired at 300 K and 12 K and monitored at 690 nm (black circles) and at 815 nm (red circles). The emission decay curve obtained for the **H-terminated Si NPs** at 12 K and monitored at 800 nm is also shown (blue circles).

The obtained experimental lifetimes (τ) for the emission at 690 nm and at 815 nm (denoted τ_1 and τ_2, respectively), which correspond to the time at which the experimental emission intensity is reduced to $1/e$, are indicated in Table 3.1. For τ_1 and τ_2, an increase of temperature from 12 to 300 K induces a decrease in lifetime. Attending to the fact that the experimental transition probability may be expressed as

$$\tau^{-1} = {\tau_{nr}}^{-1} + {\tau_r}^{-1} \quad (3.1)$$

where τ_{nr} and τ_r, represent the nonradiative and radiative lifetimes, respectively, and that at 12 K $\tau^{-1} \approx {\tau_r}^{-1}$, the decrease in τ as the temperature increases suggests the presence of competing thermally activated nonradiative mechanisms.[166]

Table 3.1 Experimental lifetime values obtained for the E1 and E2 emission components (τ_1 and τ_2, respectively) measured at 12 and 300 K for the **oxidized surface Si NPs** and **H-terminated Si NPs**.

	τ_1 (ms)		τ_2 (ms)	
Temperature (K)	300	12	300	12
oxidized surface Si NPs	0.069±0.001	0.189±0.001	0.235±0.003	0.424±0.003
H-terminated Si NPs	–		<0.01	0.457±0.005

To gain further insight about the recombination paths, the 12 K time-resolved emission spectra were analyzed according to the following methodology. Figure 3.8A shows the emission spectrum of the **oxidized surface Si NPs** acquired at SD=0.55 ms. This spectrum is well described by a single-Gaussian band with energy peak position equal to 1.53±0.02 eV (810 nm) and fwhm equal to 0.23±0.02 eV, indicating that at this SD the emission should be due to a single radiative recombination mechanism. It should be noted that the decay time τ_1 (0.189 ms) measured on the lower wavelength side (690 nm) of the emission band is considerably smaller than τ_2 (0.424 ms), measured on the higher wavelength side (815 nm) of the band (Table 3.1 and Figure 3.7). Therefore, it is not surprising that at SD=0.55 ms the emission observed in the lower wavelength side (≈700 nm) of the steady-state spectrum is not present. For lower SD values the recorded spectra change. The band becomes asymmetric and broader (Figure 3.8) and can no longer be described with a single-Gaussian function. The spectra at lower SD values are well described with a sum of two Gaussian functions (Figure 3.8), in which one of the functions is similar to that used to adjust the spectrum acquired at SD=0.55 ms and the other is centered at a peak position of 1.66±0.01 eV.

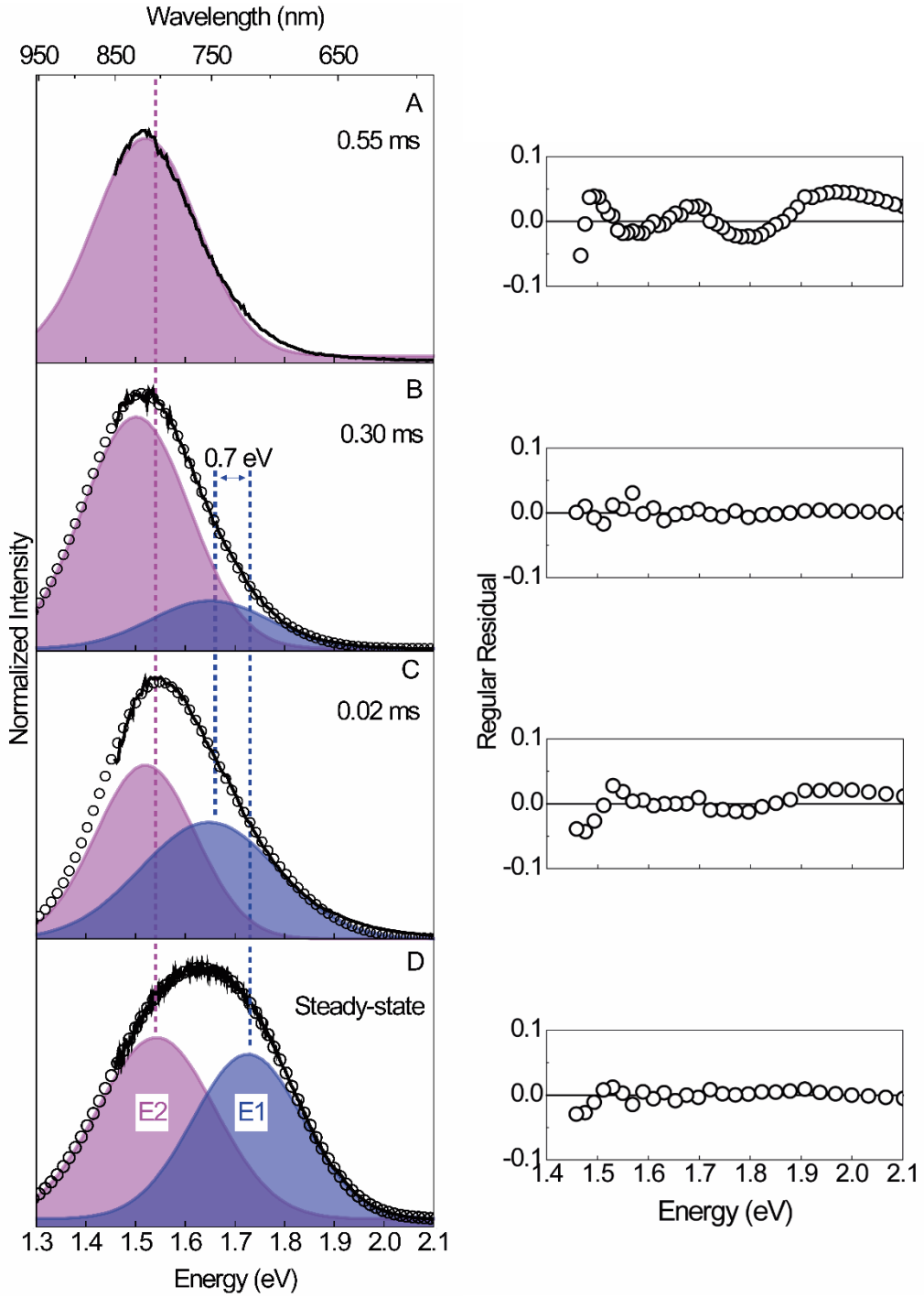

Figure 3.8 Low-temperature (12 K) time-resolved emission spectra of the **oxidized surface Si NPs** excited at 365 nm and obtained at SD values of (A) 0.55, (B) 0.30 and (C) 0.02 ms, together with (D) steady-state emission spectrum excited at 275 nm. Two-Gaussian envelope fit (open circles) and the corresponding E1 and E2 components (shaded area). The respective regular residual plots are also shown (right side).

It should be noted that all emission spectra recorded for SD≤0.30 ms are well modelled with these two Gaussian functions, each one with an energy that is rather independent of SD (Figure 3.8 and Table 3.2).

The steady-state emission spectrum is also modelled with two emission components centered at energies similar to those of the spectra acquired at different SD (Figure 3.8D). These experimental observations provide compelling evidence for the present of two distinct emission components centered at ≈700 nm and ≈800 nm in the spectra of the oxidized surface Si NPs. These components are hereafter denoted E1 and E2, respectively.

The existence of two distinct components can also account for the dependence of the emission and excitation spectra on the excitation and monitoring wavelength (Figures 3.3 and 3.4, respectively), and for the variation of η as the excitation energy is varied (Figure 3.5). Moreover, as mentioned above, non-exponential decay curves were observed, both at the low and high wavelength sides of the emission band (Figure 3.7). The observation of non-exponential decays for the E1 and E2 emissions could be associated with size and shape dispersion of the Si NP samples[166, 167] or with fluctuations in the local environment of the emission states.[168] Moreover, non-exponential decays can also be due to charge migration between interacting NPs,[166, 167, 169] which can be mediated by escape states in the surface oxide created due to disorder.[169]

Table 3.2 Energy peak position and fwhm for E1 and E2 emission components resulting from the fit to the emission spectra measured at 12K and excited at 365 nm in steady state regime and in the time-resolved mode for a SD between 0.02 and 0.50 ms.

		E1		E2	
		Energy peak position (±0.02 eV)	fwhm (±0.02 eV)	Energy peak position (±0.02 eV)	fwhm (±0.02 eV)
Steady-state		1.73	0.23	1.54	0.19
SD (ms)	0.02	1.66	0.27	1.53	0.20
	0.10	1.67	0.25	1.52	0.20
	0.22	1.67	0.21	1.51	0.20
	0.30	1.67	0.21	1.51	0.23
	0.55	–		1.53	0.23

The identification of two emission components is corroborated from photoluminescence measurements of the same Si NPs after replacement of the surface oxide with hydrogen-termination through HF-etching. Figure 3.3C shows the 12 K emission spectra of the **H-terminated Si NPs**. The emission spectra display a Gaussian

shaped band peaking at 830 nm, independent of the selected excitation wavelength and temperature (Figure 3.3C). Apart from a small red-shift (≈50 meV), this emission spectrum is similar to the E2 component of the **oxidized surface Si NPs**. It should be noted that no signature of the E1 component could be detected in the spectra of the **H-terminated Si NPs**. Unlike observed for the **oxidized surface Si NPs**, the excitation spectra of the **H-terminated Si NPs** monitored at 12 K along the broad band emission (Figure 3.3C) are independent of the monitoring wavelength (Figure 3.4C), indicating a single component for the emission band. It may be concluded that E2 is related to the NPs core, whereas E1 is associated with emission involving states associated with the oxide shell.

Further confirmation of that the band observed for the **H-terminated Si NPs** corresponds to the E2 emission component observed for the **oxidized surface Si NPs** is provided by the 12 K emission decay curve monitored at 800 nm for the **H-terminated Si NPs** (Figure 3.7B). This emission decay curve resembles that monitored for the E2 component observed for the **oxidized surface Si NPs** measured under the same experimental conditions (Figure 3.7B), revealing an experimental lifetime value (0.457±0.005 ms, Table 3.1) similar to that obtained for the **oxidized surface Si NPs** (0.424±0.003 ms, Table 3.1), unequivocally attributing the E2 emission in the **oxidized surface Si NPs** to recombination in the Si NPs core.

At 300 K, the E2 lifetime measured for **H-terminated Si NPs** decreases to values below the detection limit of our experimental apparatus (0.01 ms). Also, η values of the **H-terminated Si NPs** substantially decrease with respect to the values measured for the **oxidized surface Si NPs**, being below the experimental detection limit of about 0.01. Both observations indicate the presence of extra non-radioactive channels, with respect to the E2 emission, in the case of **H-terminated Si NPs** when compared to **oxidized surface Si NPs**.

The E2 emission peak position and fwhm obtained from the spectra analysis (fits) are almost independent of SD and are equal to the values obtained for steady-state mode (Figure 3.8 and Table 3.2). The fact that the energy peak position of E2 is independent of the SD values is an experimental evidence of an excitonic recombination mechanism in semiconductors,[56, 166, 170-172] which in Si NPs are associated with the NP core states. For the **H-terminated Si NPs**, the 300 K emission

spectrum shifts to the red (≈30 meV) compared to that acquired at 12 K. This is the expected dependence of the band gap of Si with decreasing temperature,[34] as already observed in Si nanocrystals embedded in SiO_2.[167] This supports the conclusion that the E2 emission is due to excitonic recombination. Comparing the values energy peak position of E1 obtained from the spectra measured at different SD with the value obtained from modelling the steady-state spectrum, it is observed that the primer values are red-shifted by 0.7 eV (Figure 3.8 and Table 3.2). This suggests that the emission E1 is governed by a donor−acceptor recombination mechanism, because distant pairs emit at longer wavelengths with lower transition probability and, thus, longer lifetime values.[170, 173-175] The donor−acceptor states are most probably located at the interface between the NP core and the oxide shell or inside the surface oxide shell, in either case, they are related to the presence of the oxide shell.

The photoluminescence properties of the **oxidized surface Si NPs** suspended in ethanol were also studied. The characteristics of the emission (peak energy and fwhm) of the **oxidized surface Si NPs** in ethanol (Figure 3.3E) are similar to those described above for the same **oxidized surface Si NPs** in film (Figure 3.3B). However, major changes were observed in the excitation spectra (Figure 3.4D). The excitation spectra monitored at E1 and E2 are in this case identical, revealing an increase in the relative intensity of the low-wavelength region with the appearance of a component around 270 nm that was not present in the room temperature excitation spectra of the **oxidized surface Si NPs** in film (Figure 3.4B).

The η of the Si NPs in suspension has a maximum value of 0.43±0.04 for excitation wavelengths between 350 and 393 nm. At 270 nm and 420 nm the quantum yield decreases to 0.33±0.03 (Figure 3.5). Independently of the excitation wavelength, there is a substantial increase in the quantum yield values of the **oxidized surface Si NPs** in suspension with respect to those in film (Figure 3.5). Table 1.1, in section 1.1, gathers the quantum yield values reported for oxidized surface Si NPs in suspensions.[33, 37, 58, 64, 79, 80] The NPs size is also indicated as it influences the emission energy. In what concerns oxidized surface Si NPs, the values observed for **oxidized surface Si NPs** in suspension are among the highest[80] reported so far. However, a note of caution is in order: the comparison between quantum yield values measured in distinct solvents needs to take into consideration the solvent polarity. It has been

observed for germanium NPs and Si NPs that the emission quantum yield decreases with decrease in the polarity of the solvent.[33]

In order to discuss the possible radiative and nonradiative recombination mechanisms present in the Si NPs as a function of termination shell and the NP proximity, the energetic diagrams depicted in Figure 3.9 were built, in which the band edge energies of the Si NPs and the surface oxide are compared. Based on the experimental emission energy of E2 (1.54 eV) the location of the lowest unoccupied molecular orbital (LUMO) level of the Si NPs is at −3.85 eV with respect to the vacuum level. This corresponds to the electron affinity of bulk Si (−4.0 eV) plus one-third of the confinement energy (0.44 eV),[41] which is the energy difference between the E2 peak position (1.54 eV) and the bulk Si energy gap (1.1 eV). The highest occupied molecular orbital (HOMO) is −5.39 eV, which corresponds to the ionization energy of bulk Si (−5.1 eV) minus two-thirds of the confinement energy.[41] The HOMO of the surface oxide lays between 4.1 and 4.4 eV below the HOMO of the Si NPs,[176-178] and the energy of the LUMO is ≈0.0 eV.[179] The excitation spectra of the **oxidized surface Si NPs** suspended in ethanol (Figure 3.4D) resemble the absorption spectrum of bulk Si,[34] also depicted for comparison in Figure 3.4D. The absorption spectrum of bulk Si has a feature associated with the direct $\Gamma_{25} \rightarrow \Gamma_{15}$ transition, whose energy is 3.4 eV (365 nm), and another one with energy of 4.2 eV (295 nm) ascribed to a second direct $\Gamma_{25} \rightarrow \Gamma_{2'}$ transition or a direct transition at *X*.[33, 34, 58, 81, 82, 180] The observed similarity between the excitation spectra recorded at 300 K for both emission components (E1 and E2) in **oxidized surface Si NPs** suspended in ethanol (Figure 3.4D) and the absorption spectrum of bulk Si indicates that in this case both emissions are fed by electrons and holes photoexcited within electronic states of the NPs core. Since emission E1 involves states associated with the oxide shell, it can be concluded that charge transfer from the core to oxide shell states takes place in the Si NPs. These mechanisms are illustrated in Figure 3.9A, with the core-shell charge transfer indicated as path (i).

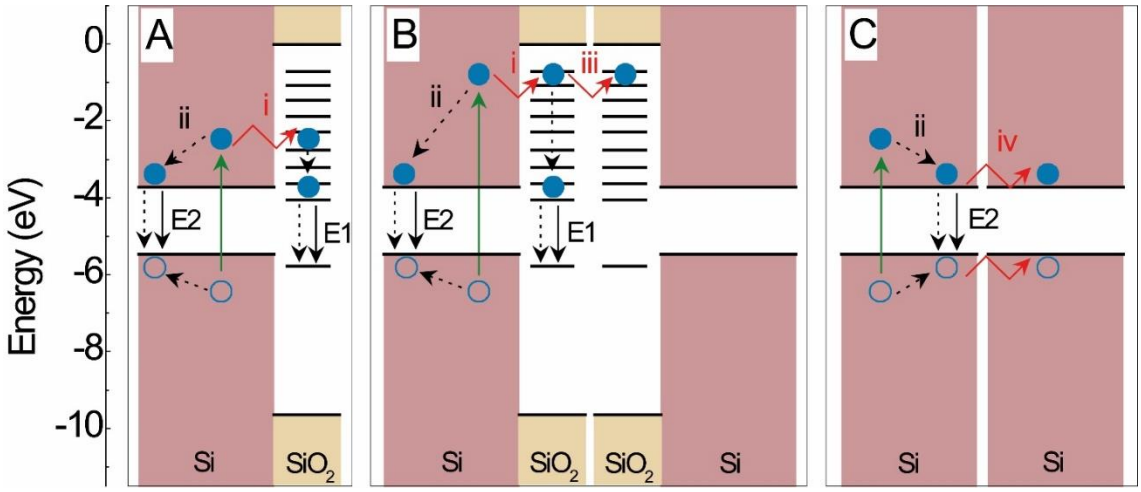

Figure 3.9 Schemes illustrating the energy level diagram for (A and B) **oxidized surface Si NPs** and (C) **H-terminated Si NPs**. The vertical arrows represent radiative (solid line) and selected nonradiative (dashed lines) transitions. The curved arrows stand for inter-NPs charge transfer.

When the **oxidized surface Si NPs** are in film the excitation spectra, measured at room temperature (Figure 3.4B), deviate from those recorded for oxidized surface Si NPs in ethanol. The deviation is evidenced by a change of the relative intensity between the lower (≈295 nm) and higher (≈365 nm) wavelength regions. These deviations indicate that, in the case of having the Si NPs in film, electrons and holes that are excited at the lower wavelength region are non-radiatively lost, since they do not lead to photoemission, which does not happen in the case of Si NPs in ethanol. It should be noted that the Si NPs are the same in the two types of samples. The competing nonradiative recombination mechanism that takes place in the Si NPs in film is absent in the case of Si NPs in solution. Despite the fact that oxidized surface Si NPs do not form fully dispersed solutions in polar solvents like ethanol, the NPs aggregate in clusters, which are in any case smaller than in the film. It is reasonable to assume that, in the case of Si NPs dispersed in ethanol, excitons have a more limited number of NPs to which they can diffuse. This in turn limits the probability of nonradiative recombination in this case. Thus, the most likely nonradiative recombination mechanism involved in the case of Si NPs in film, justifying the above-mentioned differences observed in the excitation spectra, should be inter-NP charge transfer. This path is schematically depicted as (iii) in Figure 3.9B. Nonradiative recombination associated with inter-NP charge transfer taking place in Si NPs in film also accounts for the observed lower quantum yield values measured for **oxidized**

surface Si NPs in film when compared to values measured for **oxidized surface Si NPs** in ethanol (Figure 3.5). Moreover, when the 12 K excitation spectra is monitored at E1 and E2, it is observed that the E1 emission (Figure 3.4A) reveals the appearance of a contribution at a wavelength region ≈270 nm. This means that at 12 K, the electrons and holes that are excited at ≈270 nm lead selectively to the E1 emission, indicating that some of the inter-NP charge transfer paths are thermally activated.

Different Si NP shells also influence the inter-NP charge transfer. The room temperature excitation spectra of the **H-terminated Si NPs** (Figure 3.4C) are different from those recorded for the **oxidized surface Si NPs** (Figure 3.4B), both in the form of NPs film. The main difference is a decrease in the relative intensity of the low-wavelength region around ≈295 nm for the case of **H-terminated Si NPs**. The inter-NP charge transfer in **H-terminated Si NPs** should be different from that of **oxidized surface Si NPs**, which results in different excitation spectra. Figure 3.9C illustrates the situation for the case of **H-terminated Si NPs**. Here, electrons and holes are photogenerated in the NPs core with energies above and below the LUMO and HOMO, respectively. After thermalization, these may recombine leading to the E2 emission or may be transferred to neighboring Si NPs, which is a potential nonradiative recombination path as in the case of **oxidized surface Si NPs**. However, transfer of photogenerated charge carriers between core states of neighboring Si NPs is more efficient in the case of **H-terminated Si NPs** than in the case of **oxidized surface Si NPs**, since the surface oxide represents a higher barrier for direct inter-NP charge transfer.[121] This conclusion is in good agreement with the significantly lower η and lower room-temperature lifetime value of the E1 emission in the **H-terminated Si NPs**, when compared to what we found for **oxidized surface Si NPs**. In **H-terminated Si NPs**, direct inter-NP charge transfer between core states, represented by (iv) in Figure 3.9C, may take place.[121] Although, it can not rule out that the direct charge transfer may also take place in the case of **oxidized surface Si NPs**, a recent study has shown that this mechanism is not dominant and charge transfer between NP core states should be mediated by oxide-related localized states,[121] as represented in Figure 3.9C.

Organic-functionalized silicon nanoparticles

Figure 3.10A shows the emission spectra of the Si NPs measured at room temperature. The spectrum of **Si NPs-C12** is formed of a broad band (fwhm ≈0.23 eV) in the red spectral region, peaking at 758 nm (1.64 eV). Apart from a minor red-shift (≈0.03 eV), this emission spectrum resembles that measured for **Si NPs-H**. Decreasing the temperature from 300 K to 12 K (Figure 3.10B), the emission spectrum reveals a blue-shift (≈0.1 eV). This shift is considerably larger than the value that is expected for bulk Si (≈0.045 eV), which results from the temperature-induced shrinkage of the band gap in this temperature range.[166] The emission spectra of **Si NPs-C12-O** (*i.e.* **Si NPs-C12** exposed to air) is broader and blue-shifted with respect to **Si NPs-C12**. The emission spectra of **Si NPs-C12** and **Si NPs-H** measured with higher excitation wavelengths (525 nm and 460, respectively) are identical to the spectra measured under 365 nm excitation. For **Si NPs-C12-O**, the increase in the excitation wavelength (from 365 to 525 nm) results in a red-shift of the broad band of the emission (≈0.05 eV).

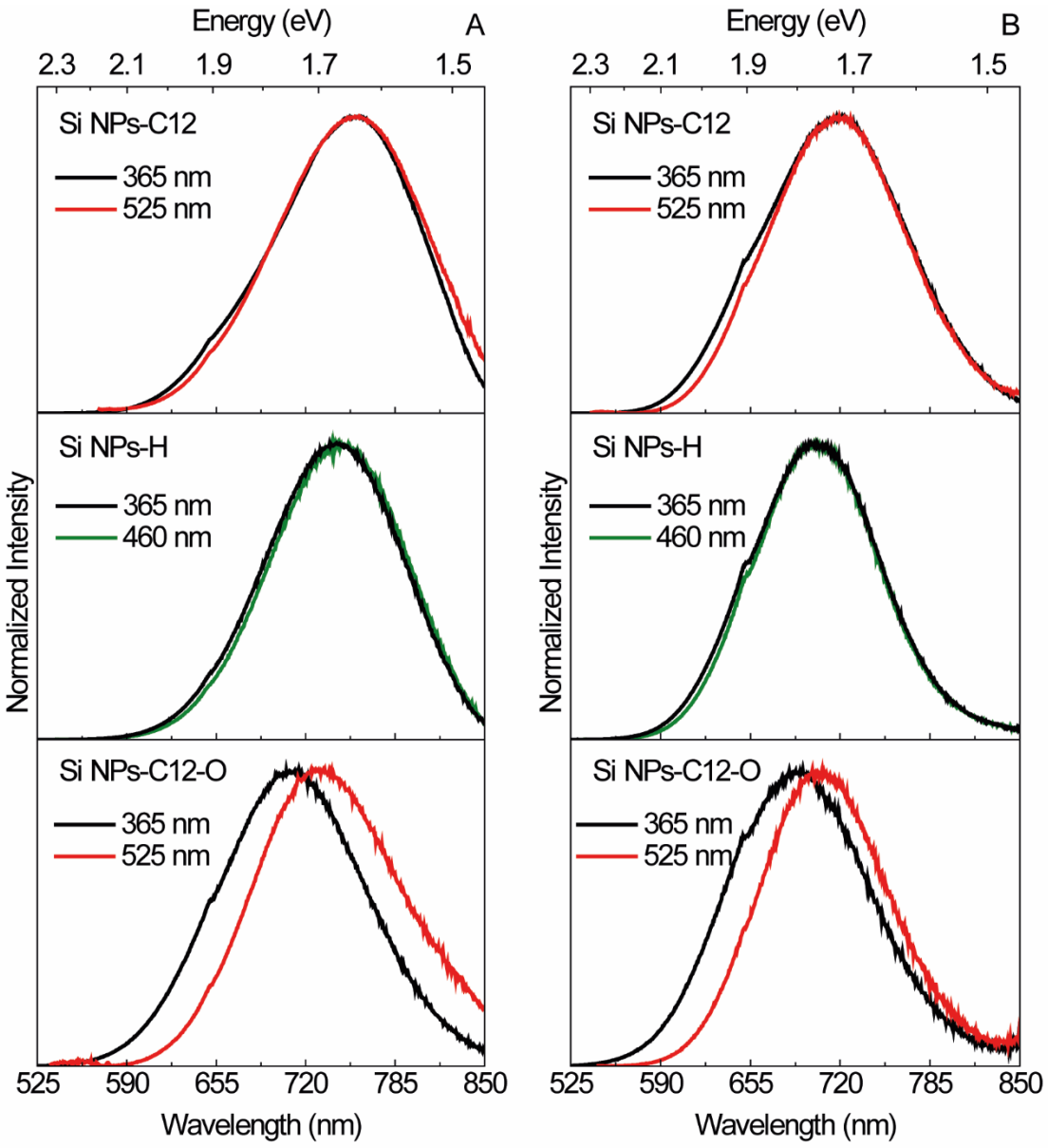

Figure 3.10 Emission spectra of **Si NPs-C12**, **Si NPs-H**, and **Si NPs-C12-O** measured at (A) 300 K and (B) 12 K, excited at the indicated wavelengths.

The room temperature excitation spectra of the **Si NPs-H**, **Si NPs-C12**, and **Si NPs-C12-O** (Figure 3.11) were monitored along the emission spectra at 12 K and at 300 K, in which a broad band spanning from 250 nm to 600 nm, with three excitation components at ≈270 nm, 365 nm, and 525 nm are discerned. The excitation spectra of the **Si NPs-H** and **Si NPs-C12** are independent of the monitoring wavelength, as shown in Figure 3.11 for selected monitoring wavelengths, due to the presence of a single emission component related with the Si-core of the NPs. In the case of the **Si NPs-C12-O**, the excitation spectra depend on the monitoring wavelength, in good agreement with the appearance of a surface/interface-related emission component discussed

above. Apart from changes in the relative intensity, the excitation spectra are independent of the selected temperature value (Figure 3.11).

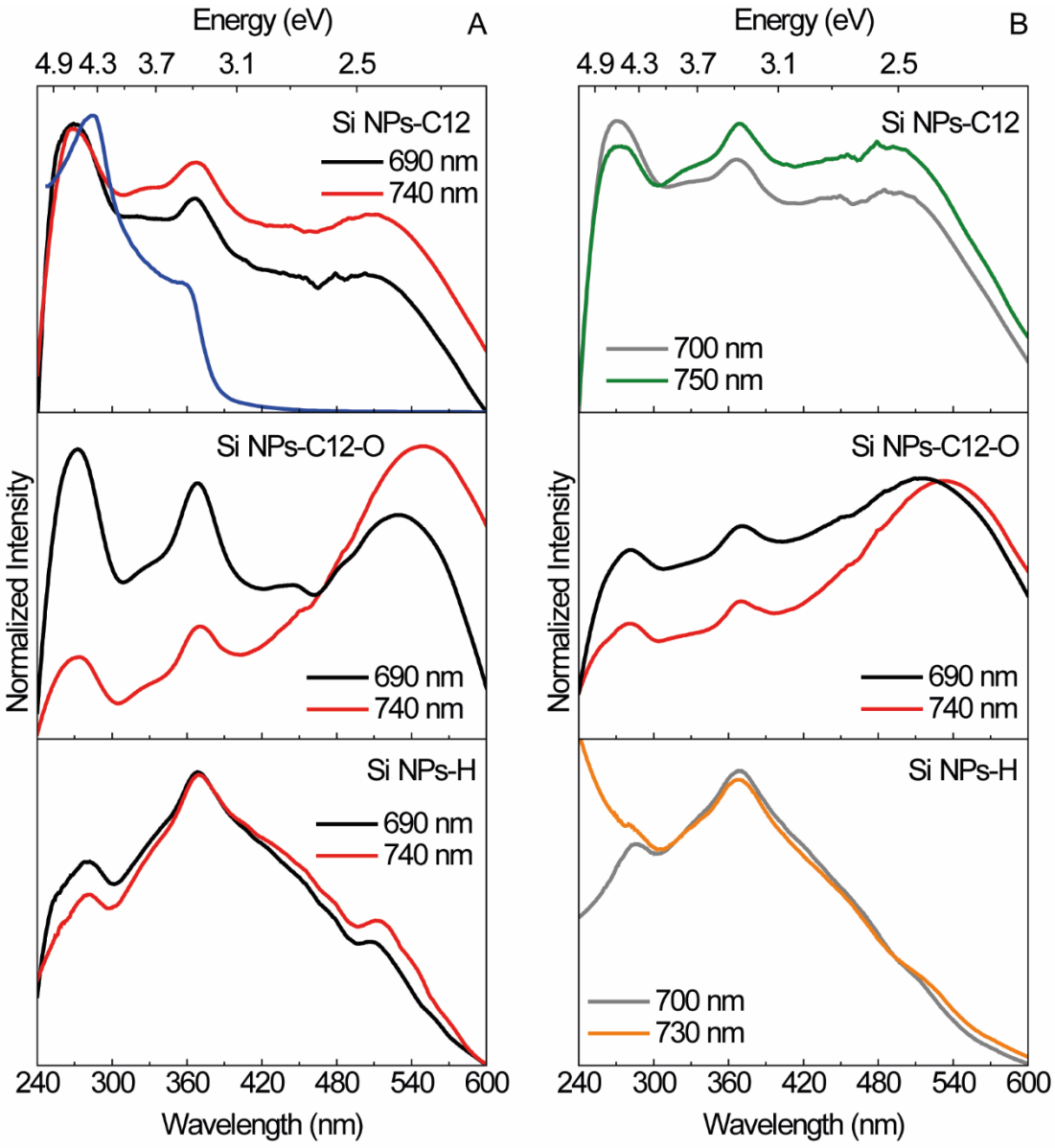

Figure 3.11 Excitation spectra of **Si NPs-C12**, **Si NPs-C12-O**, and **Si NPs-H** measured at (A) 300 K and (B) 12 K, monitored at the indicated wavelengths. The intensity increase observed below 300 nm for **Si NPs-H** is due to correction effects. The dashed curve represents the absorption spectrum (10 K) reported for crystalline bulk Si.[34]

The emission properties of **Si NPs-C12** were also quantified through the measurement of η as a function of the excitation wavelength. In particular, η was measured under excitation around the three components observed in the excitation spectra (270 nm, 325 nm and 525 nm), yielding analogous values within the experimental error (0.18±0.02, 0.23±0.02, and 0.20±0.02, respectively). After surface

oxidation (**Si NPs-C12-O**), η remains constant within the experimental error being 0.18±0.02, 0.21±0.02, and 0.17±0.02 excited at 270 nm, 325 nm, and 525 nm, respectively. This result is different from that reported for 1-dodecene-functionalized Si NPs in solution (with higher average diameter, namely 3.9 nm prior to surface oxidation and 3.7 nm after oxidation), which show a decrease in η from 0.62 to 0.40 upon surface oxidation.[71] The range of η values observed for **Si NPs-C12** and **Si NPs-C12-O** is substantially higher than the values measured for **Si NPs-H**, which exhibit maximum η values of 0.03±0.01, excited in the low-wavelength region (≈270 nm).

In order to study the role of the surface termination in the time-scale behind the emission features of the Si NPs and to distinguish different components in the emission spectra, time-resolved emission spectra measurements were performed. Figure 3.12A compares the low-temperature (12 K) time-resolved emission spectra of **Si NPs-C12** recorded at different SD values, revealing a band well described by a single Gaussian function, whose maximum (1.83±0.01 eV) and fwhm are independent of the SD, readily establishing the presence of a single emission component. Apart from a blue-shift of ≈0.1 eV, this band resembles the spectrum acquired in steady-state for the same sample. Moreover, the characteristics of the time-resolved emission spectra observed for **Si NPs-C12** are rather similar to those observed in the time-resolved spectra of **Si NPs-H** (Figure 3.12B). These observations show that the origin of the emission band observed for **Si NPs-C12** is the same as that of the band recorded for **Si NPs-H**.

For **H-terminated Si NPs**, it was shown above that the emission is due to recombination of photogenerated electrons and holes located in the crystalline core of the Si NPs (E2 emission). The fact that the time-resolved emission spectra are independent of the SD values is an experimental evidence of a single emission mechanism, typically associated to excitonic recombination in semiconductors.[170, 171] At room temperature the time-resolved emission spectra deviates to the red as SD increases, as shown in Figures 3.12C and 3.12D for the **Si NPs-H** and **Si NPs-C12**, respectively.

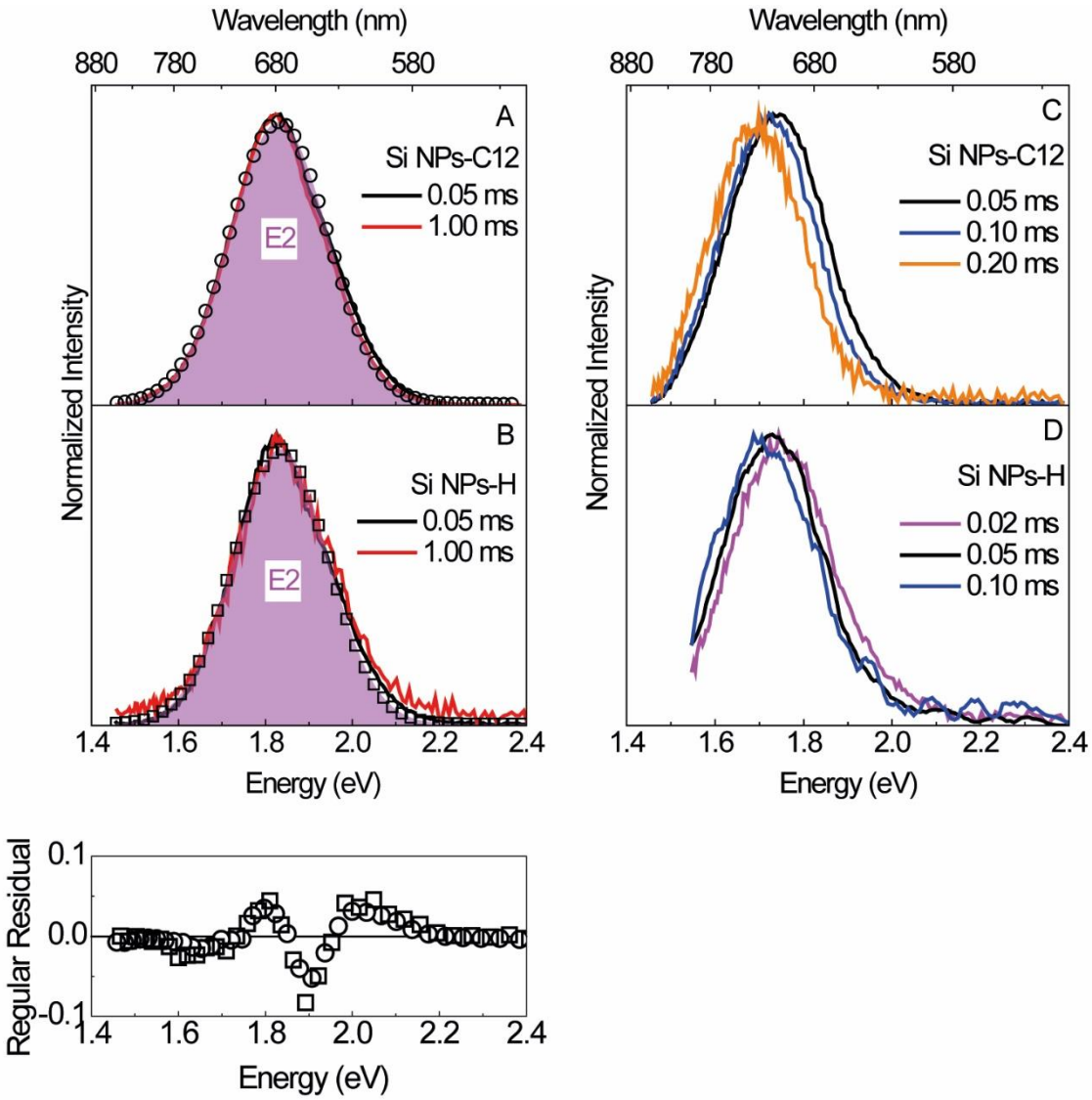

Figure 3.12 Time-resolved emission spectra of **Si NPs-C12** and **Si NPs-H** measured at (A and B) 12 K and at (C and D) 300 K, excited at 365 nm for the indicated SD. Gaussian envelope fit (open symbols) and the corresponding E2 components (shaded area). The respective regular residual plots [coefficient of determination (r^2)>0.99] are also shown (bottom).

The time-resolved emission spectra (peak and fwhm) of **Si NPs-C12-O** depend on SD. For SD=0.05 ms, two emission components are clearly discerned, namely E2 and another one (E1 emission) at higher energies (Figure 3.13). As the SD value increases from 0.05 ms to 0.50 ms, the relative intensity of E1 decreases, so that for SD>0.50 ms only the long-lived E2 emission is observed. The appearance of E1 after surface oxidation has already been observed for **oxidized surface Si NPs**, being ascribed to radiative recombination via electronic states associated with the surface oxide.

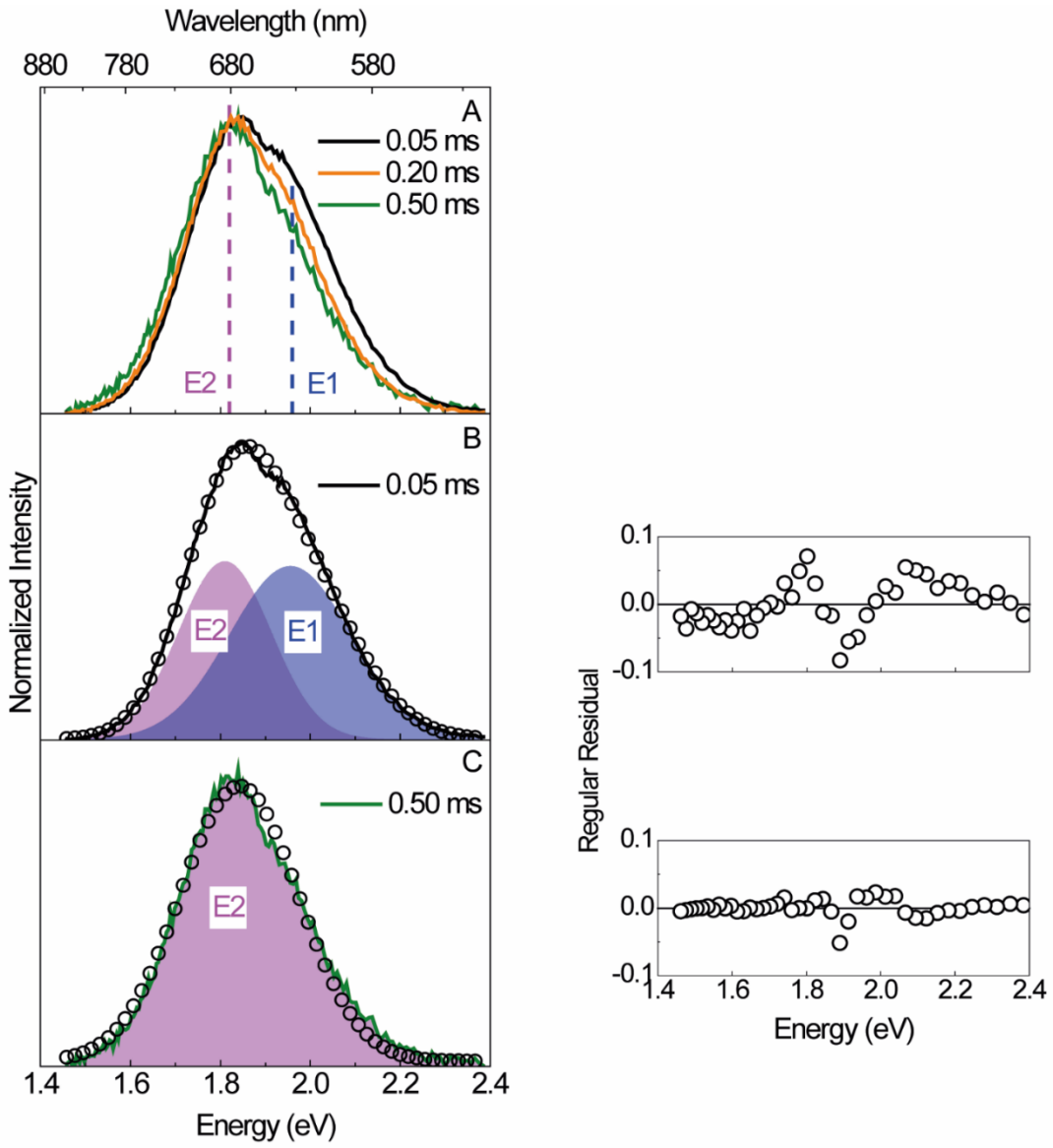

Figure 3.13 Time-resolved emission spectra of **Si NPs-C12-O** measured at 12 K, excited at 365 nm for SD values between 0.05 and 0.50 ms. Gaussian envelope fit (open circles) and the corresponding E1 and E2 components (shaded areas). The respective regular residual plots (r^2>0.99) are shown on the right.

The emission decay curves for **Si NPs-C12** and **Si NPs-H** (Figure 3.14) were monitored at 12 K/300 K around the maximum intensity peak position of the time-resolved emission spectra, namely at 680/710 nm and 679/690 nm, respectively (Figure 3.12). For **Si NPs-C12-O**, the emission decay curves (Figure 3.14) of the E1 and E2 emission components were selectively monitored at 300/12 K around 600/617 nm and 690/710 nm, respectively. These wavelengths deviate from the emission peak position to decrease the spectral overlap between E1 and E2 components, enabling a selective detection of E1 and E2 emission decay curves.

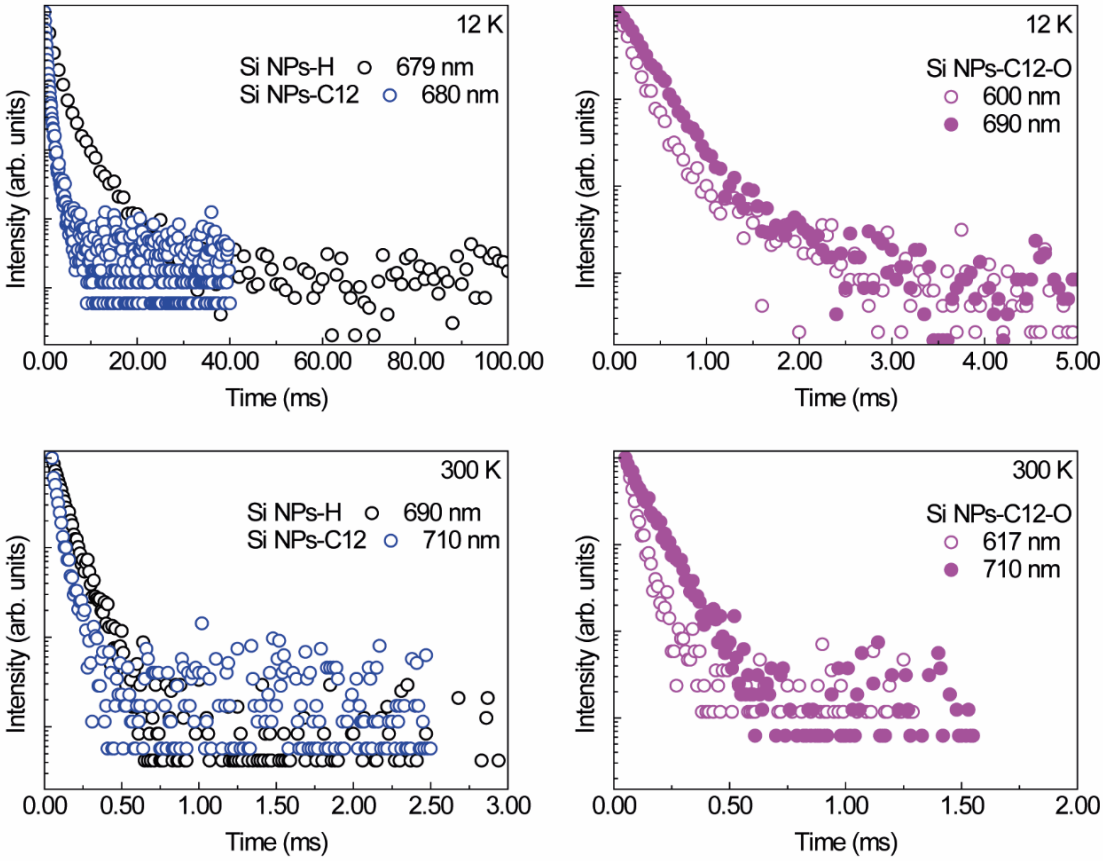

Figure 3.14 Emission decay curves of **Si NPs-C12**, **Si NPs-H** and **Si NPs-C12-O** measured at 12 and 300 K. The monitoring wavelengths are indicated in the figure.

The emission decay curves of **Si NP-H** and **Si NPs-C12** display a non-single exponential behavior, suggesting a distribution in the Si NPs diameter.[166] Thus, lifetime values (τ), corresponding to the time at which the experimental emission intensity is reduced to $1/e$, were estimated for all the samples (the τ of E1 emission are 0.20±0.05 ms and 0.085±0.005 ms, at 12 and 300 K, respectively, and the τ of E2 emission are shown in Table 3.3), evidencing that τ depends both on the surface termination and temperature, as discussed below.

Table 3.3 Experimental lifetime values (ms) for the E2 emission of the Si NPs.

Temperature (K)	**Si NPs-C12**	**Si NPs-H**	**Si NPs-C12-O**
12	1.54±0.05	0.41±0.05	0.31±0.05
300	0.121±0.005	0.083±0.005	0.124±0.005

The observed dependence of the light emission properties of the Si NPs on the surface termination may be rationalized in terms of inter-NP exciton migration, which

is expected to depend on the distance between NPs and on the inter-NP medium. A certain degree of electronic interconnection is expected in NP ensembles because the NPs are physically interconnected.[166, 181-183] To help in the discussion, Figure 3.15 illustrates the energy level diagrams of the interface between two Si NPs in the cases of (A) **Si NPs-H**, (B) **Si NPs-C12**, and (C) **Si NPs-C12-O**.

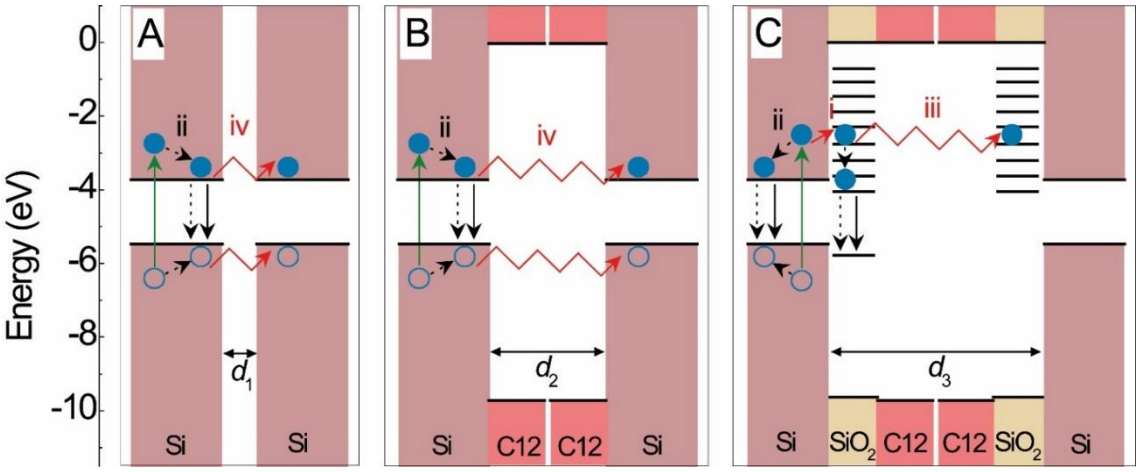

Figure 3.15 Schemes illustrating the energy level diagram at the interface between two Si NPs for the cases of (A) **Si NPs-H**, (B) **Si NPs-C12**, and (C) **Si NPs-C12-O**. The vertical arrows represent absorption (green solid) and radiative (black solid) and nonradiative (black dashed) transitions.

Based on the experimental emission energy of E2 (≈1.8 eV) extracted from the low-temperature emission spectra, the LUMO level of the Si NPs is located at −3.75 eV with respect to the vacuum level. This corresponds to the electron affinity of bulk Si (−4.0 eV) plus one-third of the confinement energy (0.72 eV),[41] which is the energy difference between the E2 peak position (1.82 eV) and the bulk Si energy gap (1.1 eV). The HOMO is at −5.58 eV, which corresponds to the ionization energy of bulk Si (−5.1 eV) minus two-thirds of the confinement energy.[41] The HOMO of the organic molecule (1-dodecane) attached to the surface of the Si NPs was considered identical to that of 1-decane (≈9.65 eV).[184] It was assumed that the LUMO is at the vacuum level (0.0 eV) for the surface oxide[179] and the organic molecules. The mean distance between the Si surfaces of **Si NPs-H** (d_1=0.29 nm) is considered as being twice of the Si-H bond length (Figure 3.15A).[185] For **Si NPs-C12**, It was estimated the mean distance between the Si surfaces considering theoretical studies developed for gold NPs capped with organic molecules. In that case, the equilibrium distance between the NPs cores is ≈1.25 times larger than the diameter value of the crystalline core of the NPs,[186, 187]

yielding d_2=0.60 nm, which corresponds to the distance between the NPs centers minus twice the NPs radius (Figure 3.15B). The average distance between Si surfaces for **Si NPs-C12-O** is d_2 plus twice the thickness of the oxide shell (0.4 nm), d_3=1.40 nm (Figure 3.15C).

Evidence for exciton migration can be found by comparing the emission peak position at 12 K and at room temperature, permitting to infer from the role of the surface termination and of the inter-NP distance on the fluorescent mechanism. In particular, the shift in the peak position with the temperature variation from 12 K to room temperature depends on the surface termination. In the case of **Si NPs-C12** and **Si NPs-H**, this shift is considerably larger (≈0.1 eV) than the value of ≈0.045 eV that is expected for bulk Si, which indicates that radiative sites are located at lower energies.[166] This red-shift of the luminescence spectra can be explained by the presence of efficient energy migration from smaller to larger nanocrystals.[188] In particular, after electronic thermalization (path ii in Figure 3.15), this migration (paths iii and iv in Figure 3.15) takes place until the electrons and holes recombine radiatively (vertical arrows with solid lines in Figure 3.15) and favors radiative recombination in NPs with smaller energy band gap, which means larger diameter. The red-shift with the increasing of SD observed in the time-resolve emission spectra of **Si NPs-C12** and **Si NPs-H** measured at 300 K (Figures 3.12C and 3.12D) is another evidence of energy migration, due to the fact that this result means that smaller size Si NPs (higher emission energy) are favored at shorter SD because its lifetime is shorter due to efficient energy migration to larger Si NPs. Therefore, the long-lived emission spectra appear at shorter energies as they arise from the larger size NPs.

The emission decay curves observed for the Si NPs provide insight into the dependence of exciton migration on the termination of the Si NPs. Focusing the attention on the dynamics behind the core-related emission (E2). For Si NP films in which there is some degree of NP interconnection, the E2 exciton lifetime can be described through

$$\tau^{-1} = k_{\mathrm{r}} + k_{\mathrm{nr}} + k_{\mathrm{m}} \qquad (3.2)^{*}$$

* In Equation (3.1) ${\tau_r}^{-1} = k_{\mathrm{r}}$ and ${\tau_{nr}}^{-1} = k_{\mathrm{nr}} + k_{\mathrm{m}}$

where k_{r} is the radiative recombination probability, k_{nr} is the nonradiative recombination probability, and k_{m} is the probability of exciton migration.[166, 189] At 12 K, k_{nr} may be neglected[166] and $\tau^{-1} \approx k_{\mathrm{r}} + k_{\mathrm{m}}$. Knowing that for Si NPs with similar average diameter, k_{r} should be similar, at low-temperature values, a decrease in the experimental lifetime τ may be related to an increase in k_{m}.[166] Comparing the E2 exciton experimental lifetime τ values at 12 K for **Si NPs-C12** and **Si NPs-H** (Table 3.3), it is observed that τ is smaller for **Si NPs-H**. Thus, it may be concluded that exciton migration is more likely to occur in **Si NPs-H** (Figure 3.15A) than in the case of **Si NPs-C12** (Figure 3.15B), due to the thinner inter-NP energy barrier represented by the Si-H termination when compared to the barrier imposed by the long chain surface ligands. Interestingly, after surface-oxidation (**Si NPs-C12-O**) the experimental lifetime value is closer to that of **Si NPs-H** (Table 3.3). The inter-NP energy barrier in **Si NPs-C12-O** is increased, when compared to that of **Si NPs-C12**, and, therefore, inter-NP exciton transfer would be expected to be even less likely to occur. Thus, one could expect that k_{m} would be lower in **Si NPs-C12-O** than in **Si NPs-C12**. It may be that in the case of **Si NPs-C12-O** there is an additional process that competes with the processes that take place in **Si NPs-C12** (and in **Si NPs-H**), associated with exciton migration from the crystalline core of the Si NPs to the surface oxide shell (path i in Figure 3.15C), which is not present in **Si NPs-C12** (and in **Si NPs-H**). In this case, excitons may recombine via electronic states associated with the surface oxide, leading to the oxide-related emission E1 observed for **Si NPs-C12-O**.

The low-temperature excitation spectra recorded for the Si NPs provide additional evidence in support that exciton transfer is indeed taking place from the NP crystalline core to electronic states associated with the surface-oxide shell. Comparing the excitation spectra of the Si NPs with the absorption spectrum of crystalline bulk Si,[34] it may be concluded that the excitation components at 270 nm (4.6 eV) and 365 nm (3.4 eV) are also present in the absorption spectrum of bulk Si. The absorption component of bulk Si at 365 nm (3.4 eV) is associated with the direct $\Gamma_{25} \rightarrow \Gamma_{15}$ transition and the one at 295 nm (4.2 eV) corresponds to a second direct $\Gamma_{25} \rightarrow \Gamma_{2'}$ transition or a direct transition at *X*.[33, 81, 82] The presence of these components in the excitation spectra of **Si NPs-C12-O** and the observation of emission associated with the

surface oxide (E1 emission mentioned above) demonstrates that there is charge transfer between the NPs core and shell oxide states.

Comparing the excitation spectra of **Si NPs-C12** and **Si NPs-H** with the absorption spectrum of crystalline bulk Si (Figure 3.11), a relative intensity decrease in the low-wavelength excitation region (≈270 nm) is observed. It may be inferred that excitons generated by photons with higher energies are the ones that are more likely to recombine non-radiatively. This is also supported by the observation that the relative intensity of the ≈270 nm spectral region of the excitation spectrum is lower for the **Si NPs-H** than for **Si NPs-C12** (Figure 3.11), and taking into account that the quantum yields found for **Si NPs-C12** are considerably higher than the values found for **Si NPs-H**.

At room temperature, the E2 exciton lifetime values decrease for all Si NP samples, compared with that found at 12 K (Table 3.3) due to the confined excitonic triplet and singlet states, whose occupation depends on the temperature. At room temperature the excitons are predominantly photocreated in a singlet state, which present a faster radiative lifetime, as studied for porous Si.[190] Nevertheless, contrarily to that found at 12 K, **Si NPs-C12** and **Si NPs-C12-O** have similar τ values at room temperature, which correlates well with the similar η values obtained for these samples. Interestingly, it is inferred from these observations that the native oxide formed on the organic-functionalized Si NPs does not lead to a decrease of the quantum yield, which means that nearly all of the excitons transferred to oxide-related states contribute to light emission. Moreover, the lower lifetime value found for **Si NPs-H**, when compared to **Si NPs-C12**, correlates also well with the higher η values found for **Si NPs-C12**, which confirms the role played by thermally-activated nonradiative recombination mechanisms in limiting the η exhibited by Si NPs at room temperature.

The inter-NP exciton transfer processes considered in this work to explain the steady-state and time-resolved photoluminescence data may also be used to discuss previous observations for other organic-functionalized Si NPs. Reports concerning the measurement of emission quantum yield for organic-functionalized Si NPs in the form of films are scarce, being reported a η=0.132 for Si NPs functionalized with trimethoxypropylsilane,[191] which is lower than that of **Si NPs-C12**. Other reports for

Si NPs in film are related to Si NPs with Si oxide at the surface (Table 1.1, section 1.1). The majority of the emission quantum yield data for organically-functionalized Si NPs refers to Si NPs suspended in different solvents, as listed in Table 1.1, section 1.1. Despite all the experimental variables that may influence the quantum yield values, the comparison between data in Table 1.1, section 1.1 evidences that Si NPs with larger average diameter (*d*) seem to yield higher η values, as already pointed out in other reports.[69] The comparison between η values measured for Si NPs with identical *d* suggests also that η increases as the length of the organic chains increases. This is verified when comparing the η values of Si NPs functionalized with 1-dodecene (η=0.70) with those of Si NPs functionalized with octadecene (η=0.62), and when comparing Si NPs functionalized with octanol (η=0.23) with Si NPs functionalized with allylamine (η=0.10). Longer organic ligands should impose a thicker energy barrier for the transfer of excitons between NPs (Figure 3.15B), which results in a decrease in the probability of nonradiative recombination and, conversely, in an increase in quantum yield.

3.3 Conclusions

The emission properties of Si NPs with different surface terminations were studied. Under UV/visible excitation, oxidized surface Si NPs with an average Si-core diameter of 3.4 nm display a broad emission formed by two components: one centered at ≈800 nm (1.55 eV) with a radiative lifetime of 0.424±0.003 ms and another centered at ≈700 nm (1.77 eV) with a radiative lifetime of 0.189±0.001 ms. These emission components are attributed to recombination of photogenerated electrons and holes located in the Si-core of the Si NPs and to donor-acceptor recombination within states associated with native oxide shell, respectively. It was concluded that both emission components are excited through electronic states of the Si NP core, showing the presence of core-to-shell charge transfer processes. It was also shown that the light emission properties of Si NP ensembles are not determined solely by the properties of individual NPs but are also governed by inter-NP charge transfer. The presence of the natural oxide shell hinders inter-NP charge transfer, resulting in a higher quantum yield than that of hydrogen-terminated Si NPs. Reduction of inter-NP charge transfer also

accounts for the high quantum yields observed for oxidized surface Si NPs when the average inter-nanocrystal separation is increased by suspending the Si NPs in solution.

The light emission properties of organic-functionalized Si NPs were also studied, namely hydrogen-terminated Si NPs (**Si NPs-H**) and 1-dodecene-functionalized Si NPs (**Si NPs-C12**) with the same average core diameter (2.4 nm). Both Si NP types display a similar single emission band at ≈1.64/1.84 eV at 300/12 K (denoted E2 emission), ascribed to recombination of photogenerated excitons in the Si-core of the Si NPs. **Si NPs-C12** display much higher room temperature quantum yield (η≈0.23) and excitonic lifetime values at 300/12 K of τ≈0.121/1.54 ms compared with those of Si NPs-H of η≤0.03 and τ≈0.083/0.41 ms (at 300/12 K). These differences reveal that nonradiative recombination mechanisms, which compete with light emission, are enhanced in **Si NPs-H**. It was concluded that the nonradiative recombination mechanisms are associated with inter-NP exciton migration. The impact of the formation of a native oxide shell on the surface of **Si NPs-C12** was also studied. After surface oxidation, the emergence of a second emission component (denoted E1 emission) associated with recombination via electronic states of the oxide (surface/interface states) is observed, demonstrating that part of the excitons generated in the Si NPs are transferred to oxide-related states. Despite the appearance of the E1 component, for **Si NPs-C12** no significant quantum yield variation is observed after surface oxidation as the oxide shell does not impose a significant additional barrier for exciton transfer when compared to the barrier provided by the organic termination. Moreover, it was inferred that in **Si NPs-C12** nearly all excitons transferred to oxide-related states contribute to light emission and, therefore, there is no significant nonradiative recombination via oxide-related states. In general, the study unveils the central role played by inter- and intra-NP exciton migration processes for the light emission properties of Si NPs. The study points out that the higher quantum yields generally found for organic-terminated Si NPs may also result from the contribution of the inhibition of inter-NP exciton transfer (responsible for nonradiative recombination).

Chapter 4. Primary luminescent thermometers[192]

4.1 Introduction

In this chapter, it is presented the application of the luminescent properties of Si NPs to the measurement of temperature, by using these as luminescent thermometers.

Measuring temperature at micro- and nanoscale is a critical task in many scientific investigations and technological developments.[193-197] The biomedical field, and in particular the possibility of mapping the temperature of living cells, is probably one of the most important and demanding applications for nanothermometry,[193, 198, 199] in which the nanothermometers need to combine an operation temperature range that coincides with the physiological one (295-320 K)[193] with biocompatibility, noninvasiveness, and working in moving biological fluids. Other applications requiring wider temperature intervals[200-206] will also benefit from nanothermometry, such as electronic and optoelectronic devices and circuits that are being continuously miniaturized, whose temperature strongly affects their performance.[194, 207, 208]

Within the diverse approaches to nanothermometry, luminescent probes are one of the most attractive as they are non-invasive, contactless, and easy to use, unlike conventional tools, such as thermocouple and fiber optic probes or volumetric methods (*e.g.* ultrasound, computed tomography, and magnetic resonance thermometry).[209] Additionally, luminescent probes can combine competitive spatial ($<10^{-4}$ m) and temporal ($<10^{-3}$ s) resolutions, allowing down to sub-micrometric resolution with a measurement based on the temperature dependence of the photophysical properties, also known as the thermometric parameter (Δ), of the materials, such as the steady-state emission intensity of one[203, 210] or two transitions[211, 212] and the lifetime[99, 203] (or risetime)[213, 214] of an excited state (Figure 4.1). Several emission centers such as organic dyes,[215, 216] polymers,[217] layered double hydroxides,[218, 219] QDs,[220, 221] and trivalent lanthanide ions (Ln^{3+})[193, 194, 211, 222-227] have been used as luminescent nanothermometers, as reviewed elsewhere.[193, 194, 197, 228, 229]

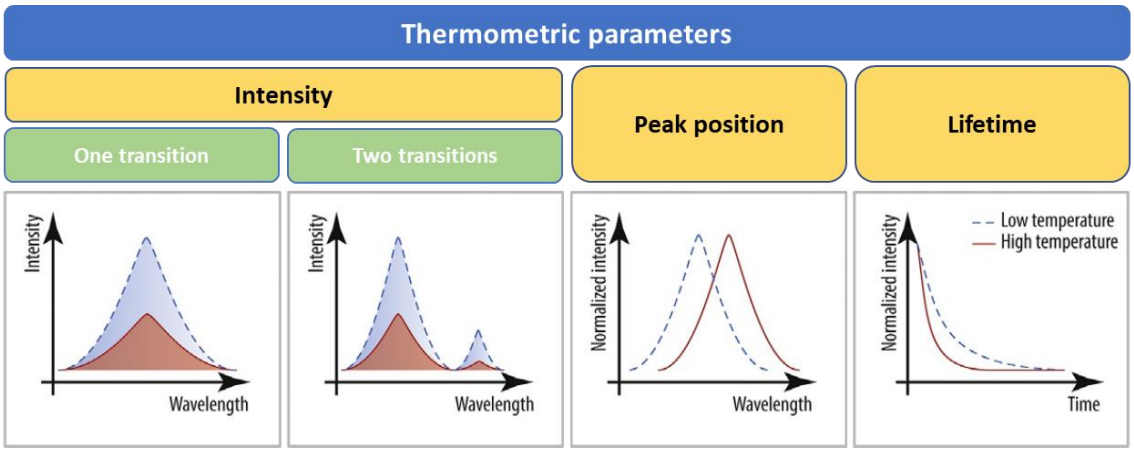

Figure 4.1 Examples of thermometric parameters used by luminescent thermometers (adapted).[230]

Thermometric systems can be classified according their Δ, as shown in Figure 4.2. Use of the emission intensity of a single transition as the thermometric parameter is compromised by variations in the sensor concentration, material non-homogeneity effects, and optoelectronic drifts in the excitation source and detecting system or optical occlusions.[193, 231, 232] In order to overcome these drawbacks, some temperature measurements use the following as Δ: (i) the intensity ratio of two transitions (ratiometric thermometers),[193, 194] (ii) the emission peak position,[193, 233, 234] (iii) the lifetime,[203, 231] or (iv) a neural recognition method based on peak and integrated intensity.[235] These strategies allow the development of self-calibrated (or self-referencing) thermometers.[193]

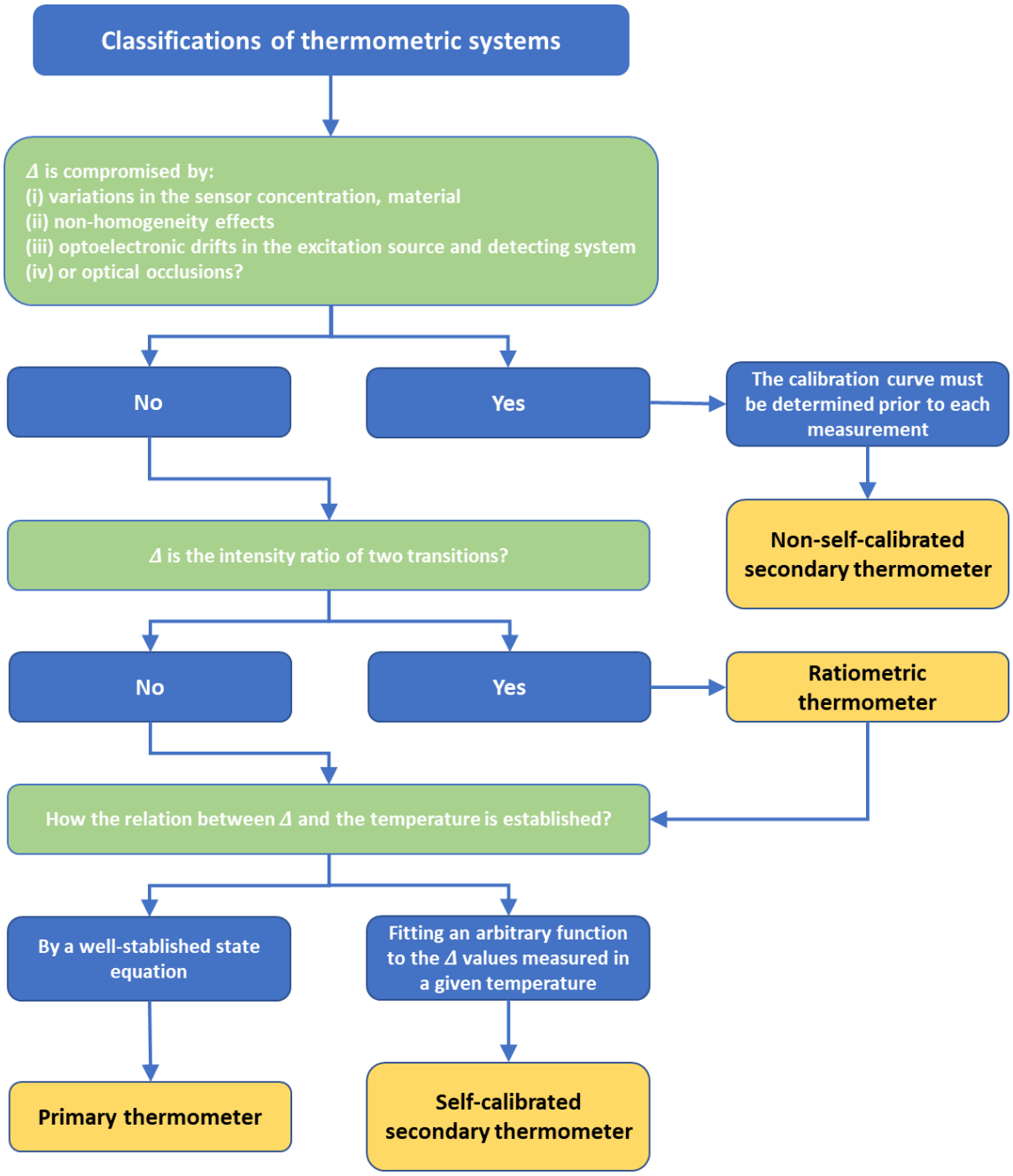

Figure 4.2 Diagram showing the classification of thermometric systems.

Thermometric systems can be classified in two categories: (i) primary or semi-primary thermometers that are characterized by well-established equations of state, directly relating the measured parameter to temperature, or (ii) secondary thermometers that require calibration.[193, 197, 236] While for non-self-calibrated secondary thermometers, the calibration curve must be determined prior to each measurement, for self-calibrated secondary thermometers, the calibration curve is obtained by modelling the thermometric parameter values measured in a given temperature range with an arbitrary function.[99, 193, 234] If other variables besides

temperature, *e.g.*, the ionic strength, pH, pressure, or atmosphere composition, impact the thermometric parameter value, a recalibration procedure must be performed as the empirical functions are not supported by theoretical or phenomenological model. On the contrary, when the relation between the thermometric parameter and the temperature is given by a well-established state equation,[211, 212, 233] the influence of these other variables can be taken into account if the thermometer needs to be recalibrated. This avoids the need of a new calibration every time the thermometer operates in a different media, which sometimes in not a trivial task *e.g.*, in living cells and in electronic devices.[237] A well-established state equation relating Δ to temperature, also allows to evaluate if Δ only dependents on the temperature or if Δ is also dependent on other variable that may change from media to media or from measurement to measurement.[230]

While many examples of primary thermometers based on the temperature dependence of gas properties, the radiation emitted by a black body, or the power spectral density of Johnson-noise in a resistor have been reported in the literature,[238-240] examples of primary luminescent thermometers are very rare. It can be mentioned CdSe(ZnS) QDs in which Δ (the emission peak position) is described by the Varshni's law (295-525 K)[233] and Y_2O_3:Eu^{3+} micro- and NPs in which Δ is defined as the ratio between the emission intensities of the $^5D_0 \rightarrow {}^7F_4$ transition when the $^5D_0$ emitting level is excited through the $^7F_2$ and $^7F_0$ levels (physiological temperatures) or through the $^7F_1$ and $^7F_0$ levels (for temperatures down to 180 K).[212, 237]

In this study, Si NPs functionalized with 1-dodecene were used to produce film- and solution-based luminescent nanothermometers. Si NPs are an attractive choice for nanothermometry as they combine tunable emission from the near-infrared to visible spectral range[38] with properties such as the material abundance,[5] potential compatibility with the current microelectronic technology,[43, 241] and biocompatibility.[8, 242] Despite this great potential, few have reported the use of Si NPs as nanothermometer, and the research has been limited to Si NPs dispersed in a liquid medium.[99, 100, 234, 243] Using a hyperspectral camera (pixel field-of-view of 1.3×1.3 μm^2), it is shown that the film's surface emission is homogenous, at least, at the microscale. It is demonstrated here, for the first time, that luminescent thermometers based on Si NP films and solutions, with thermometric parameter predicted by a well-established

equation, enable temperature sensing independent of the medium (air, vacuum, nitrogen atmosphere). The nanothermometer calibration curve is predicted by Varshni's law and allows temperature sensing in a wide range of temperatures from cryogenic to 480 K, with maximum relative sensitivity of 0.04 %.K^{-1} and reversibility and repeatability above 99.98 %.

4.2 Results and discussion

4.2.1 Structural characterization

The **as-prepared Si NPs-C12** were characterized by X-ray diffraction to evaluate their mean size. The XRD pattern (Figure 4.3) reveals reflections near 32.8°, 55.3°, and 66.1°, corresponding to (111), (220) and (311) Si crystal planes, respectively.[18, 164] Using Rietveld refinement of the Si phase, an average diameter value of 2.0±0.2 nm was calculated. The goodness of the fit was evaluated by the estimator $\chi^2=(R_{wp}/R_{exp})^2$, yielding $\chi^2=0.51$ (Figure 4.3). It should be noted that there is no absolute estimation of the refinement quality and that the χ^2 value depends on the diffraction intensity. Thus, combining graphical analysis with the chemical/physical plausibly of the model, it may be concluded that the refinement yields a realistic mean diameter size value of the Si NPs.

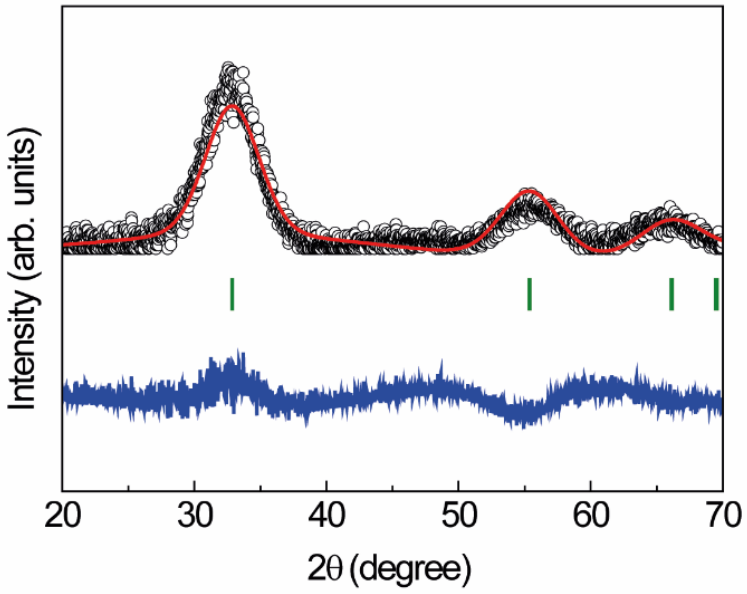

Figure 4.3 XRD pattern of the **as-prepared Si NPs-C12** (black circles). Continuous (red) line corresponds to Rietveld refinement of Si phase (R_p = 29.3 %, R_{wp} = 25.6 %, R_{exp} = 35.9 % and χ^2= 0.51). Vertical (green) lines represent the position of allowed Bragg peaks, while (blue) line represents the fit residues.

4.3.2 Film's surface emission homogeneity

Taking into consideration that temperature-sensing applications may require operation in distinct environments, the material stability is a concern. Applications as the use of thermometry in living cells or in electronic circuits require exposure to water and oxygen, which will lead to surface oxidation of the Si NPs, changing their emission spectra;[55] therefore, the more stable oxidized surface Si NPs are stronger candidates for operation in the different media compared to **as-prepared Si NPs-C12**. Accordingly to this, the study will focus on stable oxidized surface Si NPs (samples **Si NPs-C12-1** and **Si NPs-C12-2**).

The oxidized surface Si NPs display an emission visible to the naked eye in the orange-red spectral region, under a broad excitation wavelength range from the UV to the visible (240-600 nm) without a significant decrease in the η.[163] The possibility of exciting the Si NPs in the visible range permits to envisage applications also in biophotonics. Figure 4.4A shows an optical microscopy image illustrating the surface emission for a selected film.

The films emission was analyzed using a hyperspectral camera, and the emission spectra at the surface were mapped by monitoring different surface regions (Figure 4.4B and 4.3C). The emission spectrum collected by a single pixel (1.3×1.3 μm^2) shows a broad band in the orange-red spectral region peaking at ≈650 nm (green line, Figure 4.4D). By enlarging (20 times) the collection area, apart from an improvement in the signal-to-noise ratio, the spectrum (blue line, Figure 4.4D) overlaps that measured from a single pixel, suggesting homogeneous emission from the film surface.

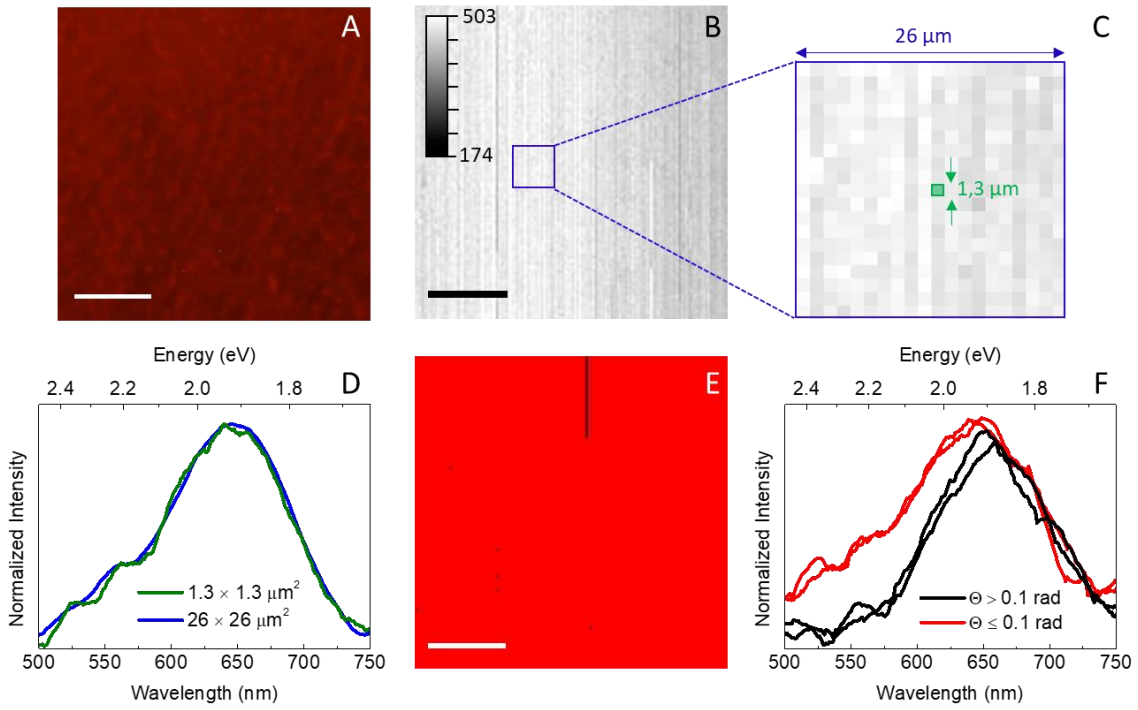

Figure 4.4 A) Optical and **B)** hyperspectral microscopy images of an oxidized surface Si NPs film surface under UV illumination. The grey scale intensity of the pixels is based on the intensity of the emission spectrum at 650 nm (the emission intensity variation arises from the spatial spectral power distribution of the excitation lamp). **C)** Magnification of the hyperspectral image. **D)** Emission spectra measured in a single pixel area (1.3×1.3 μm^2) and within an area limited by 20×20 pixels (26×26 μm^2). **E)** SAM classification for a threshold value of Θ=0.10 rad. **F)** Emission spectra measured in pixel areas with Θ≤ 0.10 rad and Θ> 0.10 rad in the SAM classification. All scale bars are 50 µm.

To further study the film spatial emission homogeneity over the total surface, the emission spectra were analyzed through SAM classification, where each emission spectrum is treated as a vector.[244] The SAM tool permits a rapid mapping of the spectral similarity between the spectra of any pixel of the film surface and a reference spectrum. The similarity criterion is based on an angle (Θ) that quantifies the angular distance between the vector that represents the emission spectrum at a given position with the

vector of the spectrum considered as reference.[244] Therefore, Θ=0 rad when the emission spectrum at a given position overlaps with the reference one. The values Θ=0.10 rad and Θ=0.20 rad have been considered as threshold values.[245] The reference spectrum is shown in blue in Figure 4.4D (measured in an area of 20×20 pixels, which is equivalent to 26×26 μm^2) in the 600-700 nm range and a similarity criteria with a threshold value of Θ=0.10 rad was considered. Figure 4.4E shows the SAM image in which the pixels in red and black correspond to Θ≤0.10 rad and Θ>0.10 rad, respectively. The ratio between the number of red and black pixels is ≈99.9 %, demonstrating the homogeneity of the emission of the oxidized surface Si NPs. To ease the interpretation of the SAM results, the spectrum arising from pixels with Θ≤0.10 rad and Θ>0.10 rad are shown in Figure 4.4F. It is notorious the large overlap of the spectra corresponding to red pixels (Θ≤0.10 rad) with the reference. Moreover, the mismatch between the emission spectra arising from black pixels (Θ>0.10 rad) and the reference is mainly due to changes in the fwhm rather than by a large shift of the emission peak position, which verifies that E_g can be used as the thermometric parameter.

4.2.3 Emission spectra a function of temperature

As the spatial homogeneity of the film emission is not a concern, the thermal dependence of the emission was further characterized using conventional photoluminescence techniques. The emission spectra of **Si NPs-C12-1** and **Si NPs-C12-2** comprise of a broad band (fwhm ≈0.33 eV) in the red spectral region, whose peak position at 300 K is ≈1.91 eV (650 nm) and ≈1.97 (630 nm), depending on the air exposure conditions, Figure 4.5A and 4.5B. Apart from a blue-shift, the emission spectra of the oxidized surface **Si NP-C12-1** and **Si NPs-C12-2** (Figure 4.5A and 4.5B) resemble that observed for the **as-prepared Si NPs-C12** (Figure 4.5C).

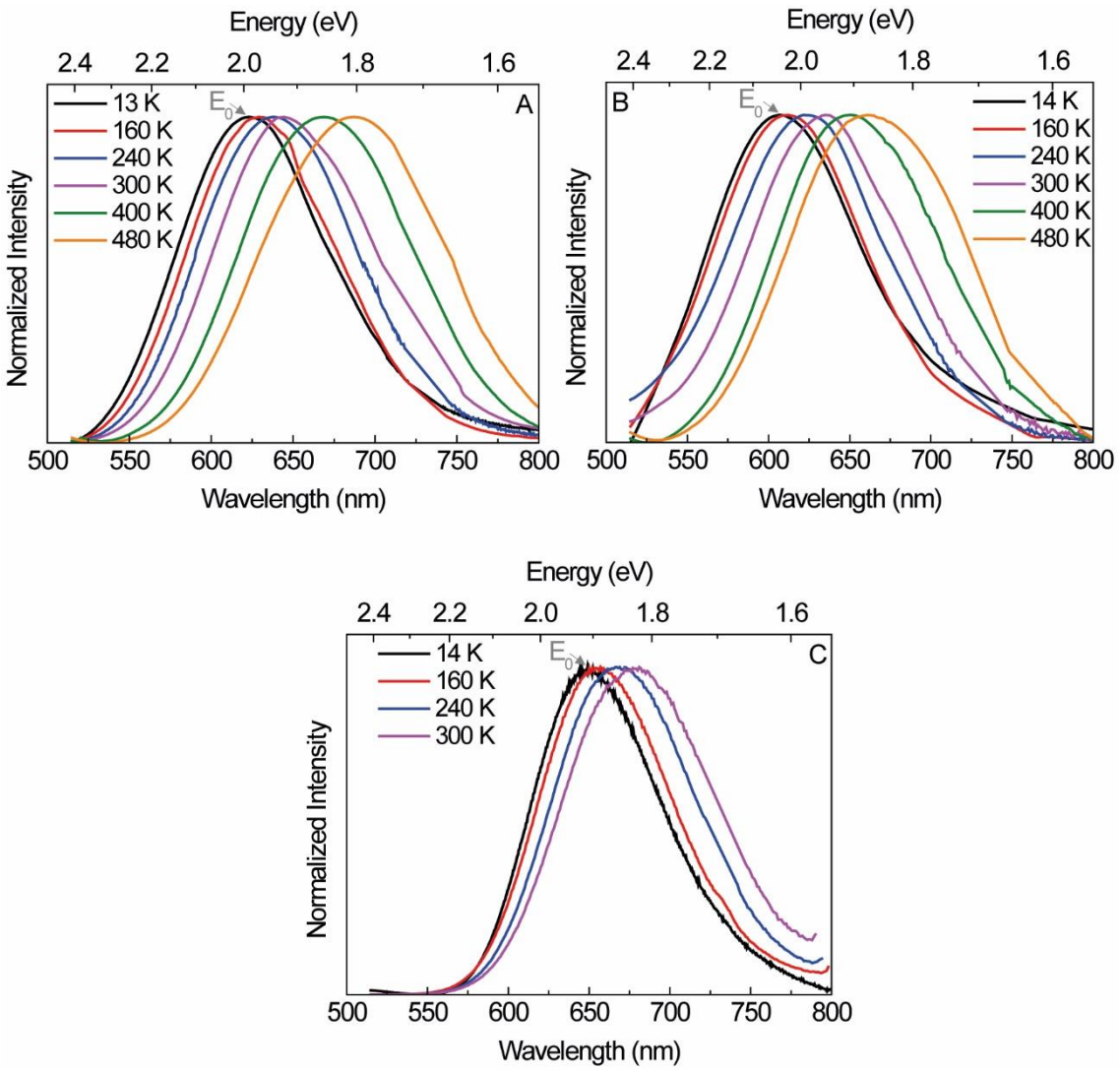

Figure 4.5 Emission spectra of films of (A) **Si NPs-C12-1**, (B) **Si NPs-C12-2**, and (C) **as prepared Si NPs-C12** excited at 365 nm and measured under vacuum at selected temperatures.

All the emission spectra display a single Gaussian profile (Figure 4.6) arising from recombination of photogenerated electrons and holes located in the crystalline core of the Si NPs. The observed blue-shift after air exposure is ascribed to the decrease of the Si crystalline core size induced by the surface oxidation that results in a wider band gap.[40] Although it is known that the presence of an oxide shell at the Si NPs surface contributes to the appearance of another emission component attributed to donor-acceptor pairs involving states associated with the native oxide shell,[162] the fact that the emission spectra of the oxidized surface **Si NP-C12-1** and **Si NPs-C12-2** are well modelled by a single Gaussian function (Figure 4.6), indicates that the contribution of the oxide-related component can be neglected, as already noticed for analogous Si

NPs,[162] in which the contribution of the oxide-related emission could only be discerned at low temperatures.[162]

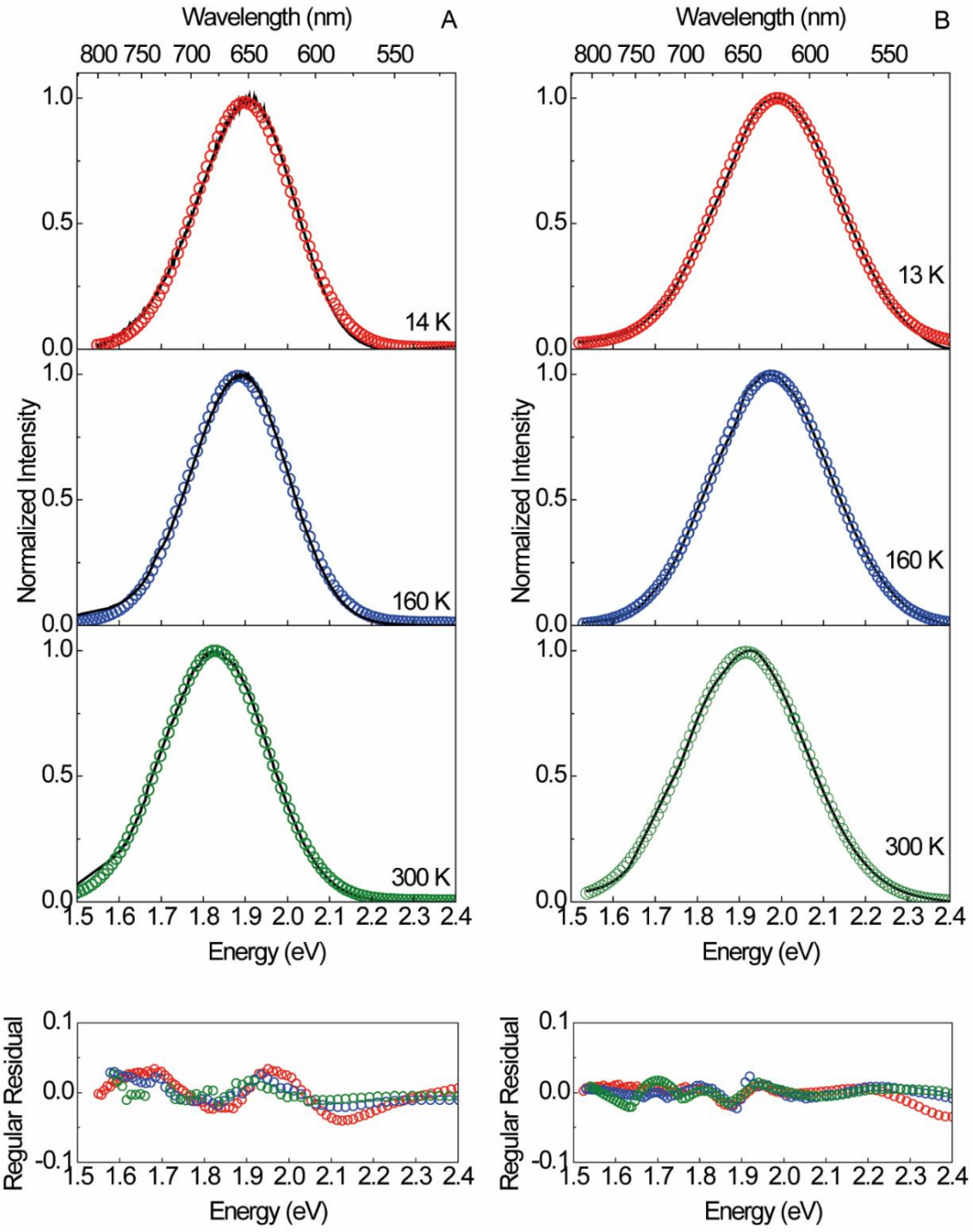

Figure 4.6 Emission spectrum (13/14 K, 160 K and 300 K) of (A) **as-prepared Si NPs-C12** and (B) **Si NPs-C12-1** excited at 365 nm. The open symbols correspond to the data best fit (r^2>0.99) with a single Gaussian function. The fit regular residual plots are shown at the bottom.

Focusing on the application as luminescent nanothermometers, the emission spectra of the samples were studied from low-temperature (13 K) to values near the Si NPs melting point (500 K).[246] In all cases, the emission spectra shifted to the red as the temperature is raised, as shown in Figure 4.5 for selected temperature values. In order to use the oxidized surface Si NPs as luminescent nanothermometers, the phenomenological Varshni's law[247] that describes the temperature (T) dependence of the emission band gap (E_g),

$$E_g(T) = E_0 - \frac{\alpha T^2}{T + \beta} \tag{4.1}$$

which corresponds to the emission peak position, where E_0 is the energy gap at 0 K and α and β are constants, can be used as predictable calibration curve. Thus, the values of E_0, α and β must be known prior to the sensing measurements. The parameter E_0 is determined by considering the energy peak position at ≈14 K (marked in Figure 4.5A and 4.4B); β is related to the Debye temperature (645 K), being β=1108 K for bulk Si.[247] The α parameter is essentially phenomenological and its value is on the order of 10^{-3} eV.K^{-1} for Si NPs[248] and bulk Si[247] and is known to be constant for Si NPs with average diameters around 2 nm.[248] Thus, to independently determine the α value for the oxidized surface Si NPs, the emission thermal dependence of E_g for the **as-prepared Si NPs-C12** (Figure 4.5C) was modelled with Equation (4.1). Despite the fact that the emission spectra are well modelled by a single Gaussian function (Figure 4.6), the E_g values were determined by modelling the emission spectra to a single Gaussian function in the energy range that presents intensity values of at least 60 % (Figure 4.7A) of the maximum intensity peak position, enabling a more accurate E_g determination. From the data modeling with Equation (4.1) (Figure 4.7B), a value of α=(1.26±0.02)×10^{-3} eV.K^{-1} was obtained, using β=1108 K and E_0=1.907±0.002 eV. Figure 4.7A shows the fit with a single Gaussian function used to determine the emission peak position of the spectrum measured at 14 K (considered as the value of E_0). The energy peak value determined with the fit is 1.9071±0.0003 eV. Considering that the spectral resolution of the measurement is 2×10^{-3} eV, this should be the uncertainty value for the energy peak.

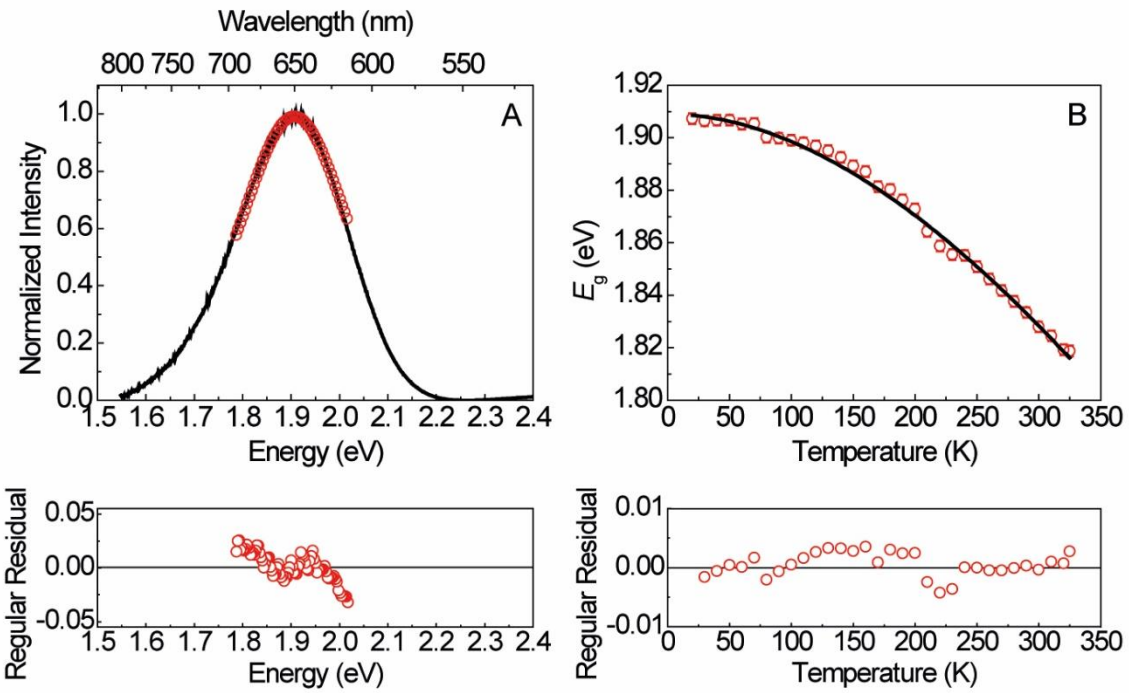

Figure 4.7 A) Emission spectrum of a film of **as-prepared Si NPs-C12** excited at 365 nm and measured under vacuum at 14 K. The open circles correspond to the data modelling (r^2>0.98) with a single Gaussian function in the range that presents intensity values of at least 60 % of the maximum intensity peak position. **B)** Thermal dependence of the emission peak position for films of the **as-prepared Si NPs-C12** measured under vacuum. The solid line corresponds to the data best fit mission spectrum (r^2>0.99) with Equation (4.1). Fit regular residual plot (bottom).

This procedure enables to independently establish the calibration curves for the luminescent thermometers based on the oxidized surface Si NPs by replacing in Equation (4.1) the values of all parameters. These calibration curves are

$$E_g(T) = 1.993 - \frac{1.26 \times 10^{-3} \times T^2}{T + 1108} \tag{4.2}$$

$$E_g(T) = 2.044 - \frac{1.26 \times 10^{-3} \times T^2}{T + 1108} \tag{4.3}$$

for **Si NPs-C12-1** and **Si NPs-C12-2**, respectively. E_0=1.993±0.002 eV (**Si NPs-C12-1**) and E_0=2.044±0.002 eV (**Si NPs-C12-2**) were determined from emission spectra measured at ≈14 K. Although E_0 value depends on the Si NPs size its value is independent of the operating conditions, thus, it ensures that the Si NPs-based thermometers are primary. The error (ΔE_g) associated with the calculation of E_g is given by

$$(\Delta E_g)^2 = \left(\frac{\partial E_g}{\partial E_0}\,\Delta E_0\right)^2 + \left(\frac{\partial E_g}{\partial \alpha}\,\Delta\alpha\right)^2 + \left(\frac{\partial E_g}{\partial T}\,\Delta T\right)^2 \Leftrightarrow$$

$$\Leftrightarrow (\Delta E_g)^2 = (\Delta E_0)^2 + \left(-\frac{T^2}{T+\beta}\Delta\alpha\right)^2 + \left(-\frac{2(T+\beta)T\alpha - \alpha T^2}{(T+\beta)^2}\Delta T\right)^2 \qquad (4.4)$$

in which ΔE_0=2×10^{-3} eV is the peak experimental uncertainty, ΔT=0.1 K is the temperature experimental resolution, and $\Delta\alpha$=0.02×10^{-3} eV.K^{-1} is the error of the parameter α resulting from the fit (Figure 4.7B). No error for β was considered as its value was taken from the literature (β=1108 K).[247]

Figure 4.8 shows the agreement between the values experimentally obtained with the oxidized surface Si NPs for the thermometric parameter, *i.e.* the emission peak position (E_g), and the values predicted by the Equation (4.2) and (4.3).

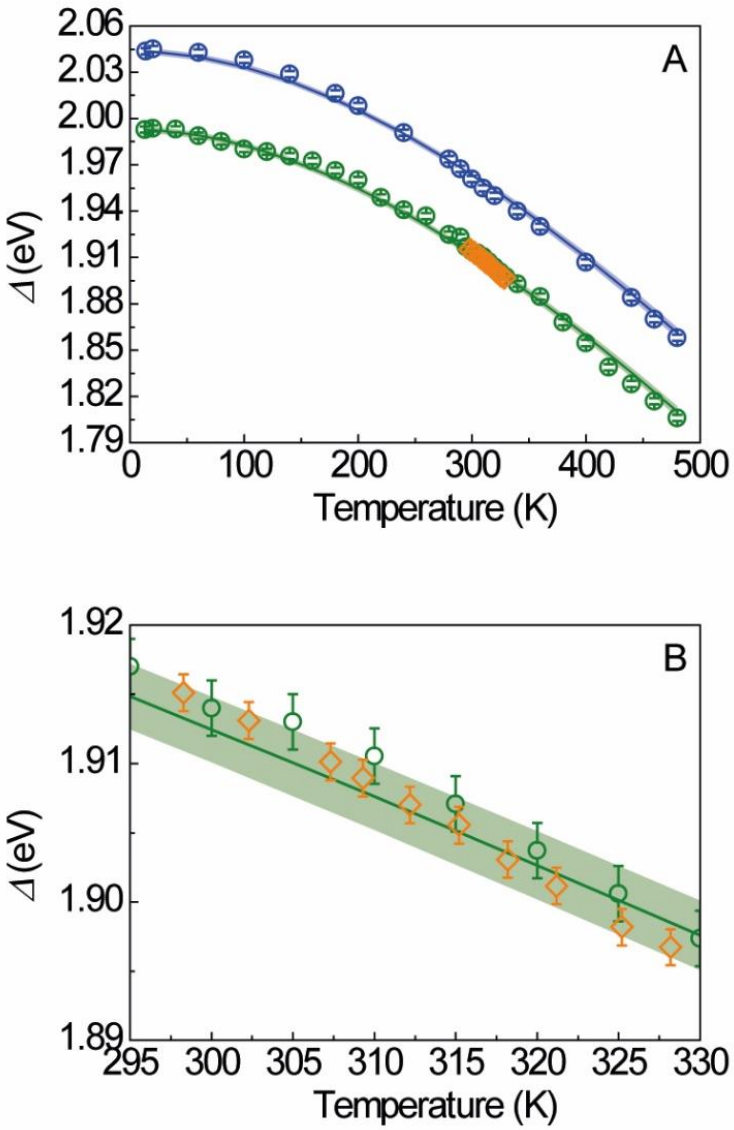

Figure 4.8 A) Thermal dependence of the emission peak position for films of **Si NPs-C12-2** under vacuum (blue circles) and of **Si NPs-C12-1** under vacuum (green circles) and in a nitrogen atmosphere (orange rhombus). The green and blue lines show the values predicted by Equations (4.2) and (4.3), respectively. **B)** Magnification of the region within 295-330 K. The shadowed area represents the error of the values given by Equation (4.4).

4.2.4 Figures of merit of the thermometer

The thermometer performance can be evaluated using the relative thermal sensitivity (S_r)[193, 249, 250] that is defined as the relative change of Δ with the temperature

$$S_r = \frac{1}{\Delta}\left|\frac{\partial \Delta}{\partial T}\right| \tag{4.5}$$

Applying this definition to Equation (4.1) results in

$$S_r(T) = \frac{1}{E_0 - \frac{\alpha T^2}{T+\beta}} \frac{2\alpha T(T+\beta) - \alpha T^2}{(T+\beta)^2} = \alpha T \frac{2 - \frac{T}{(T+\beta)}}{E_0(T+\beta) - \alpha T^2} \tag{4.6}$$

The error (ΔS_r) associated to the calculation of S_r is given by

$$(\Delta S_r)^2 = \left(\frac{\partial S_r}{\partial E_0}\Delta E_0\right)^2 + \left(\frac{\partial S_r}{\partial \alpha}\Delta\alpha\right)^2 \Leftrightarrow$$

$$\Leftrightarrow (\Delta S_r)^2 = \left(\frac{-\alpha T\left(2 - \frac{T}{T+\beta}\right)(T+\beta)}{(E_0(T+\beta) - \alpha T^2)^2}\Delta E_0\right)^2 + \left(\frac{\left(T\left(2 - \frac{T}{T+\beta}\right)\right)\left(E_0(T+\beta)\right)}{(E_0(T+\beta) - \alpha T^2)^2}\Delta\alpha\right)^2 \tag{4.7}$$

The relative thermal sensitivity for **Si NPs-C12-1** and **Si NPs-C12-2** increases with rising temperature, with sensitivity being ≈0.03 %.K^{-1} at room-temperature (Figure 4.9A). ΔS_r calculated using Equation (4.7) yields a relative error ($\Delta S_r/S_r$) of ≈1 %.

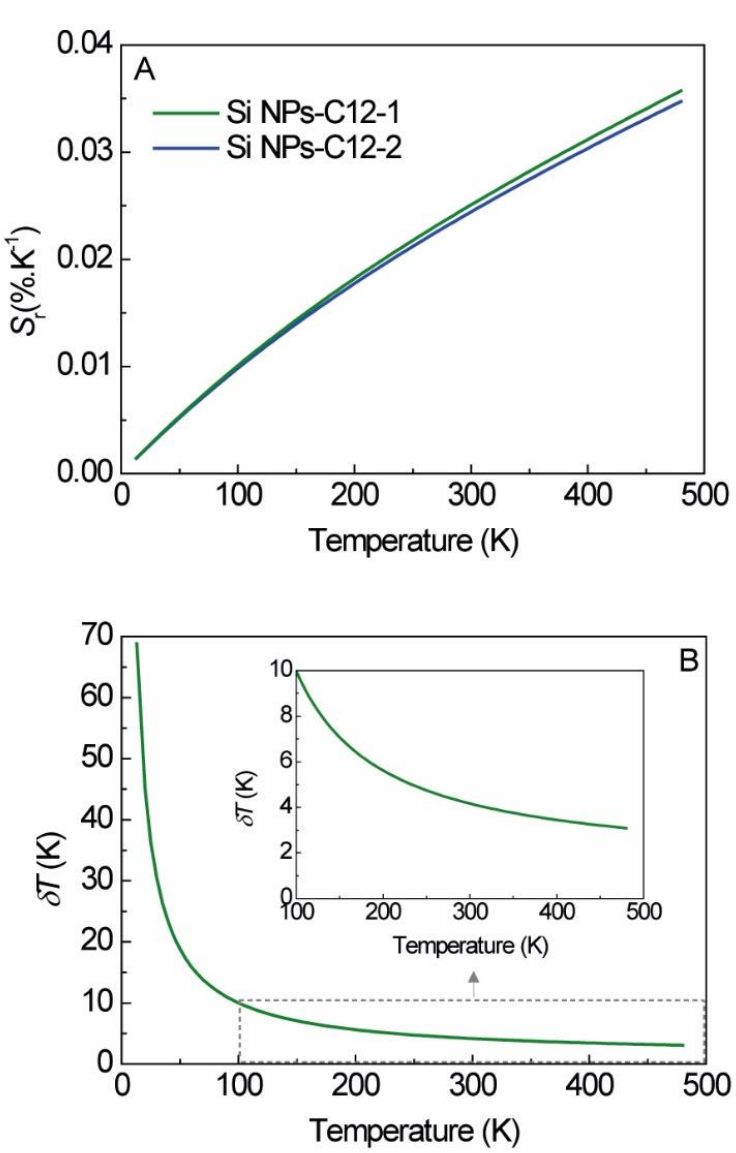

Figure 4.9 A) Relative thermal sensitivity for films of **Si NPs-C12-1** and **Si NPs-C12-2**. The relative error $\Delta S_r / S_r$ is ≈1 %. B) Temperature uncertainty for **Si NPs-C12-1**. The inset shows a magnification for the region within 100-500 K. The temperature uncertainty values are the same for **Si NPs-C12-2**.

Despite the existence of previous reports on the temperature dependence of the peak emission position of Si NPs, only a small number of works addressed the use of Si NPs as nanothermometers and only for Si NPs in solution.[99, 100, 234, 243, 251] The S_r values for the thermometers based on oxidized surface Si NPs are similar to those reported for surface-functionalized Si NPs in a squalane solution (0.052 %.K^{-1}) in the interval 303-390 K.[234] In the latter case, the emission thermal dependence for alkyl-terminated Si NPs dispersed in low-polar liquids cannot be well predicted by Equation (4.1), due to the high viscosity of the solvents and broad nanoparticle size distribution that induce exciton

migration mechanisms.[100, 234] The good agreement between Varshni's law and the experimental results indicates that exciton migration[162] can be neglected and the emission thermal dependence is mainly governed by the temperature induced shrinkage of the band gap. Other S_r values reported for thermometers based on Si NPs in solution refer to distinct thermometric parameters, namely emission lifetime (0.75 %.K^{-1})[99] and emission integrated intensity (0.8 %.K^{-1})[243] in the temperature ranges 293-393 K and 293-373 K, respectively, one order of magnitude above the value reported in this work. The temperature uncertainty (δT) was computed using

$$\delta T = \frac{1}{S_r}\left|\frac{\delta \Delta}{\Delta}\right| \tag{4.8}$$

where $\delta \Delta$=2×10^{-3} eV is the absolute uncertainty on the determination of the thermometric parameter and corresponds to the spectral resolution of the measurement. Equation (4.8) yields the thermal uncertainty plotted in Figure 4.9B. At low temperatures the δT is high due to the low values of S_r. Despite that, as the temperature increases (T>100 K), δT decreases to values below 10 K as a result of the increase of S_r. The temperature uncertainty is determined both by the material emission features (fwhm and emission quantum yield) and by the spectral resolution of the equipment (photodetector gain and grating or CCD resolution). Obviously, if NPs with higher quantum yield values are used, the absolute uncertainty on the determination of the thermometric parameter will be improved, as it will be possible to perform the experimental measurement under the maximum resolution of the equipment which is 10^{-4} eV in the visible spectral range for a nominal spectral dispersion of 2.64 nm.mm^{-1}. In this case, δT<3.5 K and δT<0.5 K for low temperatures values and above 100 K, respectively.

4.2.5 Thermometric operation in different media

Despite the fact that the use of vacuum conditions is required, for instance, in cryoprotective environments (*e.g.* living cells), space applications and opto-electronic devices, it is not compulsory or sometimes even not desired for temperature sensing near (or above) room temperature. Thus, it is pertinent to analyze the effect of the

atmosphere on the thermometric parameter, in particular, if the thermometer based on oxidized surface Si NPs requires a new calibration whenever operated in different media. Thus, the performance of the thermometer based on the **Si NPs-C12-1** was evaluated in air and in a nitrogen atmosphere in the temperature range ≈298-328 K. Nitrogen-filled environments can be found, for instance, in glove boxes used to handling both hazard substances and air sensitive materials. The thermal dependence of E_g under a nitrogen atmosphere is represented in Figure 4.8, which is also well described by Equation (4.2). Additional evidence suggesting the independence of Δ on the atmosphere in which the measurements are performed can be found in Figure 4.10 where the spectra of the film measured in air and vacuum overlap.

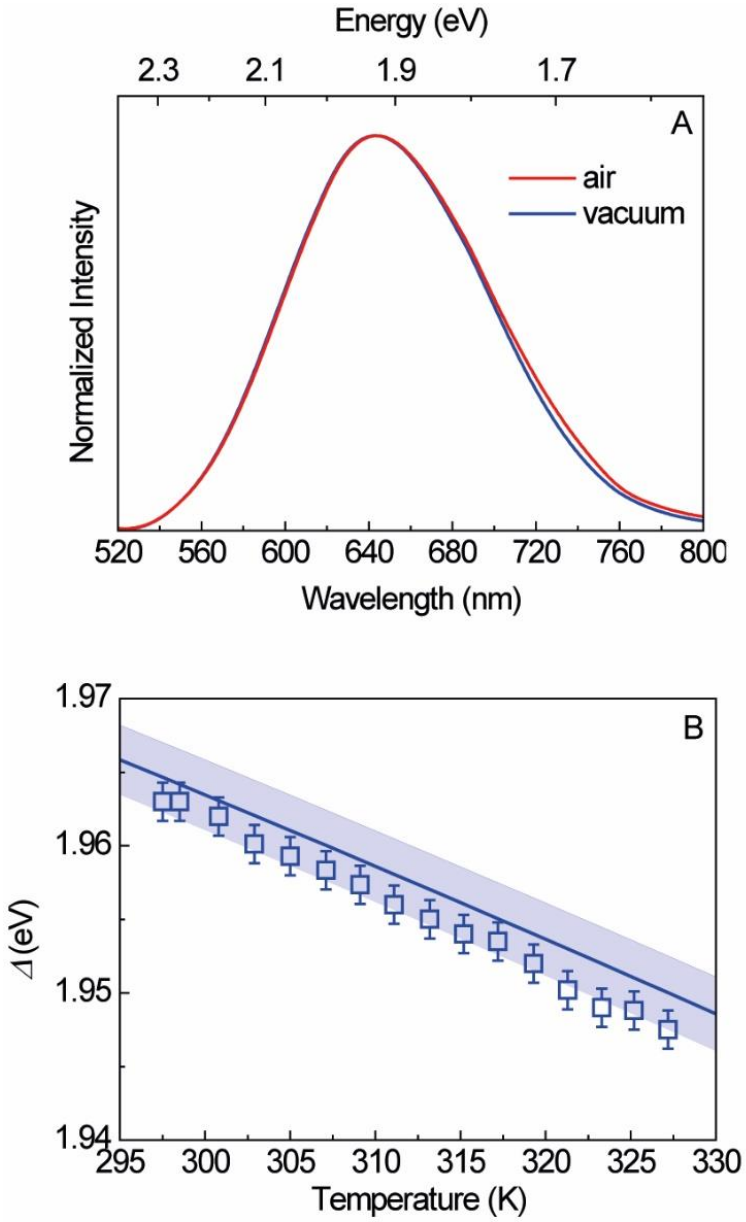

Figure 4.10 A) Emission spectra of a film of oxidized surface Si NPs acquired in air and vacuum at 293.7 K and 295.2 K, respectively. The excitation wavelength was 365 nm. **B)** Thermal dependence of the emission peak position of **Si NPs-C12-2** in solution, measured in air (squares). The solid line shows the values predicted by Equation (4.3) and shadowed area represents the respective error.

The thermometric performance of **Si NPs-C12-2** was also evaluated in solution measured in air in the temperature range 297.5-327.2 K. The emission thermal dependence is shown in Figure 4.10B and is also well predicted by Equation (4.3), reinforcing that the Si NPs are self-calibrated primary thermometers whose performance is described by a predictable, well-established state equation.

4.2.6 Repeatability and reversibility of the thermometric measurements

The repeatability and reversibility were studied for films of **Si NPs-C12-1** in air around room temperature (Figure 4.11A) and under vacuum at lower temperature values between 20.0-250.0 K (Figure 4.11B). Under consecutive heating-cooling cycles, all the thermometers present reversibility and repeatability higher than 99.99 %, being only limited by the experimental uncertainty in the determination of Δ. The test-retest reliability tests performed with **Si NPs-C12-2** in solution are shown in Figure 4.11C, revealing reversibility and repeatability higher than 99.98 %, demonstrating that the use of the oxidized surface Si NPs in toluene solution does not compromise their performance as a thermometer.

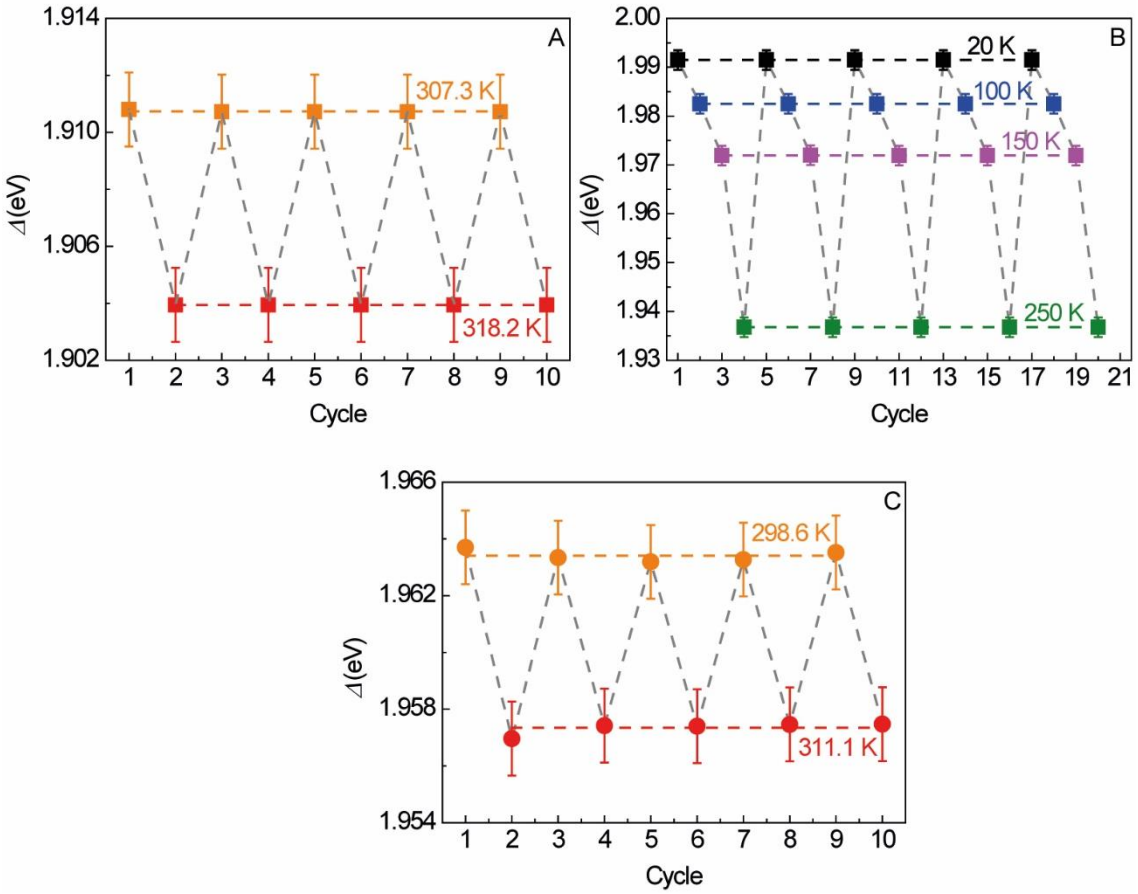

Figure 4.11 Variation of the thermometric parameter in the indicated temperature cycling range. The measurements were performed for **Si NPs-C12-1** in (A) air and (B) vacuum, and for (C) **Si NPs-C12-2** in solution, measured in air. The lines are guides for the eyes.

4.3 Conclusions

The performance of luminescent Si NPs as nanothermometers was evaluated in the 13-480 K temperature range. Independent of the sample processing (film or solution) and the environment, the dependence of the emission energy with temperature is well described by Varshni's law and can be used as the thermometric parameter, *i.e.* $\Delta = E_g$. This finding, that Δ of a nanothemometer can be predicted by a well-established equation, resolve some concerns regarding the robustness of the nanothermometer and the need for calibration in each new measurement environment, making this one of the very few examples of a primary thermometer. The reversibility and repeatability of the thermometer is higher than 99.98% and the maximum relative thermal sensitivity is 0.04 %.K^{-1}. The possibility of extending the use of Si NPs to the biomedical field is highly potentiated by the advantages of Si (*e.g.* cost, biocompatibility, and abundance). Future research should be directed to the production of narrower size distribution and water dispersible Si NPs in combination with the enhancement of the optical properties featuring higher relative thermal sensitivity approaching the best figure of merit (0.4-3 %.K^{-1}, in the physiological range).[230]

In a global way, the fact that Varshni's law is general for bulk semiconductors and semiconductor NPs, the methodology reported here can be widely explored, leading to a new generation of multi-functional semiconducting QD phosphors with the ability to sense temperature at the nanoscale in which novel developments in the field of biophotonic and nanophotonics[252] may be expected and a new generation of photon converters based on semiconducting QDs may be explored. This may extend multimodal bioimaging to temperature sensing in the interior of a nanoparticle and allow the combination of NP-based imaging with drug and gene delivery, therapy, or diagnosis.[54]

Chapter 5. Deposition of Al_2O_3 by ALD on films of silicon nanoparticles

5.1 Introduction

In chapter 3, it was shown that the surface of the Si NPs plays a key role on their photoluminescence properties. In order to take advantage of the photoluminescence properties of the Si NPs and get practical applications with commercial success it is necessary to develop devices that keep their properties stable over time. There are several systems of Si NPs that are not stable in ambient conditions, as for example the Si NPs without oxide shell, as studied in the previous chapters. The operation in ambient conditions is a necessary requirement if one wants to apply the photoluminescence properties of the Si NPs in a broad range of applications, otherwise the success of the devices will be at risk or will be restricted to very few applications in conditions where the Si NPs are stable. Taking this in consideration, it becomes an important challenge the development of strategies that allow the systems of Si NPs to keep their properties stable over time in ambient conditions. One of the strategies that can be used to protect films of NPs from oxidation in ambient condition is the coating or infilling of the film with Al_2O_3.[253-255] This strategy was already successfully adopted for PbSe NPs,[253, 254] for CdSe/ZnS core-shell NPs,[255] and for Si NPs.[256]

The ALD is a technique that have been used to coat and infill films of NPs.[253-255] The ALD is a chemical vapor deposition technique, developed in the 1970s,[257-259] which allows film thickness control at the angstrom level, conformal deposition, and pinhole-free films.[257, 259] ALD became an important tool for many industrial and research applications.[257, 259] An ALD is performed by exposing the substrate to sequential alternating pulses of gaseous chemical precursors that react with the substrate. These gas-surface reactions are called “half-reactions” and take place in a chamber under vacuum (<1 Torr) for a certain amount of time to allow the precursor to fully react with the whole substrate surface through a self-limited process that leaves only a monolayer at the surface. Subsequently, the chamber is purged with an inert carrier gas to remove unreacted precursor or reaction by-products. Then the other precursor is pulsed into

the chamber and reacts with the substrate leading to the deposition of another monolayer and after that the chamber is purged again. The process is then cycled until the desired deposited thickness is achieved. The process takes place at temperatures typically <623 K.[259]

Several inorganic materials, such as oxides, nitrides, sulphides, selenides, tellurides, and pure elements can be deposited by ALD.[259, 260] The oxides have been the most investigated materials and the deposition of Al_2O_3 using trimethylaluminum and water is a well-studied example of ALD.[128, 257, 260, 261] The surface chemistry during the ALD of Al_2O_3 using trimethylaluminum and water can be described as[128, 257, 261]

(A) $AlOH^* + Al(CH_3)_3 \rightarrow AlOAl(CH_3)_2^* + CH_4$

(B) $AlCH_3^* + H_2O \rightarrow AlOH^* + CH_4$

where the asterisks denote the surface species. The deposition can be performed at temperatures between 306 and 523 K.[128, 262]

The coating and the infilling of NP systems with metal oxides, as Al_2O_3, or other materials not only provide protection against oxidation but also impacts on other properties of the systems where they are deposited. For example, ALD infilling with Al_2O_3 has been shown to greatly enhance charge carrier mobilities in the case of field-effect transistors made of PbSe quantum dots and ZnO nanocrystals[254, 263] and improved the charge mobility in photodetectors made of CdSe quantum dot films by infiltration of the space between quantum dots with ZnO.[264] The photoluminescence properties are also affected by the coating or infilling of the systems using ALD. Table 5.1 presents some examples in which the photoluminescence properties of the systems were modified by ALD. In some cases de deposition also affected other properties, such as the refractive index.[255]

Table 5.1 Systems where ALD has been performed, with impact on the photoluminescence properties.

System	Material deposited	Distribution of the deposited material	Impact on the properties
CdSe/ZnS core-shell NP films[255]	Al_2O_3	Infilling and overcoating of NP films	Stable photoluminescence emission intensity even after three months of sample storage Refractive index can be tuned to higher values
Bulk Si[265]		Thin layer deposited at the surface	Change in the profile of the emission spectra measured at 10 K
ZnO nanowires and metal NPs[266]		Al_2O_3 layer between the ZnO nanowires and the metal NPs	Enhancement of UV emission that is dependent on the thickness of the Al_2O_3 layer
$NaYF_4$ NPs doped with Yb^{3+}, Er^{3+} or Yb^{3+} in close proximity of Au, Ag or Al NPs[267]		Al_2O_3 layer between the $NaYF_4$ NPs and the metal NPs	Increase of the photoluminescence intensity with dependence on the thickness of the oxide spacer layer and the type of metal NP
Si nanowires[268]	PbS	Uniform coating of the Si nanowire array with a layer of PbS QDs	Photoluminescence intensity increases
Monolayers of CdSe/CdS/ZnS core/shell/shell QDs[269]	ZnO	The QDs are encapsulated in the ZnO matrix	Photoluminescence intensity decreases to half its initial value after encapsulation

In this work, ALD is used to infill Si NP films with Al_2O_3 with the goal of studding if the deposition can provide protections against the spontaneous oxidation in ambient conditions as well as to study if the deposition of metal oxides, as the Al_2O_3, may impact the photoluminescence properties of the Si NPs. Using films of Si NPs with 18 nm in mean diameter that were characterized by SEM, XPS, and SIMS, it was possible to verify that a homogeneous infilling of the films with Al_2O_3 by occupation of the void spaces between the NPs, was achieved. The homogeneous infilling of the films with Al_2O_3 was also studied using FTIR because this is an easy and nondestructive technique. The FTIR was then used to verify the homogeneous infilling of films of Si NPs with average

diameters of 5.5 and 4.9 nm. For these films of NPs, with smaller average diameter, it was possible to measure the emission spectra, allowing to study how the infilling of Al_2O_3 affects the photoluminescence properties. The Al_2O_3 induces a modification on the emission profile but does not suppress the emission. In what concerns the protection against oxidation in ambient conditions, the infilling with Al_2O_3 demonstrated the capability of protecting the films from this phenomenon.

5.2 Results and discussion

5.2.1 Structural characterization before Al_2O_3 deposition

The characterization of the Si NP films before the Al_2O_3 deposition started by measuring the FTIR spectra of films of Si NPs with mean diameter of 18 nm that were air exposed and of films of the same Si NPs after etching with HF solution. The FTIR spectra measured for both systems (Figure 5.1) are modulated due to optical interference effects within the film.[270, 271] The measurement performed for Si NPs that were air exposed (Figure 5.1A) reveals a band within 1000-1200 cm^{-1}, with center around 1100 cm^{-1} attributed to Si-O-Si bond,[59] as expected from the formation of a native oxide shell on the surface of the Si NPs after air exposure. After the etching of the Si NPs with HF solution, the band attributed to Si-O-Si is not observed in the FTIR spectrum (Figure 5.1B), instead it is possible to observe a band within 890-940 cm^{-1}, with center around 915 cm^{-1} associated with deformations modes of $Si-Si-H_3$ and scissor and wag modes of Si_2-Si-H_2[165] and other band within 2050-2150 cm^{-1}, with three components located at 2086, 2100, and 2139 cm^{-1}, attributed to Si-H stretching vibrations of Si_3-Si-H, Si_2-Si-H_2, and $Si-Si-H_3$ surface hydride groups, respectively.[59] Is also possible to observe a small band within 604-700 cm^{-1}, possibly associated with Si-H vibrations.[126] These results indicate that the HF etching removes the oxide shell, rendering H-terminated Si NPs.

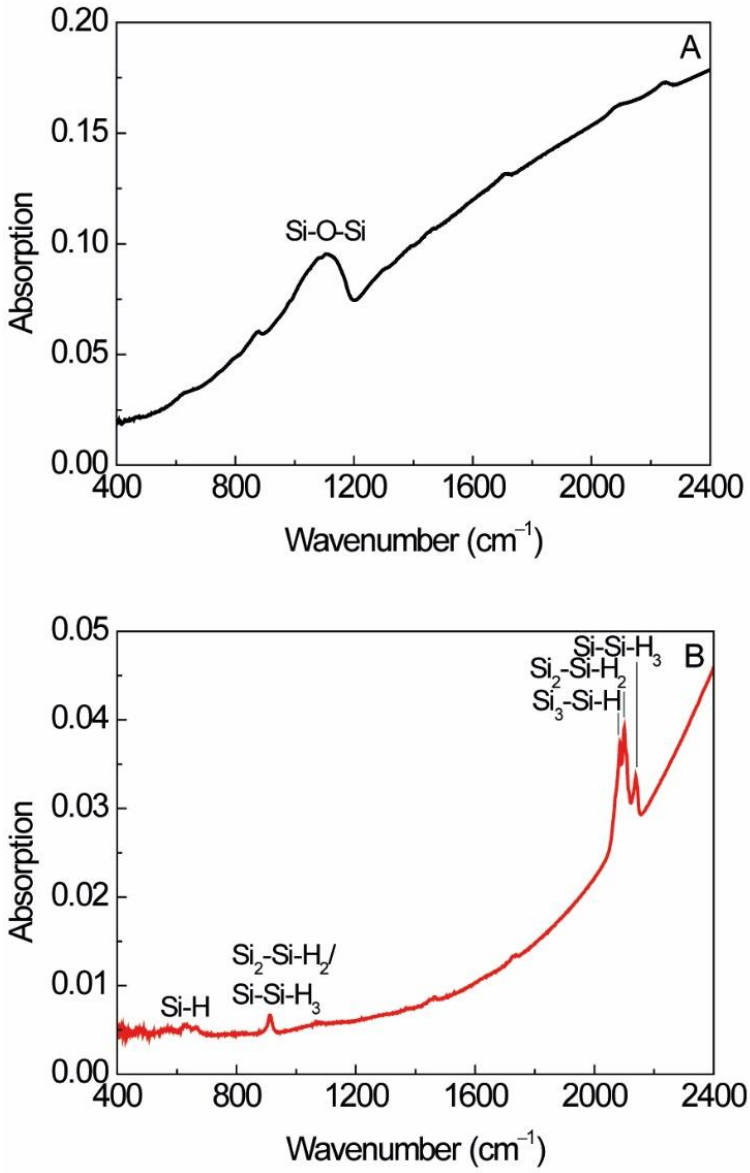

Figure 5.1 FTIR spectra recorded for films of Si NPs with mean diameter of 18 nm prepared with 4 sprays of NPs that were (A) air exposed and that were (B) etched with a HF solution.

Measurements performed using a profiler (Veeco DekTak 150, stylus diameter of 12.5 µm using a step of 0.053 µm) found that the **Si NPs (18 nm)** samples prepared with 4 sprays of NPs present a mean value of thickness of 60 nm and a surface roughness of 95 nm determined from

$$\frac{1}{n}\sum_{i}^{n} y_i \tag{5.1}$$

and

$$\sqrt{\frac{1}{n}\sum_{i=1}^{n} y_i^2} \tag{5.2}$$

respectively,[272] where y_i are the n values measured for the height in the scan direction between 200 and 400 μm (Figure 5.2).

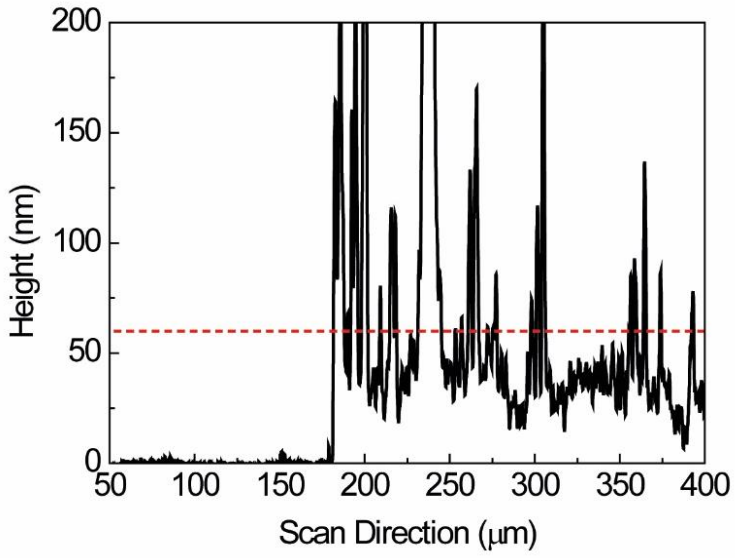

Figure 5.2 Surface profile of a **Si NPs (18 nm)** sample prepared with 4 sprays of NPs.

Films of Si NPs with different thickness were prepared by performing the spray coating deposition with different number of sprays. The modulation due to optical interference effects is observed in the FTIR spectra of Figure 5.3A. The interference phenomenon depends on the thickness of the film.[270, 271] So considering that the thickness of the films depends on the number of sprays, as expected the profile of the spectra that results from the modulation also changes with the number of sprays. The FTIR measurements performed on these films show that the bands associated with the Si_2-Si-H_2/Si-Si-H_3 and Si_{4-X}-Si-H_X (X = 1, 2, 3) increase as the number of sprays used to prepare the films increases (Figure 5.3B). This result was expected, considering that films with larger thicknesses contain more Si NP, and so the signal of the hydrogen-termination should be larger. The spectra also reveal a band at 2920 cm^{-1} due to CH_2/CH_3 deformation modes.[70] The origin of these species should be the organic solvent used in the spray deposition.

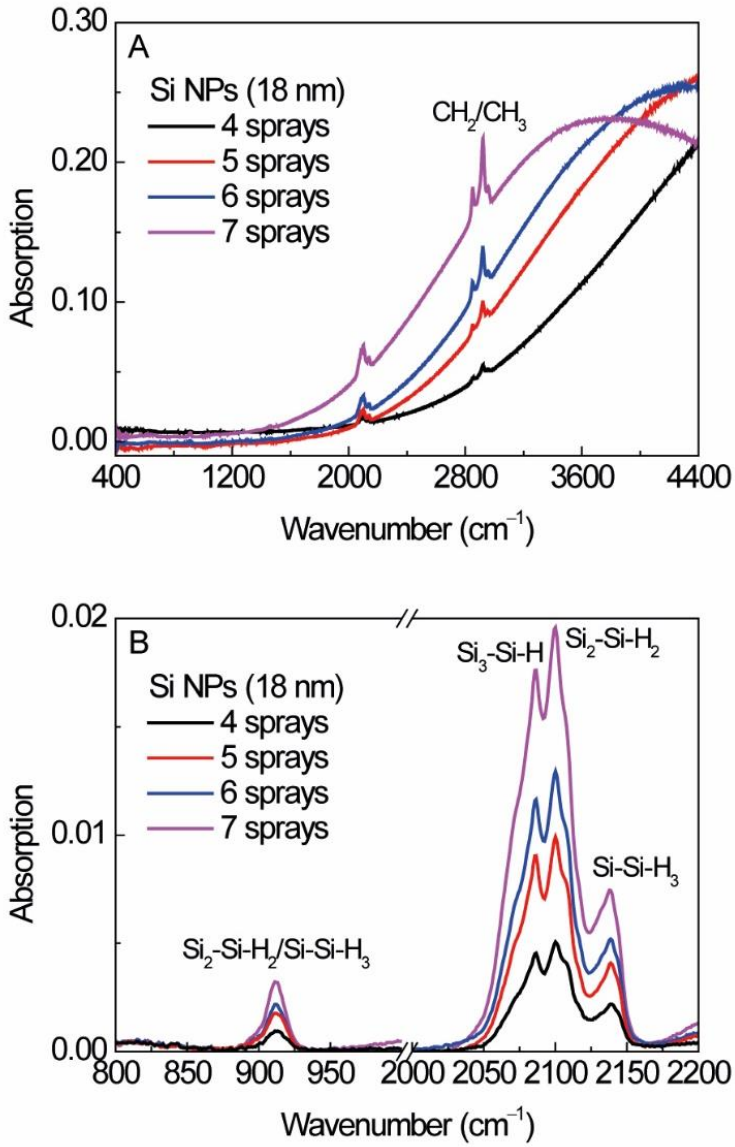

Figure 5.3 A) FTIR spectra recorded for **Si NPs (18 nm)** films prepared with 4, 5, 6 and 7 sprays NPs. **B)** Evolution of the Si_2-Si-H_2/Si-Si-H_3 and Si_{4-X}-Si-H_X related FTIR bands between 800-1000 cm^{-1} and 2000-2200 cm^{-1} spectral regions, respectively, as function of the number of sprays of NPs.

5.2.2 Structural characterization after Al_2O_3 deposition

The SEM performed on films after deposition of Al_2O_3 with 120 ALD cycles, sample **Si NPs (18 nm) + Al_2O_3**, shows a change in the surface morphology when compared with the images of films before the deposition of Al_2O_3, sample **Si NPs (18 nm)**, as shown in Figure 5.4. Before Al_2O_3 deposition of the Al_2O_3 it is possible to identify the NPs in the SEM image but after the Al_2O_3 deposition the structures that can be identified present the same shape with and larger size than the individual NPs that can

be identified before the Al_2O_3 deposition. Considering that the deposition of Al_2O_3 layer on the surface of the NPs will lead to the increase of the NPs size, the SEM images are a good indication of the successful deposition of Al_2O_3.

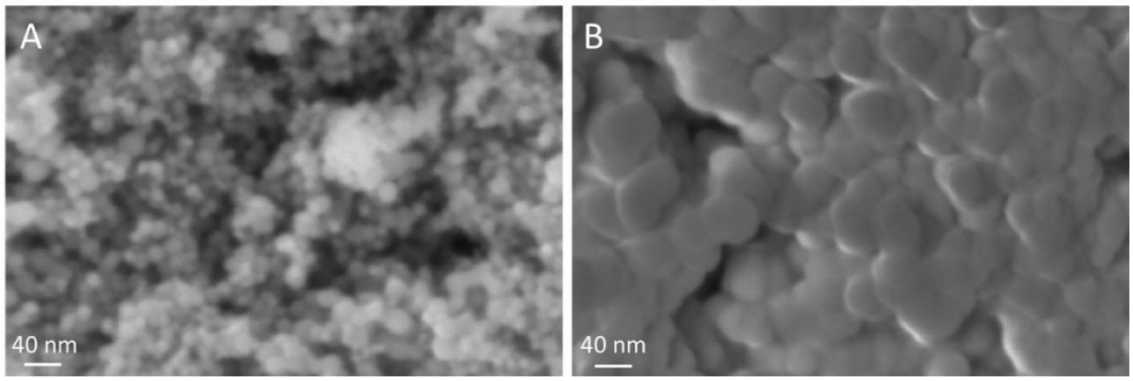

Figure 5.4 SEM images of (A) **Si NPs (18 nm)** and (B) **Si NPs (18 nm) + Al_2O_3** samples prepared with 4 sprays of Si NPs.

The measurements performed by XPS on samples where different number of ALD cycles were performed reveal the presence of the Al 2p, Al 2s and O 1s bands (Figure 5.5),[159, 273] as expected for a well succeeded deposition of Al_2O_3. The films prepared with the lower numbers of ALD cycles (30 and 50 cycles) reveal also the Si 2p and Si 2s bands (Figure 5.5A).

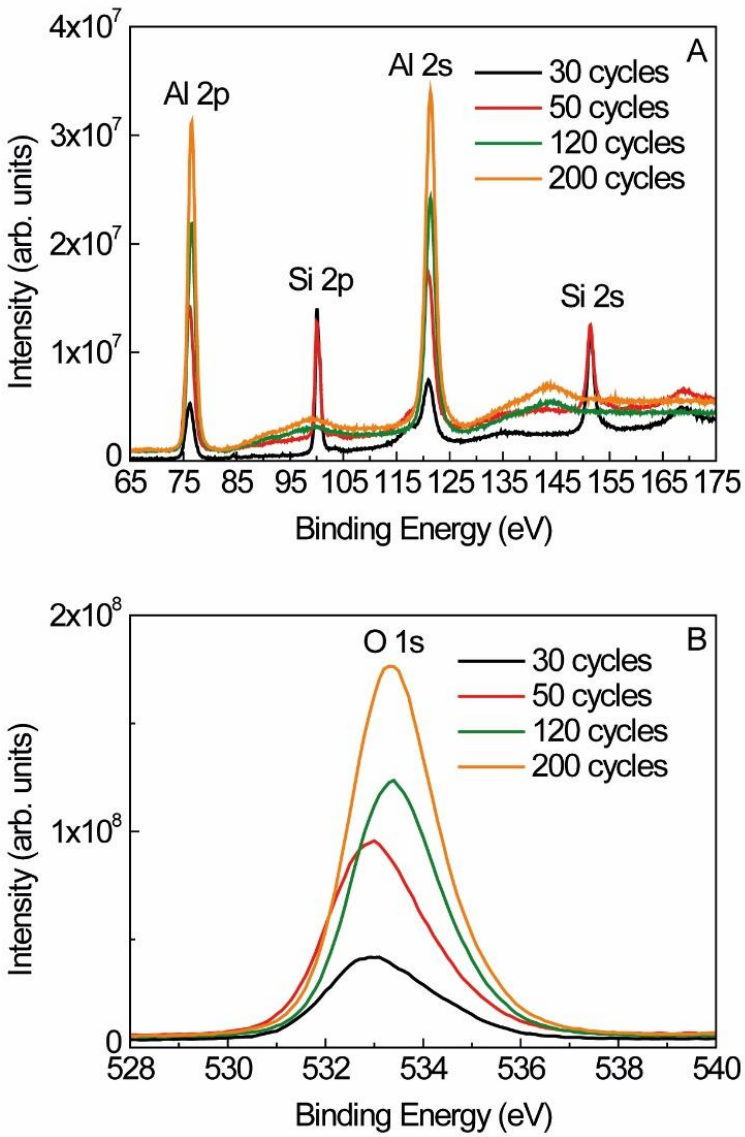

Figure 5.5 XPS spectra in the regions of (A) Al 2p, Si 2p, Al 2s, Si 2s and (B) O 1s peaks recorded for films of **Si NPs (18 nm) + Al_2O_3** samples prepared with different numbers of ALD cycles. The Si NP films were deposited using 4 sprays.

Taking into consideration the thickness of the region that is analyzed by the XPS technique (≈10 nm),[274] the XPS data can give some information about the thickness of the Al_2O_3 that is being deposited. The fact the Si-related bands are observed for the samples prepared with 30 and 50 ALD cycles, indicates that for these samples the thickness of Al_2O_3 at the surface should be lower than 10 nm. Considering that the Al_2O_3 growth rate is 1.0 Å per ALD cycle, the expected thicknesses for 30 and 50 cycles are 3 and 5 nm, respectively, indeed below 10 nm. For samples with 120 and 200 cycles, an Al_2O_3 layer thickness larger than 10 nm is expected, which is in good agreement with the fact that the Si-related XPS signals are not observed for these samples.

The **Si NPs (18 nm) + Al_2O_3** deposited using 120 ALD cycles has also been characterized using SIMS. The SIMS signals of the analyzed elements are presented as a function of the sputtering time in Figure 5.6.

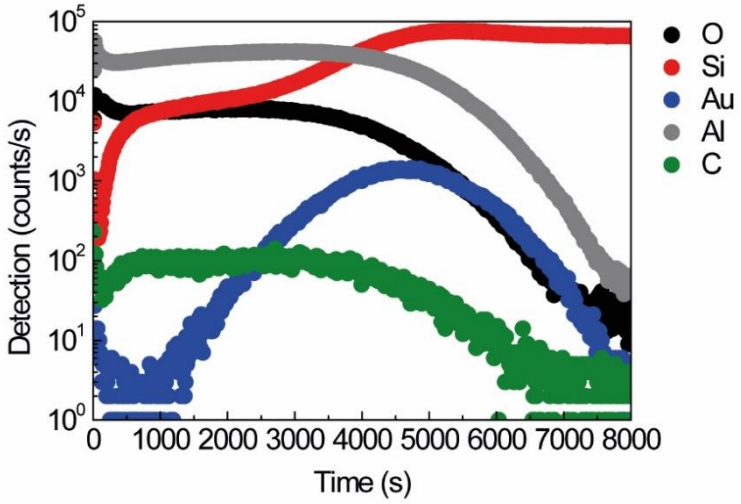

Figure 5.6 SIMS measured for different elements as a function of sputtering time measured for a **Si NPs (18 nm) + Al_2O_3** sample (120 ALD cycles).

The elements chosen to be analyzed were the Si, which is present in the Si NPs and in the substrates, the Au, which is present as a layer between the Si NPs (18 nm) + Al_2O_3 film and the substrates, the O and Al, which are present in the Al_2O_3, and the C, which is present in the solvent used to prepare the Si NP solution used for the spray coating of the Si NP films. As can be seen in Figure 5.6, up to the first 500 s of sputtering, there in a decrease in the O and Al signals while there is an increase in the Si signal. This indicates that for 120 ALD cycles, there is a layer of Al_2O_3 at the surface of the film. This correlates well with the XPS data that also indicate the existence of an Al_2O_3 layer at the surface, as for 120 ALD cycles the signals from Si are not observed in the spectra. The XPS and SIMS measurements, together with the change in the surface morphology, after ALD, shown by the SEM measurements (Figure 5.4), are good evidences of the deposition of an Al_2O_3 layer at the surface of the film. After the 500 s of sputtering, the number of Al and O signals remain approximately constant, while the Au signal increases. This can be readily understood because while the Si NPs (18 nm) + Al_2O_3 layer is removed by the sputtering, the underneath Au layer becomes continuously more exposed. The counts of Au reach a maximum at around 4500 s of sputtering and until this point, the Al and O signals remain approximately constant. This clearly indicates that the Al_2O_3 material is

homogeneously distributed in the Si NPs (18 nm) + Al_2O_3 layer, meaning that was achieved a homogeneous infilling of the empty voids within the Si NPs film by means of the ALD. This conclusion is also corroborated by the variation of the C signal. The C element is present only within the Si NPs film as a residual resulting from the organic solvent used in the spray deposition of the Si NPs. The fact that the signals of the Al, O, and C display a very similar behavior as a function of sputtering time (see Figure 5.6), namely constant counts values in the interval between 500 s and 4500 s and decrease of these values for sputtering times above 4500 s, shows that the Al_2O_3 is homogeneously distributed within the Si NPs layer. The simultaneous decrease of the counts of Al, O, C and Au for sputtering times above 4500 s and observation that at the same time the Si signal remains constant show that for these sputtering times the substrate material has been reached and less and less material from the Si NPs (18 nm) + Al_2O_3 film and Au layer can be observed.

The successful homogeneous infilling of the Si NP films with Al_2O_3 deposited by ALD is also confirmed by FTIR measurements. The FTIR spectra measured for several **Si NPs (18 nm) + Al_2O_3** samples prepared with different numbers of ALD cycles are shown in Figure 5.7A.

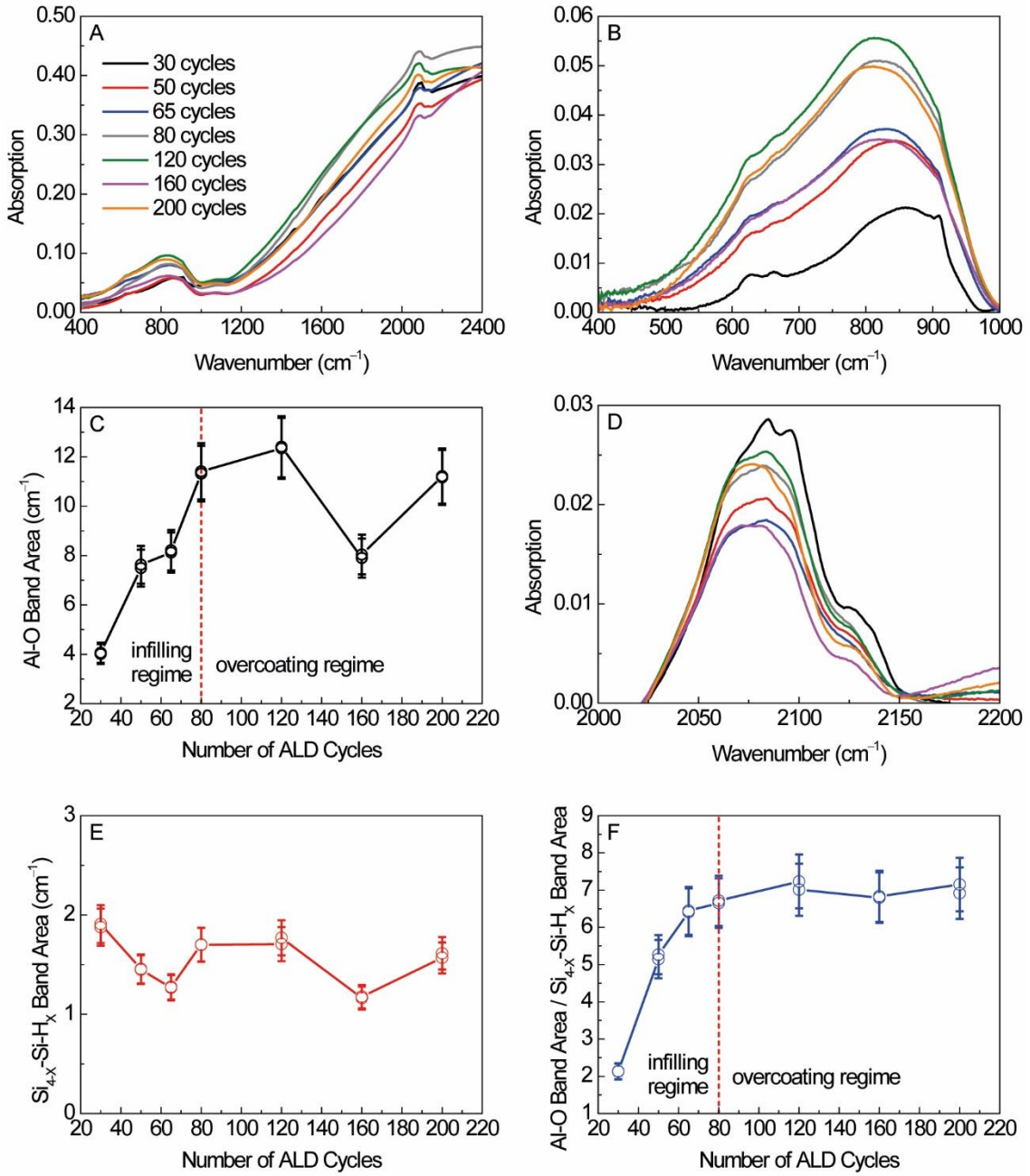

Figure 5.7 A) FTIR spectra recorded for **Si NPs (18 nm) + Al_2O_3** samples prepared with 4 sprays of Si NPs and with different number of ALD cycles. **B)** Evolution of the Al-O band as a function of the number of ALD cycles. **C)** Al-O band area as a function of number of ALD cycles. **D)** Evolution of the Si_{4-X}-Si-H_X band as a function of the number of ALD cycles. **E)** Si_{4-X}-Si-H_X band area as a function of number of ALD cycles. **F)** Al-O band area normalized by the Si_{4-X}-Si-H_X band area as a function of number of ALD cycles.

The Si NP films in these samples were deposited with 4 sprays. The spectra show a band related to Al_2O_3,[275-279] which appears within the 600-1000 cm^{-1} spectral region and is centered at about 800 cm^{-1}, due to stretching of Al-O bonds.[275-278] Figure 5.7B shows the spectra as a function of the number of ALD cycles and Figure 5.7C shows the

evolution of the Al-O FTIR band area obtained by numerical integration of the FTIR band in the interval between 700 and 1000 cm^{-1}. As can be seen, the FTIR signal from Al-O increases rapidly with the number of ALD cycles up to a cycle number of 80, whereas for larger cycle numbers no major increase of the Al_2O_3 signal is observed. This is consistent with the existence of Al_2O_3 infilled in the Si NP film. Hence, during the first cycles, the Al_2O_3 is being infilled into the Si NP film, by being deposited on the surfaces of the Si NPs, leading to the filling the void spaces of the film. This process that leads to the filling of the void spaces is called infilling regime, as denoted in Figure 5.7C. When the film is fully infilled, there are no void spaces and so there is no inner surface available for Al_2O_3 deposition, and therefore the Al_2O_3 is only deposited on the top of the film. When the Al_2O_3 is being deposited only in the top of the films it is said that the deposition is in the overcoating regime (Figure 5.7C). For 160 cycles of ALD the band area is lower than for 120 cycles, this may be due to differences in the amount of NPs deposited in each film. Performing a normalization of the Al-O FTIR band area by the FTIR band related to Si_{4-X}-Si-H_X (Figure 5.7D and 5.7E), to correct for differences in the amount of NPs in each film, confirms the existence an infilling regime with a transition to overcoating regime at around 80 ALD cycles (Figure 5.7F).

Besides the experiment presented above, where the number of ALD cycles was changed and the thickness of the Si NP films was kept approximately constant. Also were performed experiments where the number of ALD cycles was kept constant but the thickness of the films was changed, by using films prepared with different number of sprays. The Figure 5.8A shows FTIR spectra for the corresponding **Si NPs (18 nm) + Al_2O_3** samples prepared with 4, 5, 6 and 7 NP sprays. For these samples, the Al_2O_3 was deposited with 40 ALD cycles in order to be in the NP infilling regime, as discussed above. The spectra reveal the signal from the Al-O bonds stretching,[275-278] within the 600-1000 cm^{-1} spectral region. Also, it is observed a reduction of the signals of the Si_{4-X}-Si-H_X species (2000-2200 cm^{-1} spectral regions), when compared with the **Si NPs (18 nm)** samples (Figure 5.3). This is consistent with the fact that in the first steps of the ALD the hydrogen at the surface of the Si NPs reacts with the reagents from the ALD. Figure 5.8B shows the evolution of the Al_2O_3 FTIR band as a function of the number of sprays and in turn as a function of the amount of Si NPs in the sample. As can be seen, the Al_2O_3 FTIR

band increases with the amount of Si NPs, as is expected for an infilling of the Si NP films with Al_2O_3.

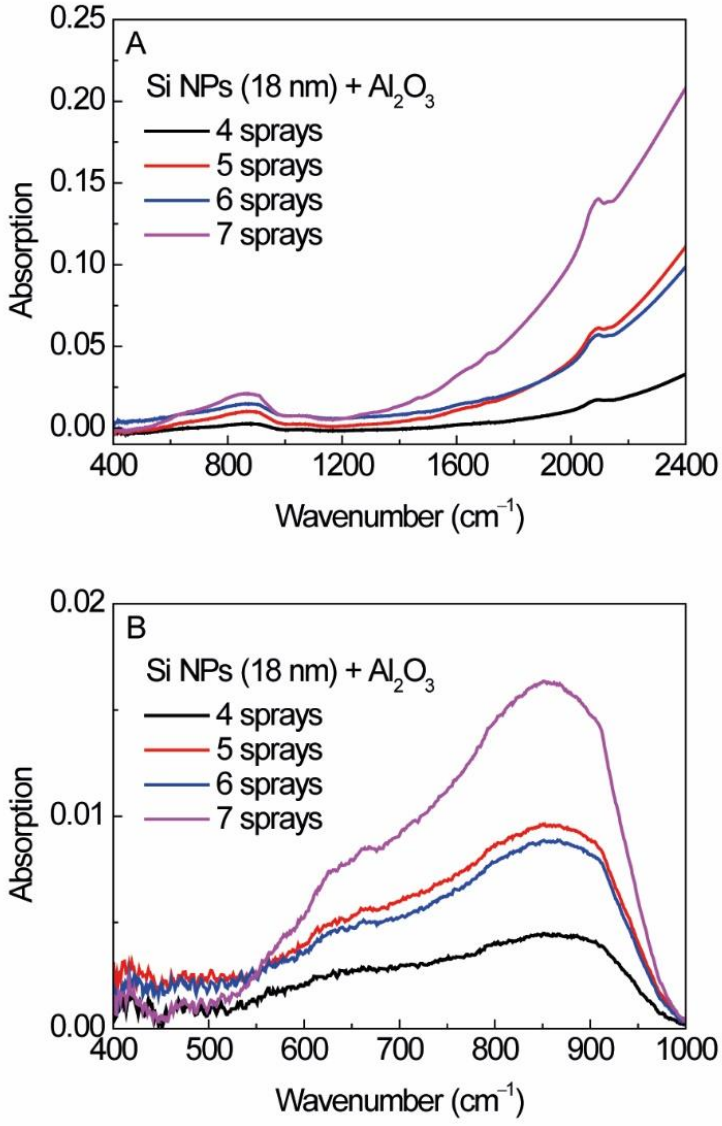

Figure 5.8 A) FTIR spectra recorded for **Si NPs (18 nm) + Al_2O_3** films prepared with 4, 5, 6 and 7 sprays NPs and 40 ALD cycles. **B)** Evolution of the Al-O FTIR band as a function of the number of sprays used to prepare the films.

In order to establish an easy and non-destructive optical method to evaluate the infilling of the Si NP films with Al_2O_3, in the following the FTIR signals from hydrogen-termination of the Si NPs, which quantify the specific surface available for Al_2O_3 deposition within the Si NP film, are correlated with the FTIR signals from Al-O, which quantify the amount of Al_2O_3 material deposited on that surface. The area of the signals associated with the hydrogen-termination is a more accurate indicator of the amount of Si NPs in the film than the number of NP sprays, because any small difference in the

amount of Si NPs deposited in each different spray are removed. Thus, it is shown in Figure 5.9A and 5.9B the Al-O band area as a function of the Si_2-Si-H_2/Si-Si-H_3 and Si_{4-X}-Si-H_X bands areas, respectively. Here, the Si_2-Si-H_2/Si-Si-H_3 and Si_{4-X}-Si-H_X bands area was obtained for several **Si NPs (18 nm)** samples deposited with different numbers of sprays, thus giving different amounts of Si NPs. The Al-O band area was obtained from FTIR spectra recorded for the very same films after Al_2O_3 deposition [**Si NPs (18 nm) + Al_2O_3** samples] using in all cases 40 ALD cycles. As can be seen in Figure 5.9A and 5.9B, the Al-O band area increases linearly with the increase of the signals associated with the hydrogen-termination. In a homogenous infilling, an increase of the inner surface available for Al_2O_3 deposition, *e.g.* by increase of the amount of NPs in the films, should correspond to a linearly proportional increase of the amount of Al_2O_3 material deposited. The linear dependence between the band area of the signal associated with the hydrogen-termination and the signal associated with the Al_2O_3, together with an intercept close to 0 cm^{-1}, which means that for zero Si-H surface there is no Al_2O_3 deposited, provides evidence for a homogeneous infilling of the Si NP films with Al_2O_3.

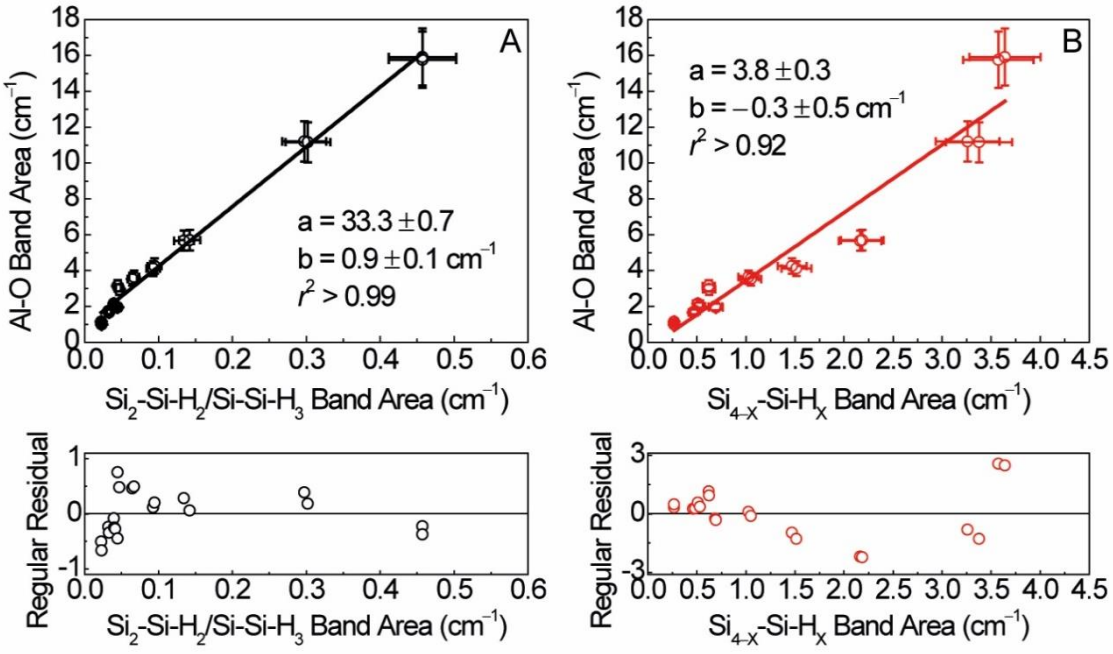

Figure 5.9 Al-O band area a function of the (A) Si_2-Si-H_2/Si-Si-H_3 band area and (B) Si_{4-X}-Si-H_X band area. The lines correspond to the data fit with a linear function with slope (a), intercept (b), and r^2 are indicated in the graphs. Fit regular residual plots (bottom).

This optical method was applied to evaluate the infilling of the Si NPs films made of smaller NPs, namely **Si NPs (5.5 nm)** and **Si NPs (4.9 nm)** samples. Here Si NP films

with different amounts of NPs were prepared, enabled by different numbers of spray coatings, and the FTIR spectra before and after Al_2O_3 (40 ALD cycles) were measured. The FTIR bands of **Si NPs (5.5 nm)** and **Si NPs (5.5 nm) + Al_2O_3** associated with Si_{4-x}-Si-H_x and Al-O signals, respectively, are shown in Figure 5.10.

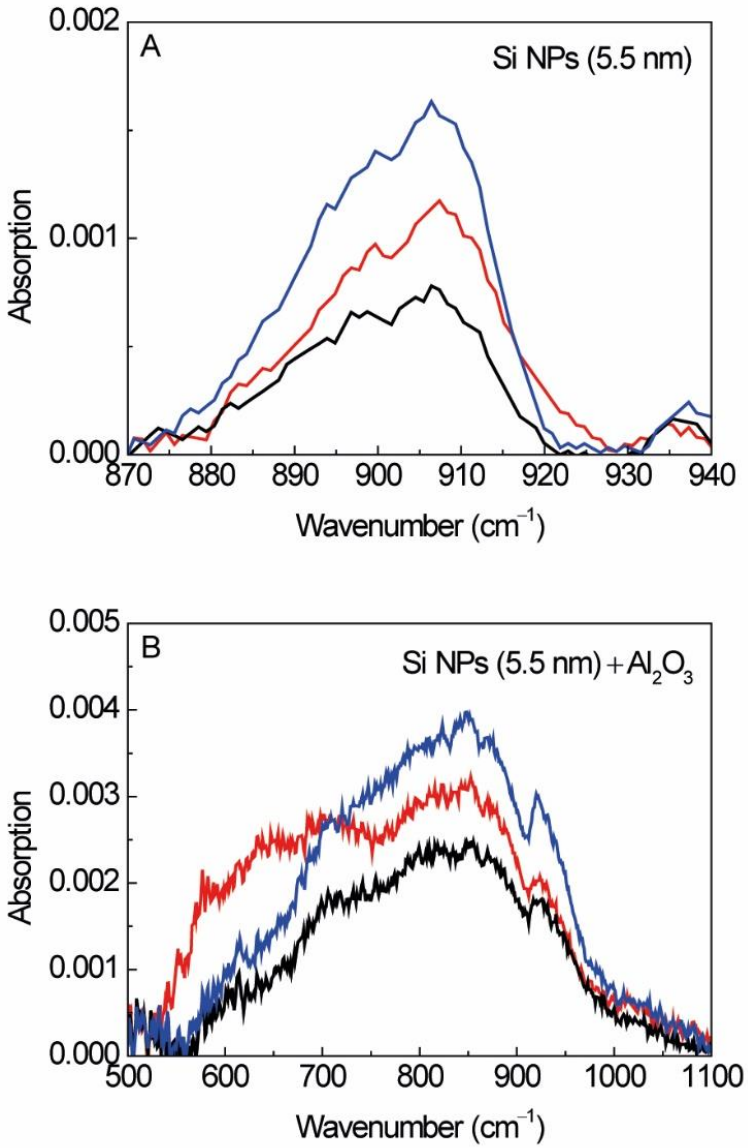

Figure 5.10 (A) Si_{4-x}-Si-H_x and (B) Al-O FTIR bands for **Si NPs (5.5 nm)** and **Si NPs (5.5 nm) + Al_2O_3**, respectively, deposited with different numbers of sprays.

Figure 5.11A and 5.12B show the Al-O band areas as a function of the Si_2-Si-H_2/Si-Si-H_3 bands areas for films made of Si NPs with *d*=5.5 nm and *d*=4.9 nm, respectively. As can be seen, also for these cases the Al-O signal correlates linearly with the Si_2-Si-H_2/Si-Si-H_3 band area, with an intercept close to 0 cm^{-1}. This relation had been already observed above for films made of Si NPs with *d*=18 nm and indicates that for films made

of Si NPs with a smaller diameter the ALD also allows a homogeneous infilling of the Si NPs films with Al_2O_3.

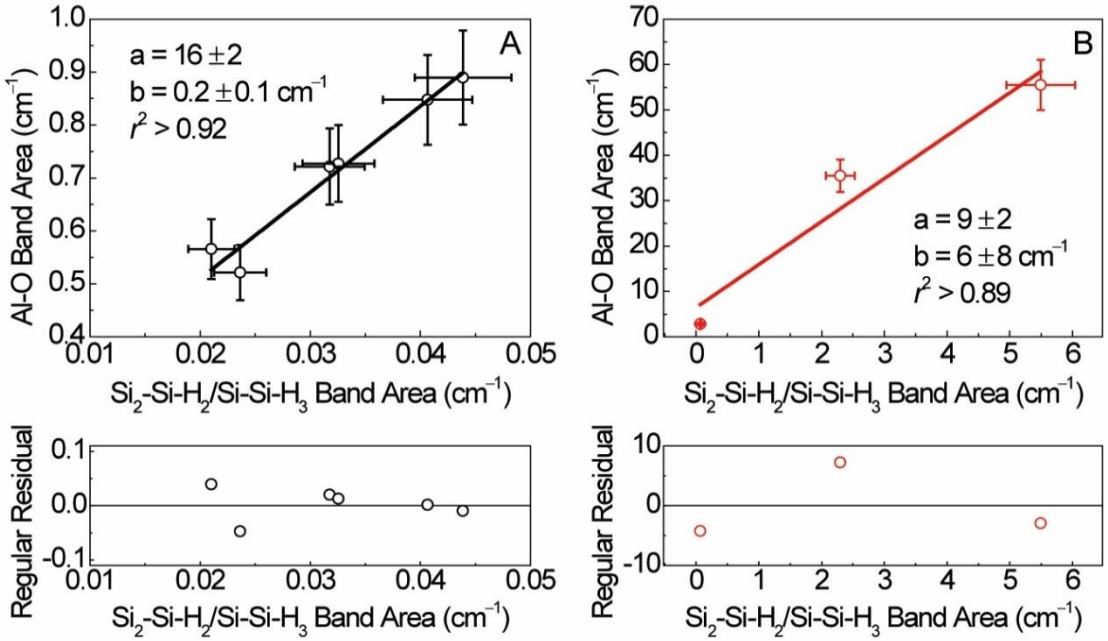

Figure 5.11 Al-O band area a function of the Si_2-Si-H_2/Si-Si-H_3 band area for (A) **Si NPs (5.5 nm) + Al_2O_3** and (B) **Si NPs (4.9 nm) + Al_2O_3** samples. The lines correspond to the data fit with a linear function with a, b, r^2 are indicated in the graphics. Fit regular residual plots (bottom).

5.2.3 Impact of the Al_2O_3 deposition on the oxidation process

The impact of the Al_2O_3 deposition on the oxidation process was studied by exposing **Si NPs (18 nm)** and **Si NPs (18 nm) + Al_2O_3** samples to ambient conditions and measuring the FTIR spectra along the process. The FTIR spectra measured for 0.1 and 532 hours of exposure to ambient conditions are shown in Figure 5.12A and 5.12B.

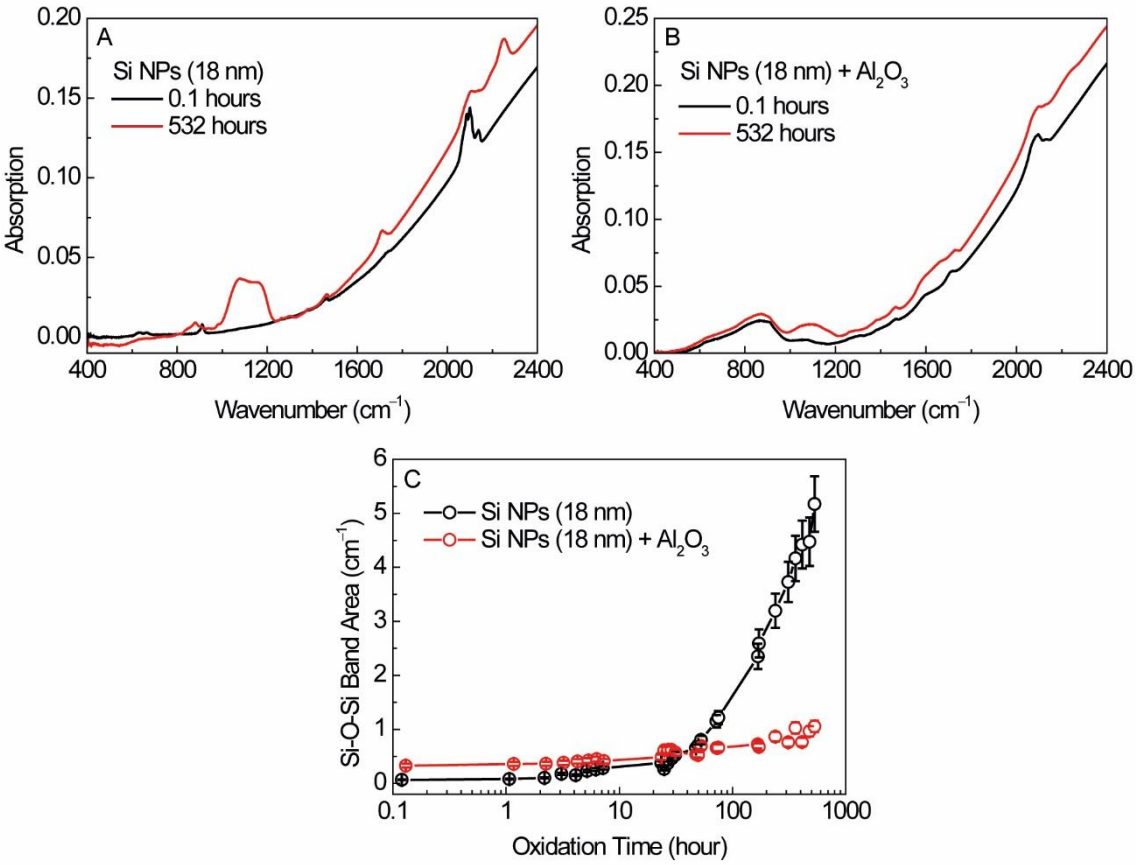

Figure 5.12 FTIR spectra recorded for (A) **Si NPs (18 nm)** and (B) **Si NPs (18 nm) + Al_2O_3** samples prepared with 4 sprays of NPs, for oxidation times of 0.1 and 532 hours. **C)** Si-O-Si band area as a function of the oxidation time.

Immediately before air exposure, the spectrum of **Si NPs (18 nm)** shows the bands within 890-940 cm^{-1} and within 2050-2150 cm^{-1} associated with the H-termination.[59, 165] In the spectrum of **Si NPs (18 nm) + Al_2O_3** measured before exposure to ambient conditions, it is possible to observe the band within 600-1000 cm^{-1} that results from the Al_2O_3 deposition. The band within 2050-2150 cm^{-1} associated with the hydrogen-termination is smaller when compared to that measured for **Si NPs (18 nm)**, because in the first steps of the ALD the hydrogen at the surface of the Si NPs reacts with the reagents from the ALD. Concerning traces of oxidation, only in **Si NPs (18 nm) + Al_2O_3** it is possible to observe a small signal from the band within 1000-1200 cm^{-1}, attributed to Si-O-Si bond.[59] This small trace of oxidation is probably due to the reaction in the first steps of the ALD of the O_2 present in residual amounts inside the ALD system with the water molecules used as reagent. After exposure to ambient conditions for 532 hours, it is possible to observe the Si-O-Si signal in both films. The Si-O-Si band area as function of the oxidation time is shown in Figure 5.12C. It is possible to observe that for **Si NPs**

(18 nm), the Si-O-Si increases fast after approximately 40 hours of exposure to ambient conditions, while for **Si NPs (18 nm) + Al_2O_3** the Si-O-Si signal only slightly increases even after 532 hours of exposure to ambient conditions. This result is in good agreement with reported data,[253, 254] for films of PbSe nanocrystal where the infilling and overcoat with Al_2O_3 deposited by ALD showed to protect against oxidation.

5.2.4 Impact of the Al_2O_3 deposition on the photoluminescence properties

The emission spectra of **Si NPs (*d* nm)** samples with *d* of 4.9 and 5.5 are shown in Figure 5.13A. The emission measured for each sample with both detectors coincides in the energy range between 1.10 and 1.35 eV where the operation range of both detectors overlap. For **Si NPs (18 nm)** no emission has been observed in the whole analyzed energy range. For **Si NPs (4.9 nm)** and **Si NPs (5.5 nm)**, samples deposited with 6 and 4 sprays, respectively, a broad emission is observed between 0.7 and 1.75 eV. It is evident from the shape of the emission spectra for both Si NPs (5.5 nm) and Si NPs (4.9 nm) that the spectra reveal more than one component. One component at lower energy, with energy peak around 1.0 and 1.2 eV for the **Si NPs (5.5 nm)** and **Si NPs (4.9 nm)**, respectively, and another component at higher energy. For the **Si NPs (4.9 nm)** this component at higher energy is around 1.7 eV. For the **Si NPs (5.5 nm)** sample, the spectrum for energies above 1.4 eV has a low signal-to-noise ratio, which hinders the determination of the peak position of the higher energy emission component. Nonetheless, the presence of this component is clear.

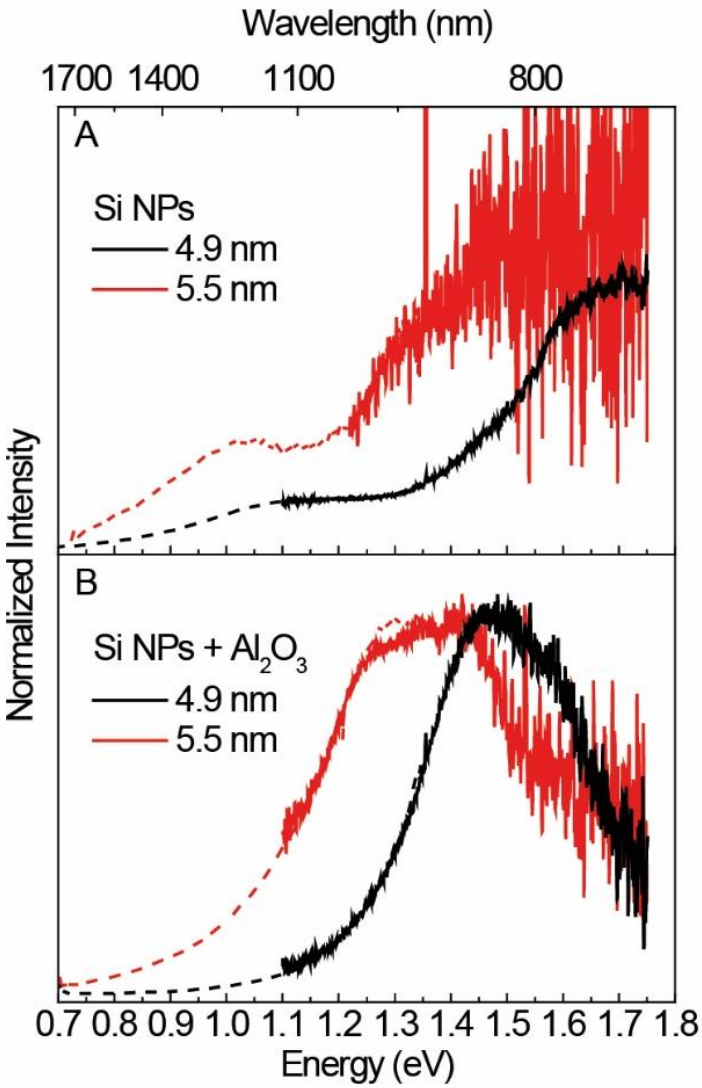

Figure 5.13 Emission spectra recorded for (A) **Si NPs (*d* nm)** and (B) **Si NPs (*d* nm) + Al_2O_3**, *d*=4.9 and 5.5. The excitation power density was 14 mW/cm^2. The spectra were measured with an InGaAs detector (dashed lines) and a Si detector (solid lines).

To study how the deposition of Al_2O_3 affects the emission features of Si NP films, the emission spectra of corresponding **Si NPs (*d* nm) + Al_2O_3** samples with *d* of 4.9 and 5.5 nm have also been recorded (Figure 5.13B). For **Si NPs (18 nm) + Al_2O_3** no emission has been observed in the whole analyzed energy range. The samples **Si NPs (4.9 nm) + Al_2O_3** and **Si NPs (5.5 nm) + Al_2O_3** exhibit an emission in the studied energy range. The emission spectra of these samples are formed by a broad band that is well described by a single-Gaussian function with peak at 1.50±0.01 and 1.36±0.02 eV, respectively. In the case of the **Si NPs (4.9 nm) + Al_2O_3**, the position of the emission band does not correspond to the position of any of the emission components observed for the Si NP films with the same NP average size but without Al_2O_3 deposition.

The spectra of **Si NPs (5.5 nm)**, **Si NPs (4.9 nm)**, **Si NPs (5.5 nm) + Al_2O_3** and **Si NPs (4.9 nm) + Al_2O_3** were measured as a function of excitation power density. Figures 5.14A and 5.14B show the emission spectra of samples **Si NPs (4.9 nm)** and **Si NPs (4.9 nm) + Al_2O_3**, respectively.

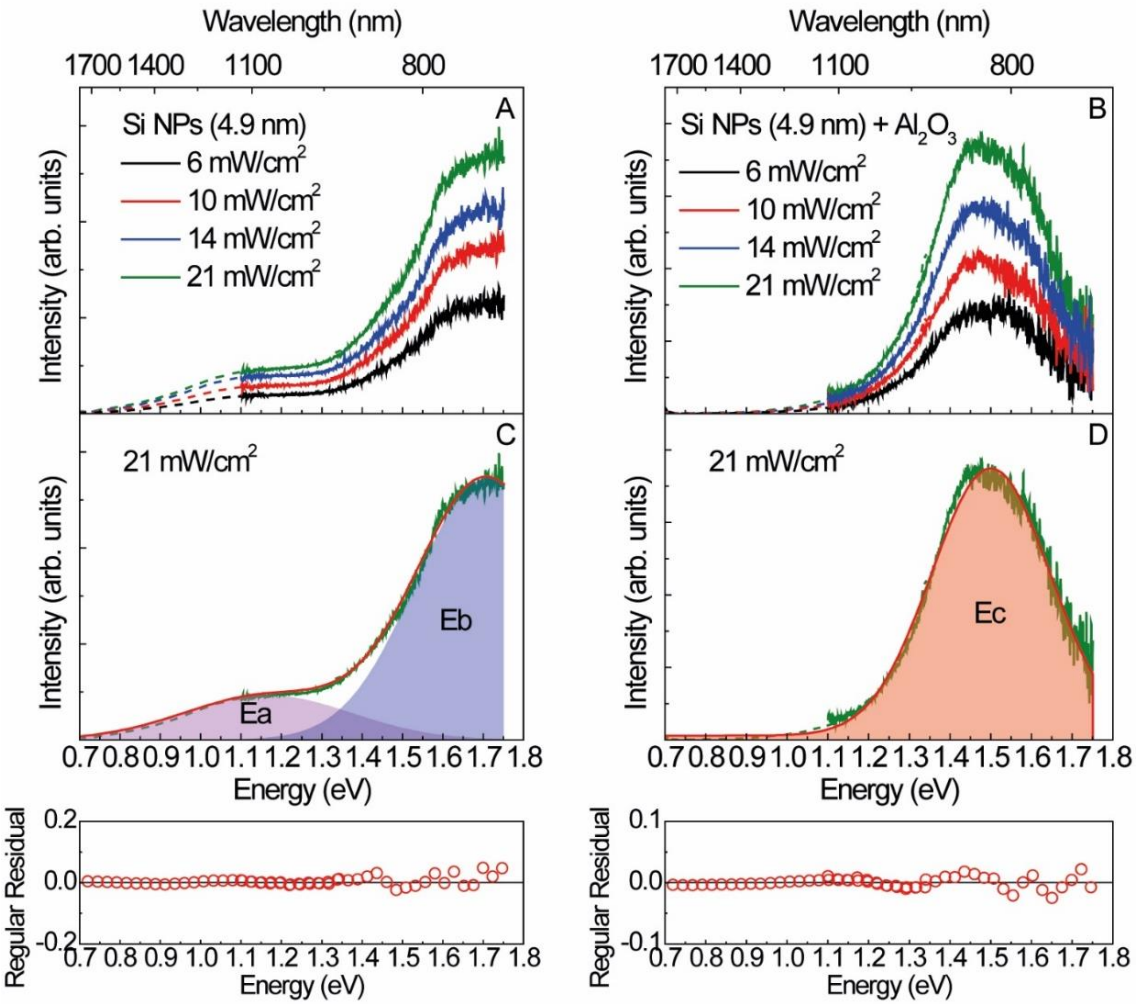

Figure 5.14 Emission spectra recorded with different excitation power densities for (A) **Si NPs (4.9 nm)** and (B) **Si NPs (4.9 nm) + Al_2O_3**. The spectra were measured with an InGaAs detector (dashed lines) and a Si detector (solid lines). (C) and (D) show fits of two and one Gaussian function to the spectra of **Si NPs (4.9 nm)** and **Si NPs (4.9 nm) + Al_2O_3**, respectively. Fit regular residual plot (bottom).

The intensity of the spectra increases as the excitation power density increases, while the shape of the spectra remains unchanged. To quantify the dependence on the excitation power density (P_{exc}) of the emission intensity, Gaussian functions were fitted to the spectra. The spectra of **Si NPs (4.9 nm)** and **Si NPs (5.5 nm)** are well described with a sum of two Gaussian functions denoted Ea and Eb (see example in Figure 5.14C)

and the spectra of **Si NPs (4.9 nm) + Al_2O_3** and **Si NPs (5.5 nm) + Al_2O_3** are well described with a single Gaussian function, denoted Ec (see example in Figure 5.14D).

The dependence of the intensity of the components of the emission spectra (I_{em}) as a function of the excitation power density is presented in Figure 5.15.

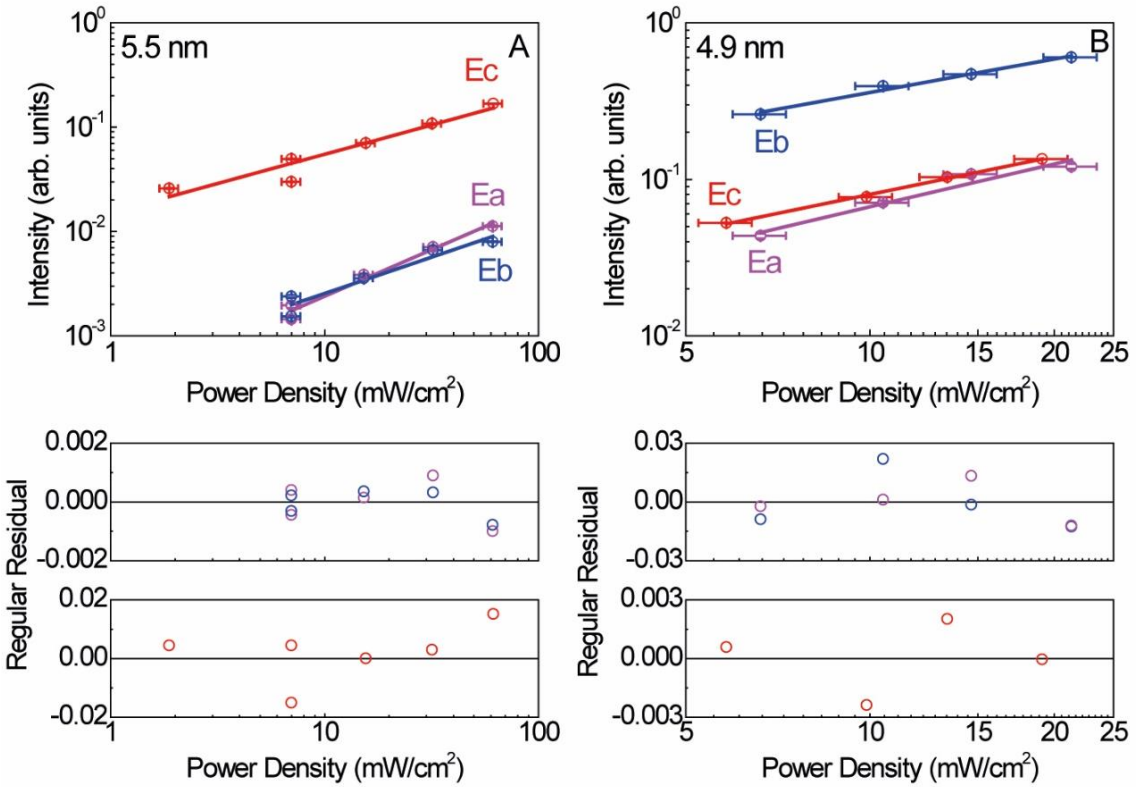

Figure 5.15 I_{em} as function of P_{exc} for films of Si NPs with average diameter of (A) 5.5 and (B) 4.9 nm. The lines correspond to the fit of $I_{em} \sim {P_{exc}}^{k}$, with k indicated in Table 5.2, to the data. Fit regular residual plot (bottom).

For all components, the intensity is proportional to the excitation power density following a power law $I_{em} \sim {P_{exc}}^{k}$,[134] with k values indicated in Table 5.2. For all emission components the k value is lower than 1.

Table 5.2 Values of k determined from the fits to I_{em} as a function of P_{exc} with $I_{em} \sim {P_{exc}}^{k}$, for films of Si NPs with the indicated average diameter (*d*).

Sample	*d* (nm)	Emission component	k
Si NPs (4.9 nm)	4.9	Ea	0.9±0.1
		Eb	0.7±0.1
Si NPs (4.9 nm) + Al_2O_3		Ec	0.8±0.1
Si NPs (5.5 nm)	5.5	Ea	0.9±0.1
		Eb	0.7±0.1
Si NPs (5.5 nm) + Al_2O_3		Ec	0.6±0.1

In the literature, it is reported a that a k value between 0 and 1 corresponds to a free-to-bound radiative recombination, such as free hole and neutral donor recombination, free electron and neutral acceptor recombination or donor-acceptor pair recombination.[134-136] In the case of **Si NPs (5.5 nm)** the peak energy of the Ea emission component is clearly lower than the band gap of Si, which supports the idea that these emission components is due to donor-acceptor type emission of states within the energy band gap of the Si NPs, rather than exciton type emission. Defects as impurities or dangling bonds, resulting, for example, from the synthesis of the NPs, which may be in the Si core or in the surface of the NPs, may be the origin of the observed emission. Other possible origin for the emission is an amorphous shell of distorted Si-Si bonds that is formed in the NPs surface around the crystalline core of the Si NPs. The Raman spectrum of **Si NPs (4.9 nm)** shows evidences of the presence of this amorphous phase (Figure 5.16). The Raman spectrum is well described by a sum of one Lorentzian function centered at 520 cm^{-1}, assigned to the transversal-longitudinal optical phonon mode of crystalline Si and three broad Gaussian lines at 334, 450, and 494 cm^{-1} assigned to disorder-activated (amorphous) longitudinal acoustic modes, transversal optical modes and longitudinal optical modes, respectively.[280, 281] The crystalline fraction (f_c) of Si can be calculated from

$$f_c = \frac{I_c}{I_c + \gamma I_a} \tag{5.3}$$

where I_c and I_a are the intensity of modes associate with crystalline and amorphous phases, respectively and γ=0.1 is a factor that for accounts the higher scattering cross-section of the amorphous phase when compared with the crystalline one.[280, 281] From this equation a crystalline fraction of 77% is obtained.

The fact that the deposition of Al_2O_3 at the surface of the NPs affects the profile of the emission may be the indication of the existence of defects in the surface of the NPs that are passivated as result of the Al_2O_3 deposition. This suggestion is in agreement with the reports of the remotion of defects (OH traps), due to the deposition of Al_2O_3 using ALD that was already reported for ZnO nanocrystals.[263]

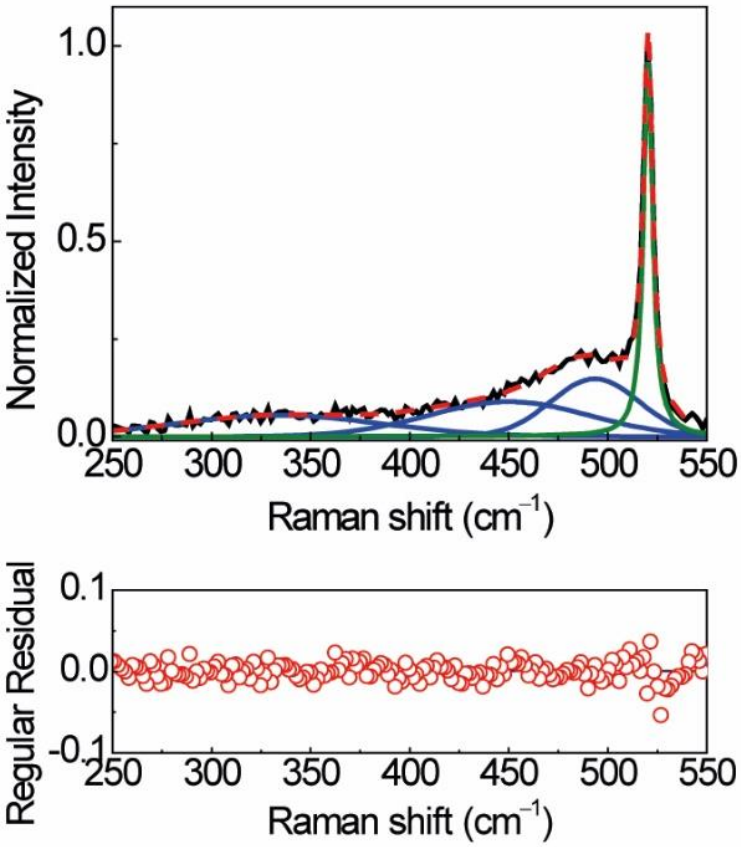

Figure 5.16 Raman spectrum (black line) of **Si NPs (4.9 nm)** and envelope fit (red line) of three Gaussian functions (blue lines) and one Lorentzian function (green line). Fit regular residual plot (bottom).

5.3 Conclusions

The ALD resulted in the homogeneous infilling of Al_2O_3 within films of hydrogen-terminated Si NPs. For Si NPs with average mean diameter of 18 nm, the characterization of the films and the verification of the infilling with Al_2O_3 was performed using SEM, XPS and SIMS. A method that uses FTIR to take conclusions about the infilling of the films with Al_2O_3 was also proposed. The FTIR method allowed an easy and nondestructive way to verify the infilling of film of Si NPs with average mean diameters of 4.9 and 5.5 nm which exhibited emission in the near infrared at 8 K. The photoluminescence properties are modified by the Al_2O_3 infilling. The profile of the emission spectra, which before the ALD is well described by a sum of the Gaussians, after Al_2O_3 infilling is modified, being well described by a single Gaussian. Measurements of the emission spectra as a function of excitation power density indicate that the emission may be related with defects that are partially eliminated by the Al_2O_3 deposition. The exposure of films of hydrogen-

terminated Si NPs and of films infilled with Al_2O_3 reveal that the infilling is capable of protecting the films from the oxidation in air at least up to exposures of 532 hours.

Chapter 6. General conclusions and perspectives

The photoluminescent properties of crystalline Si NPs attract much interest due to their potential applications. The understanding of the photoluminescence properties is a fundamental step to improve their photoluminescence properties. The goal of this work was to study the photoluminescence properties of the Si NPs, prepared by nonthermal plasma synthesis. Si NPs with distinct surface terminations, namely hydrogen, silicon oxide, and functionalized with an organic molecule (1-dodecene) were studied.

It was shown, using time-resolved spectroscopy, that the broad emission band of Si NPs with oxidized surface, and an average core diameter of 3.4 nm, is formed by two emission components, one due to recombination of photogenerated electrons and holes located in the crystalline Si core and another originated from donor-acceptor recombination pair involving states associated with the native oxide shell. After removing of the oxide shell, only the emission component due to the recombination of photogenerated electrons and holes located in the crystalline Si core is observed in the spectrum of the hydrogen-terminated. The maximum value of emission quantum yield measured for oxidized surface Si NPs (0.115 ± 0.011) decreases after removing the oxide shell (to a value below 0.01), but increases to 0.43 ± 0.04 after suspending the oxidized surface Si NPs in ethanol. This is due to the fact the light emission properties of Si NP ensembles are not determined solely by the properties of individual NPs but are also governed by inter-NP charge transfer. The presence of the natural oxide shell hinders inter-NP charge transfer, resulting in a higher quantum yield than in hydrogen-terminated Si NPs. The reduction of inter-NP charge transfer also accounts for the high quantum yields observed for oxidized surface Si NPs when the average inter-nanocrystal separation is increased by suspending the Si NPs in solution.

The study of organic-functionalized Si NPs allowed to study how the surface termination determines intra- and inter-NP interactions and how are the optical properties affected by these interactions. Si NPs functionalized with 1-dodecene without native oxide shell, hydrogen-terminated Si NPs (both with average core diameter of 2.4 nm), and Si NPs functionalized with 1-dodecene and with native oxide

shell (with Si core with average diameter of 1.7 nm) were studied. The hydrogen-terminated Si NPs and the Si NPs functionalized with 1-dodecene without native oxide shell present a single emission band ascribed to recombination of photogenerated excitons in the crystalline Si core of the Si NPs, but at higher energy than the emission of the Si NPs with average core diameter of 3.4 nm, due to the increase of the quantum confinement that leads to the increase of the band gap. The Si NPs functionalized with 1-dodecene without native oxide shell and hydrogen-terminated Si NPs reveal differences in the nonradiative recombination mechanisms associated with inter-NP exciton migrations, that lead to a higher excitonic lifetime value and a higher emission quantum yield (0.23 ± 0.02) measured for Si NPs functionalized with 1-dodecene without native oxide shell. As observed for oxidized surface Si NPs, the Si NPs functionalized with 1-dodecene with native oxide shell present an additional emission component associated with recombination via electronic states of the oxide (surface/interface states), demonstrating that part of the excitons generated in the Si NPs are transferred to oxide-related states. For the Si NPs functionalized with 1-dodecene the grown of an oxide shell does not impose a significant additional barrier for exciton transfer when compared to the barrier provided by the organic termination, as no significant quantum yield variation is observed. The work unveils the leading role played by inter- and intra-NP exciton migration processes for the light emission properties of Si NPs. The study points out that the higher quantum yields generally found for organic-terminated Si NPs result from inhibition of inter-NP exciton transfer (responsible for nonradiative recombination).

Taking advantage of the knowledge obtained from the study that allowed to identify the number and origin of the emission components of the Si NPs, the dependence on the temperature of the emission component ascribed to recombination of photogenerated excitons in the crystalline Si core of the Si NPs was studied as a tool to measure the temperature. The study about the performance of the Si NPs as luminescent thermometer was performed for Si NPs functionalized with 1-dodecene in film and in colloidal solution. The emission peak position can be used as the thermometric parameter, being predicted by Varshni's law. It was experimentally demonstrated that the Si NPs can be used as luminescent thermometer, in the 13-480 K temperature range, and in several medium (air, vacuum, nitrogen atmosphere). The

reversibility and repeatability is higher than 99.98 %, and the maximum relative thermal sensitivity is 0.04 %.K^{-1}. The calibration curve is predicted by Varshni's law making this one of the few primary thermometers reported in the literature and the first with operation experimentally tested in several medium. The fact that the thermometric parameter is predicted by a well-established equation resolve some concerns regarding the robustness of the nanothermometer and the need for calibration in each new measurement environment and allows to state that the thermometric parameters measured are without doubt being dependent on the temperature and not from other variable of the medium. Future works can develop other primary thermometers using other semiconductor NP systems in which the relation between the thermometric parameter and the temperature is also described by Varshni's law.

Aiming to confer protection against oxidation in ambient condition the infilling of hydrogen-terminated terminated Si NPs with Al_2O_3 using ALD was studied, together with the effect on the photoluminescent properties. The homogeneous infilling of Al_2O_3 on films of Si NPs with average mean diameter of 18 nm was shown using techniques as SEM, XPS, and SIMS, but also using a FTIR based method that is easier and nondestructive. This method was applied to verify the homogeneous infilling of films with a smaller average diameter (4.9 and 5.5 nm) in which the emission spectrum in the near infrared at 8 K was possible to measure. The profile of the emission spectra is modified by the Al_2O_3 deposition. The emission profile formed by two components before Al_2O_3 deposition, becomes formed by only one component after the deposition. Measurements of the emission spectra as a function of excitation power density indicate that the emission may be related with defects that are partially eliminated by the Al_2O_3 deposition. Despite the change in the emission profile, the photoluminescence is not completely suppressed, which is a promising result considering the deposition of Al_2O_3 reveled the capability to protect the films against oxidation under ambient conditions. This indicates that the Al_2O_3 deposition may be used to produce Si NP systems with stable photoluminescent properties under ambient conditions.

The objectives behind this thesis were achieved. As future work, it would be relevant a study of the infilling of films of Si NPs with emission properties that would allow to perform photoluminescent measurements not only at low temperature but also at room temperature and in time-resolved mode, these would allow to understand

better how the interaction of the Si NPs with the Al_2O_3 affects the emission. Also, would be interesting study the effect on the photoluminescent properties of the infilling of the films with other metal oxide than can be deposited by ALD (for example ZnO).

References

[1] M. M. Waldrop, *Nature* **2016**, *530*, 145.

[2] M. Schulz, *Nature* **1999**, *399*, 729.

[3] C. Kittel, *Introduction to Solid State Physics*, Wiley, Hoboken **2005**.

[4] L. T. Canham, *Appl. Phys. Lett.* **1990**, *57*, 1046.

[5] R. Teki, M. K. Datta, R. Krishman, T. C. Parker, T.-M. Lu, P. N. Kumt, N. Koratkar, *Small* **2009**, *5*, 2236.

[6] S.-K. Kang, G. Park, K. Kim, S.-W. Hwang, H. Cheng, J. Shin, S. Chung, M. Kim, L. Yin, J. C. Lee, K.-M. Lee, J. A. Rogers, *ACS Appl. Mater. Interfaces* **2015**, *7*, 9297.

[7] M. K. Choi, J. Yang, T. Hyeon, D.-H. Kim, *npj Flexible Electronics* **2018**, *2*, 10.

[8] N. O'Farrell, A. Houlton, B. R. Horrocks, *Int. J. Nanomed.* **2006**, *1*, 451.

[9] P. Sergio, *Advanced Silicon Materials for Photovoltaic Applications*, Wiley, **2012**.

[10] *Terminology for Nanomaterials*, British Standards Institution (BSI), London **2007**.

[11] S. Adachi, *Optical Properties of Crystalline and Amorphous Semiconductors: Materials and Fundamental Principles*, Springer, **1999**.

[12] A. Bapat, M. Gatti, Y.-P. Ding, S. A. Campbell, U. Kortshagen, *J. Phys. D: Appl. Phys.* **2007**, *40*, 2247.

[13] V. Schmidt, J. V. Wittemann, S. Senz, U. Gösele, *Adv. Mater.* **2009**, *21*, 2681.

[14] R. Körmer, B. Butz, E. Spiecker, W. Peukert, *Cryst. Growth Des.* **2012**, *12*, 1330.

[15] M. Hasan, M. F. Huq, Z. H. Mahmood, *SpringerPlus* **2013**, *2*.

[16] J. Henzie, M. Grünwald, A. Widmer-Cooper, P. L. Geissler, P. Yang, *Nat. Mater.* **2012**, *11*, 131.

[17] K. Kim, *Phys. Rev. B* **1998**, *57*, 13072.

[18] A. V. Hernandez, T. V. Torchynska, A. L. Q. Vazquez, Y. Matsumoto, L. Khomenkova, L. Shcherbina, *J. Phys. Conf. Ser.* **2007**, *61*, 1231.

[19] L. Ferraioli, M. Wang, G. Punker, D. Navarro-Urrios, N. Daldosso, C. Kompocholis, L. Pavesi, *J . Nanomater.* **2007**, *2007*, 43491.

[20] N. B. Nguyen, C. Dufour, S. Petit, *J. Phys.: Condens. Matter* **2008**, *20*, 455209.

[21] S. Kalem, P. Werner, V. Talalaev, M. Becker, O. Arthursson, N. Zakharov, *Nanotechnology* **2010**, *21*, 435701.

[22] Y. Q. Wang, Y. G. Wang, L. Cao, Z. X. Cao, *Appl. Phys. Lett.* **2003**, *83*, 3474.

[23] L. E. Brus, P. F. Szajowski, W. L. Wilson, T. D. Harris, S. Schuppler, P. H. Citrin, *J. Am. Chem. Soc.* **1995**, *117*, 2915.

[24] R. B. Wehrspohn, J. N. Chazalviel, I. Solomon, *Eur. Phys. J. B.* **1999**, *8*, 179.

[25] N. Arad-Vosk, A. Sa'ar, *Nanoscale Res. Lett.* **2014**, *9*, 47.

[26] O. Bisi, S. Ossicini, L. Pavesi, *Surf. Sci. Rep.* **2000**, *38*, 1.

[27] R. B. Wehrspohn, J. N. Chazalviel, F. Ozanam, I. Solomon, *Phys. Rev. Lett.* **1996**, *77*, 1885.

[28] A. G. Cullis, L. T. Canham, P. D. J. Calcott, *J. Appl. Phys.* **1997**, *82*, 909.

[29] L. B. Ma, A. L. Ji, C. Liu, Y. Q. Wang, Z. X. Cao, *J. Vac. Sci. Technol. B* **2004**, *22*, 2654.

[30] E. J. Anglin, L. Cheng, W. R. Freeman, M. J. Sailor, *Adv. Drug Deliv. Rev.* **2008**, *60*, 1266.

[31] X. D. Pi, R. Gresback, R. W. Liptak, S. A. Campbell, U. Kortshagen, *Appl. Phys. Lett.* **2008**, *92*, 123102.

[32] J. P. Proot, C. Delerue, G. Allan, *Appl. Phys. Lett.* **1992**, *61*, 1948.

[33] J. P. Wilcoxon, G. A. Samara, P. N. Provencio, *Phys. Rev. B* **1999**, *60*, 2704.

[34] G. Davies, *Phys. Rep.* **1989**, *176*, 83.

[35] P. D. Milewski, D. J. Lichtenwalner, P. Mehta, A. I. Kingon, *J. Electron. Mater.* **1994**, *23*, 57.

[36] J. D. Holmes, K. J. Ziegler, R. C. Doty, L. E. Pell, K. P. Johnston, B. A. Korgel, *J. Am. Chem. Soc.* **2001**, *123*, 3743.

[37] Z. Kang, Y. Liu, C. H. A. Tsang, D. D. D. Ma, X. Fan, N. Wong, S. Lee, *Adv. Mater.* **2009**, *21*, 661.

[38] A. Gupta, M. T. Swihart, H. Wiggers, *Adv. Funct. Mater.* **2009**, *19*, 696.

[39] G. Ledoux, J. Gong, F. Huisken, O. Guillois, C. Reynaud, *Appl. Phys. Lett.* **2002**, *80*, 4834.

[40] G. Ledoux, O. Guillois, D. Porterat, C. Reynaud, F. Huisken, B. Kohn, V. Paillard, *Phys. Rev. B* **2000**, *62*, 15942.

[41] T. Van Buuren, L. Dinh, L. Chase, W. Siekhaus, L. Terminello, *Phys. Rev. Lett.* **1998**, *80*, 3803.

[42] F. E. Kruis, H. Fissan, A. Peled, *J. Aerosol Sci.* **1998**, *29*, 511.

[43] V. A. Belyakov, V. A. Burdov, R. Lockwood, A. Meldrum, *Advances in Optical Technologies* **2008**, *2008*, 279502.

[44] A. Kitai, *Luminescent Materials and Applications*, Wiley, West Sussex **2008**.

[45] L. Bergman, J. L. McHale, *Handbook of Luminescent Semiconductor Materials*, CRC Press, Boca Raton **2012**.

[46] J. S. Biteen, N. S. Lewis, H. A. Atwater, A. Polman, *Appl. Phys. Lett.* **2004**, *84*, 5389.

[47] J. P. Wolfe, *Phys. Today* **1982**, *35*, 46.

[48] I. Pelant, J. Valenta, *Luminescence Spectroscopy of Semiconductors*, Oxford University Press, New York **2012**.

[49] H. Rinnert, O. Jambois, M. Vergnat, *J. Appl. Phys.* **2009**, *106*, 23501.

[50] A. R. Goñi, L. R. Muniz, J. S. Reparaz, M. I. Alonso, M. Garriga, A. F. Loeandia, J. Rodríguez-Viejo, J. Arbiol, R. Rurali, *Phys. Rev. B* **2014**, *89*, 45413.

[51] S. Yang, W. Li, B. Cao, H. Zeng, W. Cai, *J. Phys. Chem. C* **2011**, *115*, 21056.

[52] H. Jayatilleka, D. Diamare, M. Wojdak, A. J. Kenyn, C. R. Mokry, P. J. Simpson, A. P. Knights, I. Crowe, M. P. Halsall, *J. Appl. Phys.* **2011**, *110*, 33522.

[53] V. Singh, Y. Yu, Q.-C. Sun, B. Korgel, P. Nagpal, *Nanoscale* **2014**, *6*, 14643.

[54] D.-Q. Yang, J.-N. Gillet, M. Meunier, E. Sacher, *J. Appl. Phys.* **2005**, *97*, 24303.

[55] X. D. Pi, L. Mangolini, S. A. Campbell, U. Kortshagen, *Phys. Rev. B* **2007**, *75*, 85423.

[56] I. Umezu, A. Sugimura, T. Makino, M. Inada, K. Matsumoto, *J. Appl. Phys.* **2008**, *103*, 24305.

[57] R. W. Liptak, U. Kortshagen, S. A. Campbell, *J. Am. Chem. Soc.* **2009**, *106*, 64313.

[58] S.-W. Lin, D.-H. Chen, *Small* **2009**, *5*, 72.

[59] R. N. Pereira, D. J. Rowe, R. J. Anthony, U. Kortshagen, *Phys. Rev. B* **2011**, *83*, 155327.

[60] I. Umezu, T. Kimura, A. Sugimura, *Physica B* **2006**, *376*, 853.

[61] T. Nozaki, S. K., T. Ogino, D. Asahi, K. Okazaki, *Nanotechnology* **2007**, *18*, 235603.

[62] X. D. Pi, R. W. Liptak, J. D. Nowak, N. PWells, C. B. Carter, S. A. Campbell, U. Kortshagen, *Nanotechnology* **2008**, *19*, 245603.

[63] I. N. Germanenko, M. Dongol, Y. B. Pithawalla, M. S. El-Shall, J. A. Carlisle, *Pure Appl. Chem.* **2000**, *72*, 245.

[64] X. G. Li, Y. Q. He, S. S. Talukdar, M. T. Swihart, *Langmuir* **2003**, *19*, 8490.

[65] M. V. Wolkin, J. Jorne, P. M. Fauchet, G. Allan, C. Delerue, *Phys. Rev. Lett.* **1999**, *82*, 197.

[66] A. B. Filonov, S. Ossicini, F. Bassani, F. A. D'Avitaya, *Physical Review B* **2002**, *65*, 195317.

[67] L. E. Ramos, J. Furthmuller, F. Bechstedt, *Phys. Rev. B* **2004**, *70*, 33311.

[68] K. Dohnalová, K. Kusova, I. Pelant, *Appl. Phys. Lett.* **2009**, *94*, 211903.

[69] M. L. Mastronardi, E. J. Henderson, D. P. Puzzo, G. A. Ozin, *Adv. Mater.* **2012**, *24*, 5890.

[70] L. Mangolini, D. Jurbergs, E. Rogojina, U. Kortshagen, *J. Lumin.* **2006**, *121*, 327.

[71] D. Jurbergs, E. Rogojina, L. Mangolini, U. Kortshagen, *Appl. Phys. Lett.* **2006**, *88*, 233116.

[72] R. J. Anthony, D. J. Rowe, M. Stein, J. Yang, U. Kortshagen, *Adv. Funct. Mater.* **2011**, *21*, 4042.

[73] Q. Li, T.-Y. Luo, M. Zhou, H. Abroshan, J. Huang, H. J. Kim, N. L. Rosi, Z. Shao, R. Jin, *ACS Nano* **2016**, *10*, 8385.

[74] M. Rosso-Vasic, E. Spruijt, B. Lagen, L. Cola, H. Zuilhof, *Small* **2008**, *4*, 1835.

[75] S.-M. Liu, Y. Yang, S. Sato, K. Kimura, *Chem. Mater.* **2006**, *18*, 637.

[76] J. R. Siekierzycka, M. Rosso-Vasic, H. Zuilhof, A. M. Brouwer, *J. Phys. Chem. C* **2011**, *115*, 20888.

[77] M. Dasog, G. B. De los Reyes, L. V. Titova, F. A. Hegmann, J. G. C. Veinot, *ACS Nano* **2014**, *8*, 9636.

[78] O. Guillois, N. Herlin-Boime, C. Reynaud, G. Ledoux, F. Huisken, *J. Appl. Phys.* **2004**, *95*, 3677.

[79] P. Shen, N. Uesawa, S. Inasawa, Y. Yamaguchi, *J. Mater. Chem.* **2010**, *20*, 1669.

[80] R. W. Liptak, J. Yang, N. J. Kramer, U. Kortshagen, S. A. Campbell, *Nanotechnology* **2012**, *23*, 395205.

[81] R. M. Sankaran, D. Holunga, R. C. Flagan, K. P. Giapis, *Nano Lett.* **2005**, *5*, 537.

[82] J. H. Warner, A. Hoshino, K. Yamamoto, R. D. Tilley, *Angew. Chem. Int. Ed.* **2005**, *44*, 4550.

[83] F. Hua, F. Erogbogbo, M. T. Swihart, E. Ruckenstein, *Langmuir* **2006**, *22*, 4363.

[84] D. Kovalev, J. Goss, N. Künzner, F. Koch, V. Y. Timoshenko, M. Fujii, *Phys. Rev. Lett.* **2002**, *89*, 137401.

[85] E. Gross, D. Kovalev, J. Diener, F. Koch, V. Y. Timoshenko, M. Fujii, *Phys. Rev. B* **2003**, *68*, 115405.

[86] D. Kovalev, M. Fujii, *Adv. Mater.* **2005**, *17*, 2531.

[87] G. Farace, S. Gibilisco, A. R. Pennisi, G. Franzó, S. L. Rosa, L. Lozzi, *Phys. Rev. B* **2008**, *78*, 245425.

[88] S. Godefroo, M. Hayne, M. Jivanescu, A. Stesmans, M. Zacharias, O. I. Lebedev, G. Tendeloo, V. V. Moshchalkov, *Nat. Nanotechnol.* **2008**, *3*, 174.

[89] D. C. Hannah, J. Yang, P. Podsiadlo, M. K. Y. Chan, A. Demortière, D. J. Gosztoa, V. B. Prakapenka, G. C. Schatz, U. Kortshagen, R. D. Schaller, *Nano Lett.* **2012**, *12*, 4200.

[90] K. Y. Cheng, R. Anthony, U. R. Kortshagen, R. J. Holmes, *Nano Lett.* **2010**, *10*, 1154.

[91] K. Y. Cheng, R. Anthony, U. R. Kortshagen, R. J. Holmes, *Nano Lett.* **2011**, *11*, 1952.

[92] D. P. Puzzo, E. J. Henderson, M. G. Helander, Z. Wang, G. A. Ozin, Z. Lu, *Nano Lett.* **2011**, *11*, 1585.

[93] F. Maier-Flaig, J. Rinck, M. Stephan, T. Bocksrocker, M. Bruns, C. Kübel, A. K. Powell, G. A. Ozin, U. Lemmer, *Nano Lett.* **2013**, *13*, 475.

[94] L. Yao, T. Tu, L. Ba, H. Meng, X. Fang, Y. Wang, L. Li, X. Rong, S. Wang, X. Wang, G. Ran, X. Pi, G. Qin, *J. Mater. Chem. C* **2016**, *4*, 673.

[95] S. Pimputkar, J. Speck, S. P. DenBaars, S. Nakamura, *Nat. Photonics* **2009**, *3*, 180.

[96] P. O. Anikeena, J. E. Halpert, M. G. Bawendi, V. Bulovic, *Nano Lett.* **2009**, *9*, 2532.

[97] A. Wang, H. Shen, S. Zang, Q. Lin, H. Wang, L. Qian, J. Niu, L. S. Li, *Nanoscale* **2015**, *7*, 2951.

[98] X. Dai, Z. Zhang, Y. Jin, Y. Niu, H. Cao, X. Liang, L. Chen, J. Wang, X. Peng, *Nature* **2014**, *515*, 96.

[99] Y. V. Ryabchikov, S. Alekseev, V. Lysenko, G. Bremond, J. Bluet, *Phys. Status Solidi Rapid Res. Lett.* **2013**, *6*, 414.

[100] H. Hajjaji, S. Alekseev, G. Guillot, N. P. Blanchard, V. Monnier, Y. Chevolot, G. Brémond, M. Querry, D. Philippon, V. Philippe, P. Vergne, J. Bluet, *Nanoscale Res. Lett.* **2014**, *9*, 94.

[101] C. M. Hessel, M. R. Rasch, J. L. Hueso, B. W. Goodfellow, V. A. Akhavan, P. Puvanakrisknan, J. W. Tunnell, B. A. Korgel, *Small* **2010**, *6*, 2026.

[102] X. Cheng, B. S. Lowe, P. J. Reece, J. J. Gooding, *Chem. Soc. Rev.* **2014**, *43*, 2680.

[103] L. Wang, V. Reipa, J. Blasic, *Bioconjugate Chem.* **2004**, *15*, 409.

[104] Z. F. Li, E. Ruckenstein, *Nano Lett.* **2004**, *4*, 1463.

[105] N. Petermann, N. Stein, G. Schierning, R. Theissmann, B. Stoib, M. S. Brandt, C. Hecht, C. Schulz, H. Wiggers, *J. Phys. D: Appl. Phys.* **2011**, *44*, 174034.

[106] V. Švrček, T. Sasaki, Y. Shimizu, N. Koshizaki, *Appl. Phys. Lett.* **2006**, *89*, 213113.

[107] N. Mansour, A. Momeni, R. Karimzadeh, M. Amini, *Opt. Mater. Express* **2012**, *2*, 740.

[108] Z. Kang, C. H. A. Tsang, Z. Zhang, M. Zhang, N. Wong, J. A. Zapien, Y. Shang, S.-T. Lee, *J. Am. Chem. Soc.* **2007**, *129*, 5326.

[109] K. A. Littau, P. J. Szajowski, A. J. Muller, A. R. Kortan, L. E. Brus, *J. Phys. Chem.* **1993**, *97*, 1224.

[110] C. S. Yang, R. A. Bley, S. M. Kauzlarich, H. W. H. Lee, G. R. Delgado, *J. Am. Chem. Soc.* **1999**, *121*, 5191.

[111] U. R. Kortshagen, R. M. Sankaran, R. N. Pereira, S. L. Girshick, J. J. Wu, E. S. Aydil, *Chem. Rev.* **2016**, *116*, 11061.

[112] L. Mangolini, E. Thimsen, U. Kortshagen, *Nano Lett.* **2005**, *5*, 655.

[113] U. Kortshagen, *J. Phys. D: Appl. Phys.* **2009**, *42*, 113001.

[114] C. R. Gorla, S. Liang, G. S. Tomba, W. E. Mayo, Y. Lu, *J. Vac. Sci. Technol. A* **1997**, *15*, 860.

[115] R. N. Pereira, D. J. Rowe, R. J. Anthony, U. Kortshagen, *Phys. Rev. B* **2012**, *86*, 85449.

[116] D. A. Eckhoff, J. N. Stuart, J. D. B. Sutin, J. V. Sweedler, E. Gratton, *J. Chem. Phys.* **2006**, *125*, 81103.

[117] J. Choi, N. S. Wang, V. Reipa, *Langmuir* **2007**, *23*, 3388.

[118] C. M. Hessel, D. Reid, G. M. Panthani, M. R. Rasch, B. W. Goodfellow, J. Wei, H. Fujii, V. Akhavan, B. A. Korgel, *Chem. Mater.* **2012**, *24*, 393.

[119] X. Li, Y. He, T. Swihart, *Langmuir* **2004**, *20*, 4720.

[120] M. Shigeta, A. B. Murphy, *J. Phys. D: Appl. Phys.* **2011**, *44*, 174025.

[121] R. N. Pereira, S. Niesar, W. B. You, A. F. da Cunha, N. Erhard, A. R. Stegner, H. Wiggers, M. G. Willinger, M. Stutzmann, M. S. Brandt, *J. Phys. Chem. C* **2011**, *115*, 20120.

[122] A. R. Stegner, R. N. Pereira, K. Klein, R. Lechner, R. Dietmueller, M. S. Brandt, M. Stutzmann, H. Wiggers, *Phys. Rev. Lett.* **2008**, *100*, 26803.

[123] R. N. Pereira, A. J. Almeida, A. R. Stegner, M. S. Brandt, H. Wiggers, *Phys. Rev. Letts.* **2012**, *108*, 126806.

[124] R. N. Pereira, A. J. Almeida, *J. Phys. D: Appl. Phys.* **2015**, *48*, 314005.

[125] S. Niesar, R. N. Pereira, A. R. Stegner, N. Erhard, M. Hoeb, A. Baumer, H. Wiggers, M. S. Brandt, M. Stutzmann, *Adv. Funct. Mater.* **2012**, *22*, 1190.

[126] J. Knipping, H. Wiggers, B. Rellinghaus, P. Roth, D. Konjhodzic, C. Meier, *J. Nanosci. Nanotech.* **2004**, *4*, 1039.

[127] S. Brunauer, P. H. Emmett, E. Teller, *J. Am. Chem. Soc.* **1938**, *60*, 309.

[128] M. D. Groner, F. H. Fabreguette, J. W. Elam, S. M. George, *Chem. Mater.* **2004**, *16*, 639.

[129] S. Gierałtowska, D. Sztenkiel, E. Guziewicz, M. Godlewski, G. Łuka, B. S. Witkowski, Ł. Wachnick, E. Łusakowska, T. Dietil, M. Sawicki, *Acta Phys. Pol. A* **2011**, *119*, 692.

[130] J. Haeberle, K. Henkel, H. Gargouri, F. Naumann, B. Gruska, M. Arens, M. Tallarida, D. Schmeißer, *Beilstein J. Nanotechnol.* **2013**, *4*, 732.

[131] J. G. Solé, L. E. Bausá, D. Jaque, *An Introduction to the Optical Spectroscopy of Inorganic Solids*, Wiley, West Sussex **2005**.

[132] P. Y. Yu, M. Cardona, *Fundamentals of Semiconductors*, Springer, **2010**.

[133] K. Maeda, *J. Phys. Chem. Solids* **1965**, *26*, 595.

[134] T. Schmidt, K. Lischka, W. Zulehner, *Phys. Rev. B* **1992**, *45*, 8989.

[135] L. Bergman, X.-B. Chen, J. L. Morrison, J. Huso, A. P. Purdy, *J. Appl. Phys.* **2004**, *96*, 675.

[136] V. A. Fonoberov, K. A. Alim, A. A. Balandin, F. Xiu, J. Liu, *Phys. Rev. B* **2006**, *73*, 165317.

[137] *Fluorolog® -3 Operation Manual*, Accessed 25th June 2018, Available from: http://www.horiba.com/fileadmin/uploads/Scientific/Downloads/UserArea/Fluorescence/Legacy/Complete_FluoroLog3_Manual.pdf.

[138] A. M. Hartel, S. Gutsch, D. Hiller, M. Zacharias, *Phys. Rev. B* **2012**, *85*, 165306.

[139] C. Würth, M. Grabolle, J. Pauli, M. Spieles, U. Resch-Genger, *Nat. Protoc.* **2013**, *8*, 1535.

[140] M. Grabolle, M. Spieles, V. Lesnyak, N. Gaponik, A. Eychmüller, U. Resch-Genger, *Anal. Chem.* **2009**, *81*, 6285.

[141] H. Ishida, S. Tobita, Y. Hasegawa, R. Katoh, K. Nozaki, *Coordin. Chem. Rev.* **2010**, *254*, 2449.

[142] G. Will, *Powder Diffraction: The Rietveld Method and the Two-Stage Method*, Springer, Heidelberg **2006**.

[143] J. I. Langford, A. J. C. Wilson, *J. Appl. Cryst.* **1978**, 102.

[144] U. Holzwarth, N. Gibson, *Nat. Nanotechnol.* **2011**, *6*, 534.

[145] B. D. Cullity, S. R. Stock, *Elements of X-ray Diffraction*, Pearson Education Limited, Harlow **2014**.

[146] *X-ray Powder Diffraction*, Accessed 28th June 2018, Available from: http://www.ens-lyon.fr/CHIMIE/plateformes/diffractometre/doc_diff/x-ray%20powder%20diffraction.pdf?lang=en.

[147] B. H. Toby, *Powder Diffr.* **2006**, *21*, 67.

[148] J. Rodríguez-Carvajal, *Phys. B* **1993**, *192*, 55.

[149] W. I. F. David, K. Shankland, L. B. McCusker, C. Baerlocher, *Structure Determination from Powder Diffraction Data*, Oxford University Press, Oxford **2002**.

[150] J. J. Ojeda, M. Dittrich, *Methods Mol. Biol.* **2012**, *881*, 187.

[151] P. R. Griffiths, J. A. de Haseth, *Fourier Transform Infrared Spectrometry*, Wiley, Hoboken **2007**.

[152] I. Mills, T. Cvitas, K. Homann, N. Kallay, K. Kuchitsu, *Quantities, Units and Symbols in Physical Chemistry*, Blackwell Science, **1993**.

[153] E. Smith, G. Dent, *Modern Raman Spectroscopy A Practical Approach*, Wiley, West Sussex **2005**.

[154] R. L. McCreery, *Raman Spectroscopy for Chemical Analysis*, Wiley-Interscience, New York **2000**.

[155] F. Rouquerol, J. Rouquerol, K. S. W. Sing, P. Llewellyn, G. Maurin, *Adsorption by Powders and Porous Solids*, Elsevier, Oxford **2014**.

[156] R. F. Egerton, *Physical Principles of Electron Microscopy*, Springer, Switzerland **2016**.

[157] J. F. Moulder, W. F. Stickle, P. E. Sobol, K. D. Bomben, *Handbook of X-ray Photoelectron Spectroscopy*, Perkin-Elmer Corporation Physical Electronics Division, Eden Prairie **1992**.

[158] J. F. Watts, J. Wolstenholme, *An Introduction to Surface Analysis by XPS and AES*, Wiley, Chichester **2003**.

[159] P. van der Heide, *X-ray Photoelectron Spectroscopy*, Wiley, New Jersey **2012**.

[160] P. van der Heide, *Secondary Ion Mass Spectrometry*, Wiley, New Jersey **2014**.

[161] F. A. Stevie, *Secondary Ion Mass Spectrometry*, Momentum Press Engineering, New York **2016**.

[162] A. M. P. Botas, R. A. S. Ferreira, R. N. Pereira, R. J. Anthony, T. Moura, D. J. Rowe, U. Kortshagen, *J. Phys. Chem. C* **2014**, *118*, 10375.

[163] A. M. P. Botas, R. J. Anthony, J. Wu, D. J. Rowe, N. J. Silva, U. Kortshagen, R. N. Pereira, R. A. S. Ferreira, *Nanotechnology* **2016**, *27*, 325703.

[164] B. P. Swain, B. S. Swain, Y.-B. Chung, N. M. Hwang, *Solid State Sci.* **2009**, *11*, 1408.

[165] J. Holm, J. T. Roberts, *J. Am. Chem. Soc.* **2007**, *129*, 2496.

[166] S. Gardelis, A. G. Nassiopoulou, N. Vouroutzis, N. Frangis, *J. Appl. Phys.* **2009**, *105*, 113509.

[167] J. Heitmann, F. Muller, L. X. Yi, M. Zacharias, D. Kovalev, F. Eichhorn, *Phys. Rev. B* **2004**, *69*, 195309.

[168] C. Delerue, G. Allan, C. Reynaud, O. Guillois, G. Ledoux, F. Huisken, **2006**, *73*, 235318.

[169] K. Dunn, J. Derr, T. Johnston, M. Chaker, F. Rosei, *Phys. Rev. B* **2009**, *80*, 35330.

[170] R. A. Street, *Adv. Phys.* **1981**, *30*, 593.

[171] A. Y. Kobitski, K. S. Zhuravlev, H. P. Wagner, D. R. T. Zahn, *Phys. Rev. B* **2001**, *63*, 115423.

[172] I. Umezu, T. Kimura, A. Sugimura, *Phys. B* **2006**, *376*, 853.

[173] N. Chestnoy, T. D. Harris, R. Hull, *J. Phys. Chem.* **1986**, *90*, 3393.

[174] H. Koyama, T. Ozaki, N. Koshida, *Phys. Rev. B* **1995**, *52*, 11561.

[175] Y. Zhong, K. S. Wong, W. Zhang, D. C. Look, *Appl. Phys. Lett.* **2006**, *89*, 22108.

[176] F. Himpsel, F. McFeely, A. Taleb-Ibrahimi, J. Yarmoff, G. Hollinger, *Phys. Rev. B* **1988**, *38*, 6084.

[177] H. Nohira, A. Omura, M. Katayama, T. Hattori, *Appl. Surf. Sci.* **1998**, *123*, 546.

[178] V. V. Afanas'ev, M. Houssa, A. Stesmans, M. M. Heyns, *Appl. Phys. Lett.* **2001**, *78*, 3073.

[179] C. G. Van de Walle, J. Neugebauer, *Nature* **2003**, *423*, 626.

[180] S. M. Sze, K. K. Ng, *Physics of Semiconductor Devices*, Wiley-Interscience, **1969**.

[181] K. Dohnalová, T. Gregorkiewicz, K. Kusová, *J. Phys.: Condens. Matter* **2014**, *26*, 173201.

[182] R. Limpens, A. Lesage, P. Stallinga, A. N. Poddubny, M. Fujii, T. Gregorkiewicz, *J. Phys. Chem. C* **2015**, *119*, 19565.

[183] G. B. Reyes, M. Dasog, M. Na, L. V. Titova, J. G. C. Veinot, F. A. Hegmann, *Phys. Chem. Chem. Phys.* **2015**, *17*, 30125.

[184] E. A. Costner, B. K. Long, C. Navar, S. Jockusch, X. Lei, P. Zimmerman, A. Campion, N. J. Turro, C. G. Willson, *J. Phys. Chem. A* **2009**, *113*, 9337.

[185] L. Sutton, *Tables of Interatomic Distances and Configuration of Molecules and Ions: Supplement 1956-1959*, Chemical Society, **1965**.

[186] P. Schapotschnikow, R. Pool, T. J. H. Vlugt, *Nano Lett.* **2008**, *8*, 2930.

[187] P. Schapotschnikow, T. J. H. Vlugt, *J. Chem. Phys.* **2009**, *131*, 124705.

[188] K. Furuta, M. Fujii, H. Sugimoto, K. Imakita, *J. Phys. Chem. Lett.* **2015**, *6*, 2761.

[189] L. Pavesi, *J. Appl. Phys.* **1996**, *80*, 216.

[190] P. D. J. Calcott, K. J. Nash, L. T. Canham, M. J. Kane, D. Brumhead, *J. Phys. Condens.: Matter* **1993**, *5*, 91.

[191] C. Tu, Q. Zhang, L. Y. Lin, G. Cao, *Opt. Express* **2012**, *20*, 1585.

[192] A. M. P. Botas, C. D. S. Brites, J. Wu, U. Kortshagen, R. N. Pereira, L. D. Carlos, R. A. S. Ferreira, *Part. Part. Syst. Charact.* **2016**, *33*.

[193] C. D. S. Brites, P. P. Lima, N. J. O. Silva, A. Millán, V. S. Amaral, F. Palacio, L. D. Carlos, *Nanoscale* **2012**, *4*, 4799.

[194] D. Jaque, F. Vetrone, *Nanoscale* **2012**, *4*, 4301.

[195] G. Kucsko, P. C. Maurer, N. Y. Yao, M. Kubo, H. J. Noh, P. K. Lo, H. Park, M. D. Lukin, *Nature* **2013**, *500*, 54.

[196] Z. Wang, X. Ma, S. Zong, Y. Wang, H. Chen, Y. Cui, *Talanta* **2015**, *131*, 259.

[197] L. D. Carlos, F. Palacio, *Thermometry at the Nanoscale*, Cambridge: Royal Society of Chemistry, UK **2016**.

[198] K. Okabe, N. Inada, C. Gota, Y. Harada, T. Funatsu, S. Uchiyama, *Nat. Commun.* **2012**, *3*, 705.

[199] D. Jaque, B. Rosal, E. M. Rodríguez, L. M. Maestro, P. Haro-González, J. G. Solé, *Nanomedicine* **2014**, *9*, 1047.

[200] Z. Wang, D. Ananias, A. Carné-Sánchez, C. D. S. Brites, I. Inhar, D. Maspoch, J. Rocha, L. D. Carlos, *Adv. Funct. Mater.* **2015**, *25*, 2824.

[201] A. Pfenning, F. Hartmann, M. R. S. Dias, L. K. Castelano, C. SüBmeier, F. Langer, S. Höfling, M. Kamp, G. E. Marques, L. Worschech, V. Lopez-Richard, *ACS Nano* **2015**, *9*, 6271.

[202] X. Xu, Z. Wang, P. Lei, Y. Yu, S. Yao, S. Song, X. Liu, Y. Su, L. Dong, J. Feng, H. Zhang, *ACS Appl. Mater. Interfaces* **2015**, *7*, 20813.

[203] H. Peng, M. I. J. Stich, J. Yu, L. Sun, L. H. Fischer, W. O. S., *Adv. Mater.* **2010**, *22*, 716.

[204] C. D. S. Brites, P. P. Lima, N. J. O. Silva, A. Millán, V. S. Amaral, F. Palacio, L. D. Carlos, *Nanoscale* **2013**, *5*, 7572.

[205] W. Xu, X. Gao, L. Zheng, Z. Zhang, W. Cao, *Sensor Actuat B-Chem* **2012**, *173*, 250.

[206] A. Pandey, V. K. Rai, *Appl. Phys. B* **2013**, *113*, 221.

[207] A. Bar-Cohen, P. Wang, *Microgravity Sci. Technol.* **2009**, *21*, S351.

[208] L. Shi, C. Dames, J. R. Lukes, P. S. Reddy, J. Duda, D. G. Cahill, J. Lee, A. Marconnet, K. E. Goodson, J.-H. Bahk, A. Shakouri, R. S. Prasher, J. Felts, W. P. King, B. Han, J. C. Bischof, *Nanosc. and Microsc. Therm.* **2015**, *19*, 127.

[209] B. Han, W. L. Hanson, K. Bensalah, A. Tuncel, J. M. Stern, J. A. Cadeddu, *Ann. Biomed. Eng.* **2009**, *37*, 1230.

[210] K. Oyama, M. Takabayashi, Y. Takei, S. Arai, S. Takeoka, S. Ishiwata, M. Suzuki, *Lab Chip* **2012**, *12*, 1591.

[211] M. L. Debasu, D. Ananias, I. Pastoriza-Santos, L. M. Liz-Marzán, J. Rocha, L. D. Carlos, *Adv. Mater.* **2013**, *25*, 4868.

[212] A. S. Souza, L. A. O. Nunes, I. G. N. Silva, F. A. M. Oliveira, L. L. Luz, H. F. Brito, M. C. F. C. Felinto, R. A. S. Ferreira, S. A. Júnior, L. Carlos, O. L. Malta, *Nanoscale* **2016**, *8*, 5327.

[213] A. H. Khaid, K. Kontis, *Meas. Sci. Technol.* **2009**, *20*, 025305.

[214] V. Lojpur, Z. Antic, M. D. Dramicanin, *Phys. Chem. Chem. Phys.* **2014**, *16*, 25636.

[215] C. Gota, S. Uchiyama, T. Ohwada, *Analyst* **2007**, *132*, 121.

[216] C. Gota, K. Okabe, T. Funatsu, Y. Harada, S. Uchiyama, *J. Am. Chem. Soc.* **2009**, *131*, 2766.

[217] C. Pietsch, U. S. Schubert, R. Hoogenboom, *Chem. Commun.* **2011**, *47*, 8750.

[218] T. Itoh, T. Shichi, T. Yui, H. Takahashi, Y. Inui, K. Takagi, *J Phys. Chem. B* **2005**, *109*, 3199.

[219] D. Yan, J. Lu, J. Ma, M. Wei, D. G. Evans, X. Duan, *Angew. Chem., Int. Ed.* **2011**, *50*, 720.

[220] A. R. V. Sickle, J. B. Miller, C. Moore, R. J. Anthony, U. R. Kortshagen, E. K. Hobbie, *ACS Appl. Mater. Interfaces* **2013**, *5*, 4233.

[221] L. M. Maestro, Q. Zhang, X. Li, D. Jaque, M. Gu, *Appl. Phys. Lett.* **2014**, *105*, 181110.

[222] C. D. S. Brites, P. P. Lima, N. J. O. Silva, A. Millán, V. S. Amaral, F. Palacio, L. D. Carlos, *Adv. Mater.* **2010**, *22*, 4499.

[223] L. H. Fischer, G. S. Harms, O. S. Wolfbeis, *Angew. Chem., Int. Ed.* **2011**, *50*, 4546.

[224] V. Lojpur, M. G. Nikolic, M. D. Dramicanin, *J. Appl. Phys.* **2014**, *115*, 203106.

[225] O. A. Savchuk, P. Haro-González, J. J. Carvajal, D. Jaques, J. Massons, M. Aguiló, F. Díaz, *Nanoscale* **2014**, *6*, 9727.

[226] Y. Huang, F. Rosei, F. Vetrone, *Nanoscale* **2015**, *7*, 5178.

[227] R. Pinol, C. D. S. Brites, R. Bustamante, A. Martínez, N. J. O. Silva, J. L. Murillo, R. Cases, J. Carrey, C. Estepa, S. C., F. Palacio, L. D. Carlos, A. Millán, *ACS Nano* **2015**, *9*, 3134.

[228] C. D. S. Brites, P. P. Lima, N. J. O. Silva, A. Millán, V. S. Amaral, F. Palacio, L. D. Carlos, *New J. Chem.* **2011**, *35*, 1177.

[229] X. Wang, O. S. Wolfbeis, R. J. Meier, *Chem. Soc. Rev.* **2013**, *42*, 7834.

[230] C. D. S. Brites, A. Millán, L. D. Carlos, in *Handbook on the Physics and Chemistry of Rare Earths*, Vol. 48 (Eds: K. A. Gshneidner, J.-C. Bünzli, V. Pecharsky), Elsevier, 2016, 339.

[231] M. Lippitsch, S. Draxler, *Sensor Actuat B-Chem* **1993**, *11*, 97.

[232] C. D. S. Brites, P. P. Lima, L. D. Carlos, *J. Lumin.* **2016**, *169*, 497.

[233] D. Pugh-Thomas, B. M. Walsh, M. C. Gupta, *Nanotechnology* **2011**, *22*, 185503.

[234] H. Hajjaji, A. Sayed, G. Gerard, M. Mathieu, D. Philippon, P. Vergne, J. M. Bluet, *J. Phys. Chem. C* **2015**, *119*, 16897.

[235] L. Liu, S. Creten, Y. Firdaus, J. J. A. F. Cuautle, M. Kouyaté, M. V. Auweraer, C. Glorieux, *Appl. Phys. Lett.* **2014**, *104*, 031902.

[236] J. Beyer, D. Drung, A. Kirste, A. Engert, A. Netsch, A. Fleischmann, C. Enss, *IEEE T. Appl. Supercon.* **2007**, *17*, 760.

[237] S. Balabhadra, M. L. Debasu, C. D. S. Brites, R. A. S. Ferreira, L. D. Carlos, *J. Phys. Chem. C* **2017**, *121*, 13962.

[238] J. Fischer, M. Podesta, K. D. Hill, M. Moldover, L. Pitre, R. Rusby, P. Steur, O. Tamura, R. White, L. Wolber, *Int. J. Thermophys.* **2011**, *32*, 12.

[239] J. Fischer, *Metrologia* **2015**, *52*, S364.

[240] M. R. Moldover, W. L. Tew, H. W. Yoon, *Nat. Phys.* **2016**, *12*, 7.

[241] N. Koshida, *Device Applications of Silicon Nanocrystals and Nanostructures*, Springer, New York, USA **2009**.

[242] O. S. Wolfbeis, *Chem. Soc. Rev.* **2015**, *44*, 4743.

[243] Y. V. Ryabchikov, S. A. Alekseev, V. Lysenko, G. Bremond, J. Bluet, *J. Nanopart. Res.* **2013**, *15*, 1535.

[244] F. A. Kruse, A. B. Lefkoff, J. W. Boardman, K. B. Heidebrecht, A. T. Shapiro, P. J. Barloon, A. F. H. Goetz, *Remote Sens. Environ.* **1993**, *44*, 145.

[245] N. Zaini, F. Meer, H. Werff, *Remote Sens.* **2014**, *6*, 4149.

[246] A. N. Goldstein, *Appl. Phys. A* **1996**, *62*, 33.

[247] Y. P. Varshni, *Physica* **1967**, *34*, 149.

[248] J. Derr, K. Dunn, D. Riabinina, F. Martin, M. Chaker, F. Rosei, *Physica E* **2009**, *41*, 668.

[249] S. F. Collins, G. W. Baxter, S. A. Wade, T. Sun, K. T. V. Grattan, Z. Y. Zhang, A. W. Palmer, *J. Appl. Phys.* **1998**, *84*, 4649.

[250] V. K. Rai, *Appl. Phys. B* **2007**, *88*, 297.

[251] Y. V. Ryabchiknov, V. Lysenko, T. Nychyporuk, *J. Phys. Chem. C* **2014**, *118*, 12515.

[252] G. Chen, C. Yang, P. N. Prasad, *Accounts Chem. Res.* **2013**, *46*, 1474.

[253] Y. Liu, M. Gibbs, C. L. Perkins, J. Tolentino, M. H. Zarghami, J. Bustamante Jr., M. Law, *Nano Lett.* **2011**, *11*, 5349.

[254] Y. Liu, J. Tolentino, M. Gibbs, R. Ihly, C. L. Perkins, Y. Liu, N. Crawford, J. C. Hemminger, M. Law, *Nano Lett.* **2013**, *13*, 1578.

[255] M. Palei, V. Caligiuri, S. Kudera, R. Krahne, *ACS Appl. Mater. Interfaces* **2018**, *10*, 22356.

[256] S. Weis, R. Körmer, M. P. M. Jank, M. Lemberger, M. Otto, H. Ryssel, W. Peukert, L. Frey, *Small* **2011**, *7*, 2853.

[257] S. M. George, *Chem. Rev.* **2010**, *110*, 111.

[258] N. Pinna, M. Knez, *Atomic Layer Deposition of Nanostructured Materials*, Wiley-VCH, Germany **2012**.

[259] R. W. Johnson, A. Hultqvist, S. F. Bent, *Mater. Today* **2014**, *17*, 236.

[260] R. L. Puurunen, *J. Appl. Phys.* **2005**, *97*, 121301.

[261] A. W. Ott, J. W. Klaus, J. M. Johnson, S. M. George, *Thin Solid Films* **1997**, *292*, 135.

[262] J. C. Hackley, T. Gougousi, J. D. Demaree, *J. Appl. Phys.* **2007**, *102*, 034101.

[263] E. Thimsen, M. Johnson, X. Zhang, A. J. Wagner, K. A. Mkhoyan, U. R. Kortshagen, E. S. Aydil, *Nat. Commun.* **2014**, *5*, 5822.

[264] A. Pourret, P. Guyot-Sionnest, J. W. Elam, *Adv. Mater.* **2009**, *21*, 232.

[265] M. J. Chen, Y. T. Shih, M. K. Wu, F. Y. Tsai, *J. Appl. Phys.* **2007**, *101*, 033130.

[266] M. Liu, R. Chen, G. Adamo, K. F. MacDonald, E. J. Sie, T. C. Sum, N. I. Zheludev, H. Sun, H. J. Fan, *Nanophotonics* **2013**, *2*, 153.

[267] M. Saboktakin, X. Ye, S. J. Oh, S.-H. Hong, A. T. Fafarman, U. K. Chettiar, N. Engheta, C. B. Murray, C. R. Kagan, *ACS Nano* **2012**, *6*, 8758.

[268] N. P. Dasgupta, H. J. Jung, O. Trejo, M. T. McDowell, A. Hryciw, M. Brongersma, R. Sinclair, F. B. Prinz, *Nano Lett.* **2011**, *11*, 934.

[269] K. Devloo-Casier, P. Geiregat, K. F. Ludwig, K. van Stiphout, A. Vantomme, Z. Hens, C. Detavernier, J. Dendooven, *J. Phys. Chem. C* **2016**, *120*, 18039.

[270] C. Lutinski, *Anal. Chem.* **1958**, *30*, 2071.

[271] M. Milosevic, S. W. K. King, *ECS J. Solid State Sci. Technol.* **2015**, *4*, N3146.

[272] T. Adams, C. Grant, H. Watson, *International Journal of Mechanical Engineering and Mechatronics* **2012**, *1*, 66.

[273] C. D. Wagner, W. M. Riggs, L. E. Davis, J. F. Moulder, G. E. Muilenberg, *Handbook of X-ray Photoelectron Spectroscopy*, Perkin-Elmer Corporation, **1979**.

[274] E. Korin, N. Froumin, S. Cohen, *ACS Biomater. Sci. Eng.* **2017**, *3*, 882.

[275] J. van der Brand, S. V. Gils, P. C. J. Beentjes, H. Terryn, J. H. W. de Wit, *Appl. Surf. Sci.* **2004**, *235*, 465.

[276] M. Pal, S. Bera, S. Sarkar, S. Jana, *RSC Adv.* **2014**, *4*, 11552.

[277] K. Djebaili, Z. Mekhalif, A. Boumaza, A. Djellout, *J. Spectrosc.* **2015**, *2015*, 868109.

[278] S. Pletincx, K. Marcoen, L. Trotochaud, L.-L. Fockaert, J. M. C. Mol, A. R. Head, O. Karslioğlu, H. Bluhm, H. Terryn, T. Hauffman, *Sci. Rep.* **2017**, *7*, 13341.

[279] *Database of ATR-FT-IR Spectra of Various Materials*, Accessed 13th March 2018, Available from: http://lisa.chem.ut.ee/IR_spectra/paint/fillers/aluminium-oxide/.

[280] S. Hernández, J. López-Vidrier, L. López-Conesa, D. Hiller, S. Gutsch, J. Ibáñez, S. Estradé, F. Peiró, M. Zacharias, B. Garrido, *J. Appl. Phys.* **2014**, *115*, 203504.

[281] W. Aigner, O. Bienek, B. P. Falcão, S. U. Ahmed, H. Wiggers, M. Stutzmann, R. N. Pereira, *Nanoscale* **2018**, *10*, 8042.